Characterization of Interplay Errors in Step-and-Shoot Intensity-Modulated Radiation Therapy of the Lung

by

Travis J. McCaw

A dissertation submitted in partial fulfillment of
the requirements for the degree of

Doctor of Philosophy

(Medical Physics)

at the

University of Wisconsin-Madison

2015

Date of final oral examination: 01/12/15

This dissertation is approved by the following members of the Final Oral Committee:
Larry A. DeWerd, Professor, Medical Physics
Bruce R. Thomadsen, Professor, Medical Physics
Michael W. Kissick, Assistant Professor, Medical Physics
Bryan P. Bednarz, Assistant Professor, Medical Physics
Douglass L. Henderson, Professor, Engineering Physics

To Dad. Thanks for leading the way.

Abstract

Radiation therapy is used for the treatment of inoperable early-stage and advanced-stage lung cancer. Target motion during these treatments due to respiration causes delivery errors relative to the planned dose. Current recommendations for the use of motion management techniques to mitigate these errors are based on the measured amplitude of target motion. However, frequency-dependent errors due to interplay between target motion and intensity modulation of the treatment delivery may not be adequately managed by these recommendations.

A radiochromic film stack dosimeter (FSD) was developed to verify Monte Carlo simulations of interplay errors in step-and-shoot intensity-modulated radiation therapy (SS-IMRT). The energy dependence, orientation dependence, and water equivalence of the FSD were characterized. The accuracy of the FSD was verified by comparison with thermoluminescent dosimeter measurements and treatment planning software dose calculations. The FSD was shown to be capable of accurate and precise three-dimensional dose measurements.

A Monte Carlo model of a linear accelerator was developed using the EGSnrc transport code for the simulation of interplay errors. The model was verified with the comparison of measured and simulated dose profiles.

Conventionally fractionated and hypofractionated SS-IMRT treatment plans were prepared for the investigation of interplay errors. The delivery of each plan was measured with the FSD undergoing modeled respiratory motion. These measurements were reconstructed

using the Monte Carlo accelerator model to verify the methodology for the simulation of interplay errors. For each treatment plan, deliveries were simulated for target motion periods from 1 s to 180 s to identify characteristic modulation frequencies for which interplay errors were greatest. The impact of respiratory motion irregularity on interplay errors was investigated, and cumulative interplay errors over a fractionated treatment course were quantified.

It was demonstrated that interplay errors are greatest for longer motion periods, representative of drifts in the baseline target position, corresponding with the low-frequency intensity modulations of the treatment. For motion amplitudes of 5 mm, for which the use of motion management is currently recommended, interplay errors were minimal. Based on the results of this work, amplitude-based motion management criteria are sufficient to mitigate interplay errors in SS-IMRT.

Acknowledgments

The past five years in Madison have been some of the most challenging, rewarding, and enjoyable years that I have known. This thesis would not have been possible without substantial contributions from colleagues, friends old and new, and family. I do not have the words to express the gratitude that I feel for the support that I have received along this journey, but I will attempt to give due recognition to those who made this work possible.

First and foremost, I want to thank my advisor, Prof. Larry DeWerd. Larry provides his students with an unrivaled collection of resources and expertise, giving them every opportunity not only to succeed, but to excel. My journey to the Calibration Lab was an unconventional one, and I will forever be indebted to Larry for taking me on after my first year in the graduate program when I was without funding. I would also like to thank Prof. Bruce Thomadsen, who was my advisor during my first year in the graduate program. Bruce helped me get oriented within the department, but also challenged me to find my way within the realm of academic research. I am grateful for the references and insight from both Larry and Bruce during my residency application process; without their contributions, I would not have secured the position at UPMC. This opportunity arose unexpectedly and required an aggressive timeline for the completion of this thesis; I am thankful for Larry's willingness to allow me to pursue this opportunity, as well as his efforts to make the timeline possible.

The idea that led to this thesis work was proposed by Prof. Michael Kissick. Throughout the course of my research, Michael provided invaluable guidance and generously allowed me to use his equipment, which was instrumental to the completion of this thesis.

The students and staff of the Medical Radiation Research Center contributed extensively to the completion of this thesis. John Micka was always available for a discussion of experimental design and analysis methods. Dan Anderson and Keith Kunugi patiently handled endless notifications that I had once again exhausted the memory of the computing cluster or MATLAB. Cliff Hammer provided TLD expertise, and on more than one occasion restored the results presented in this thesis after they were inadvertently erased. Jeff Radtke designed and assembled the circuitry that was necessary for the simulated reconstruction of the interplay measurements. The students of the Medical Radiation Research Center provided valuable feedback and suggestions throughout the completion of this thesis work, and also reviewed drafts of this thesis in varying stages of presentability. I would especially like to thank Josh Reed, who reviewed two chapters of this thesis, the latter of which was with little advance notice over a holiday.

Throughout the completion of this thesis work, I had the opportunity to work as both a teaching assistant and a physics assistant. Prof. Jennifer Smilowitz served as a mentor to both positions, and I am grateful for her trust in me to fulfill the responsibilities of both positions, and for her guidance along the way. I also want to thank Dr. Ranjini Tolakanahalli, who initially offered me the physics assistant position, and Mark Geurts for their mentorship in this role. Jialu Yu and Brad McCabe provided the training to prepare me for the physics assistant position. I want to thank my counterparts Martha Malin and Abby Besemer for helping to keep the work manageable and for covering for me in my absences. I also want to thank Sam Simiele, Yin Zhang, Michael Lawless, Megan Hyun, and Everardo Flores for staying through the late nights, keeping the late nights from being later, and for covering for me in my absences.

I could not have completed this thesis work without the unwavering support of friends and family. It seems like a lifetime ago that I passed days in the fish tank with Josh Hubbell and Erich Urban working on problem sets. They were not the most productive days, but certainly some of the most memorable. Two years together in the program were not enough. Sam Simiele, thanks for being the best cube neighbor, always available for a second opinion or a needed distraction. Wes Culberson, your contributions to this thesis work far exceed assistance with treatment planning, review of manuscripts, and general discussions. I will always value your insight and your friendship, and I look forward to reunions at professional meetings. Ben Palmer, you are a true friend. Thank you for everything that you have done for Lauren and I. For many reasons it will be difficult for us to leave Madison, but it would not be nearly so difficult if not for you.

Without my family, I would not have had the stamina to persevere through the completion of this thesis work. Their continued interest in discussing my research helped me maintain the necessary curiosity and motivation. After particularly discouraging days, their indefatigable optimism gave me reason to keep trying. Most importantly, I want to thank my wife, Lauren. Throughout this thesis work she celebrated my victories, suffered my failures, and endured the rapid transitions between the two. Despite my best efforts to the contrary, she stayed with me through it all, and made me better for it. I hope to someday find the means to adequately express my appreciation for all that she has done and continues to do.

Finally, for those whose contributions to this thesis work were not explicitly acknowledged, I apologize. Know that my failure to recall your assistance is not indicative of the appreciation that I have for your contribution.

Contents

List of Figures

List of Tables

Chapter 1

Introduction

1.1 Overview

Patients with inoperable early-stage or advanced-stage lung cancer are treated using radiation therapy, chemotherapy, or both [Siegel et al., 2012]. Intensity-modulated radiation therapy (IMRT) is used to improve the conformality of radiation treatments, permitting the delivery of greater doses without further compromising healthy tissue. However, motion of the target during treatment, due to respiration, for instance, results in delivery errors relative to the planned dose distribution.

In a treatment of a moving target, the delivered dose is averaged over the path of motion, thereby reducing the planned dose gradients and degrading the treatment conformality. The magnitude of these so-called blurring errors is dependent on the motion trajectory of the target volume, but not the motion frequency. To compensate for blurring errors, treatment margins are increased and measures are taken to limit the excursion of the target volume. In IMRT treatments of a moving target, additional delivery errors are possible due to the temporal intensity modulation inherent in the treatment delivery. Specifically, interplay between the motion of the target and the intensity modulation of the treatment delivery can result in delivery errors dependent on the frequency of the target motion. Interplay

errors can occur within the interior of the target volume, in which case mitigation may not be possible with increased treatment margins and restriction of motion amplitude.

The report of the American Association of Physicists in Medicine (AAPM) Task Group 76 addresses the use of respiratory motion management in radiation therapy [Keall et al., 2006]. This report recommends the use of respiratory motion management for treatments of targets with a motion amplitude of greater than 5 mm. The recommendation of motion management criteria based exclusively on the target motion amplitude disregards the frequency dependence of interplay errors. The exclusion of interplay considerations was justified with studies demonstrating that interplay errors average out over the delivery of many treatment fractions [Bortfeld et al., 2002; Jiang et al., 2003]. However, these studies modeled respiratory motion as a regular, one-dimensional sinusoid that was invariant over thirty fractions. In actuality, respiratory motion is irregular, with variable motion amplitude, motion period, and baseline position [Tobin et al., 1983a,b; Bruce, 1996; Engelsman et al., 2005; Blackall et al., 2006; Shirato et al., 2006; Trofimov et al., 2008; Zhao et al., 2011].

Investigations of tomotherapy treatments of targets undergoing realistic respiratory motion [Kissick et al., 2008; Chaudhari et al., 2009; Tudor et al., 2014] have found substantial delivery errors for motion amplitudes not exceeding the 5 mm criteria recommended by Task Group 76 for the use of motion management [Keall et al., 2006]. These studies attributed the delivery errors to interference, or interplay, between the motion of the treatment couch and the low-frequency drifts in the position of the target. Such interference errors are unique to each IMRT modality and the corresponding characteristic modulation frequencies. As noted by Kissick and Mackie [2009], separate characterizations of each IMRT modality should be completed to develop frequency-dependent motion-management criteria necessary for the mitigation of these interference errors.

This thesis work investigated delivery errors due to the interplay effect in step-and-shoot IMRT lung treatments. Monte Carlo simulations of IMRT treatments were used to identify characteristic modulation frequencies and to quantify delivery errors due to interference between the intensity modulation and target motion. The impact of motion irregularity and the cumulative errors over a fractionated treatment delivery were both determined. A Monte Carlo linear accelerator model was first developed and experimentally verified for use in this work. Simulations of interplay errors were experimentally verified with the comparison of measured and simulated treatments of a moving target. Measurements of interplay errors were completed using a three-dimensional (3D) radiochromic film stack dosimeter, which was developed and characterized as part of this work. The results of this work provide an experimental basis for the recommendation of motion-management criteria to mitigate frequency-dependent interplay errors.

1.2 Description of upcoming chapters

Chapter 2 discusses the treatment of lung cancer with radiation therapy, including a description of the general treatment planning and delivery processes. The impact of respiratory motion on the delivery of radiation therapy treatments is addressed with a discussion of treatment errors due to target motion and techniques to reduce these errors. The final section of this chapter discusses the motivations and goals for this thesis work, including a review of investigations of the interplay effect.

Chapter 3 discusses the methods employed in this thesis work for radiochromic film and TLD dosimetry. In particular, techniques for the handling and analysis of each of these dosimeters are summarized. A characterization of the scanner used to analyze radiochromic films is described, including a justification for the analysis methods used in this work.

Chapter 4 describes the development of the radiochromic film stack dosimeter, including the motivation for its development. The energy dependence, orientation dependence,

and water equivalence of the film stack dosimeter are investigated. Film stack dosimeter measurements are compared with TLD measurements and treatment planning software calculations. An uncertainty analysis of both TLD measurements and film stack dosimeter measurements is provided.

Chapter 5 describes the development of a Monte Carlo model of the linear accelerator used for simulations of the interplay effect. Validation of the simulation techniques used in this thesis work is discussed. Comparisons of measured and simulated dose profiles are presented as verification of the model. Additionally, the preparation of the multileaf collimator model is described.

Chapter 6 discusses the investigation of interplay errors in step-and-shoot IMRT. Two treatment plans are prepared for the investigation. Measurements of these treatment plans with the film stack dosimeter for the verification of the interplay simulation methodology is discussed. The procedure for the simulation of interplay errors is described, and a comparison of measured and simulated treatment deliveries is presented. Results are provided identifying characteristic modulation frequencies of the step-and-shoot IMRT plans and quantifying the delivery error due to interference between the treatment modulation and the target motion. The impact of target motion irregularity on delivery errors, and the cumulative delivery errors over a fractionated treatment due to interplay are determined.

Chapter 7 provides the overall conclusions of this thesis work. Recommendations for future investigations of the film stack dosimeter and interplay errors are also provided.

Chapter 2

Background

2.1 Lung cancer

Lung cancer is the second-most frequently diagnosed cancer among both men and women in the United States. Only prostate cancer (men) and breast cancer (women) have higher rates of diagnosis than lung cancer. Additionally, the American Cancer Society estimates that lung cancer will account for 27 % of all cancer deaths in 2014, the most of all cancer sites [Siegel et al., 2014].

There are two major types of lung cancer: small-cell lung cancer, named for the appearance of the cancer cells, and non-small-cell lung cancer (NSCLC), which accounts for 85 % of all lung cancer diagnoses in the United States [Molina et al., 2008]. Small-cell lung cancer is treated using radiation therapy alone for disease of limited extent, or radiation therapy combined with chemotherapy for more widespread disease. Surgical resection is the most common treatment for stage I or stage II NSCLC; however, early-stage lung cancers are typically asymptomatic, so only 15 % of lung cancers are diagnosed at a local stage [Siegel et al., 2012]. Additionally, many patients with early-stage disease do not qualify for surgery due to coexisting morbidity, such as chronic obstructive pulmonary disease or cardiovascular

disease [Nyman et al., 2006]. Inoperable early-stage and advanced-stage NSCLC is treated using radiation therapy, chemotherapy, or both [Siegel et al., 2012].

The merit of radiation therapy for the treatment of inoperable lung cancer was demonstrated in a randomized clinical trial by Wolf et al. [1966], which concluded that radiation doses of 4000 cGy to 5000 cGy delivered in daily fractions of 150 cGy to 200 cGy significantly improved survival relative to placebo. Following a phase III trial by the Radiation Therapy Oncology Group (RTOG) to investigate the efficacy of different dose prescriptions [Sause et al., 1995], a delivery of 60 Gy over 30 fractions became the standard treatment schedule for inoperable, regionally advanced NSCLC [Molina et al., 2008]. However, the five-year survival rate following this treatment course was less than 10 % [Dillman et al., 1996] with local failure rates of 50 %, compared with failure rates of 5 % to 20 % following resection [Mehta et al., 2001]. Mehta et al. [2001] observed that NSCLC is both relatively radioresistant and proliferative, suggesting that hypofractionation (i.e., higher fraction doses and fewer fractions) is necessary to improve rates of tumor control.

The escalation of prescription doses is limited by the dose tolerance of healthy lung tissue. One of the most common clinical toxicities in radiation therapy of the lung is radiation pneumonitis, which is inflammation of lung tissue that can cause difficulty breathing. The occurrence of radiation pneumonitis is correlated with mean lung dose [Kwa et al., 1998; Hernando et al., 2001; Yorke et al., 2002]. For conventionally fractionated (i.e., 200 cGy per fraction) treatments, the mean lung dose must be held below 20 Gy to 23 Gy to limit the risk of radiation pneumonitis to 20 % [Marks et al., 2010a]. Therefore, the treated volume of lung tissue must be held to a minimum. However, as discussed in Sec. 2.3.1, tumor excursion due to respiration can be substantial, requiring the treatment of a greater volume of lung tissue to ensure effective treatment of the tumor. Methods to reduce tumor motion due to respiration, and consequently the treated lung volume, are discussed in Sec. 2.3.4.

With the appropriate management of respiratory motion amplitude, stereotactic body radiation therapy (SBRT), a highly conformal, hypofractionated treatment technique, has been shown to be well-tolerated and to improve rates of local control and survival compared with conventionally fractionated treatments of NSCLC. Dose escalation studies by McGarry et al. [2005] and Timmerman et al. [2003] both demonstrated that total doses up to 60 Gy can be delivered over three fractions for tumors up to 7 cm in diameter without the onset of limiting toxicities. For a prescription dose of 45 Gy delivered over three fractions, Nyman et al. [2006] observed a local failure rate of 20 % and a five-year survival rate of 30 %. Additionally, Grills et al. [2010] found that prescription doses of 48 Gy or 60 Gy delivered over four or five fractions reduced the rate of local recurrence relative to wedge resection, in which the diseased tissue and a sublobar margin of healthy tissue are surgically removed. Given the apparent success of SBRT for the treatment of NSCLC, the RTOG has initiated clinical trials to investigate the use of SBRT for the treatment of operable (RTOG 0618) and inoperable (RTOG 0236) disease, with additional trials to investigate centrally (RTOG 0813) or peripherally (RTOG 0915) located inoperable disease. Currently, results are only available for RTOG 0236, which reported an overall survival rate of 55.8 %, and a local control rate of 90.6 % at the three-year follow-up [Timmerman et al., 2010].

2.2 External-beam radiation therapy

In linear-accelerator based external-beam radiation therapy (EBRT), electrons are accelerated to energies of several mega-electron-volts and collided with a target to produce a beam of bremsstrahlung radiation. The resulting beam is shaped by the collimator jaws and the multileaf collimator (MLC). The jaws provide coarse collimation to a rectangular field. The MLC is comprised of opposing sets of high-density leaves capable of one-dimensional translation to provide fine collimation.

The output of a linear accelerator is quantified in terms of monitor units (MU). A pair of monitor ionization chambers positioned between the bremsstrahlung target and the jaws provide a measure of the ionization current generated by the radiation beam. A MU is a scaled measure of the integrated ionization current within the monitor chambers; the scale factor is adjusted during calibration such that 1 MU delivers a dose of 1 cGy at a reference depth under reference conditions [Almond et al., 1999].

The dose from a photon beam incident on a surface rapidly increases to a maximum at a depth of a few centimeters, depending on the mean photon energy and field size, then steadily decreases with depth as the photon fluence is attenuated. Consequently, healthy tissue superficial to the target volume receives a greater dose from any given beam. To minimize the volume of healthy tissue receiving a therapeutic dose, EBRT treatments are typically comprised of multiple discrete beams, also known as fields, or continuous arcs focused at the target volume. The arrangement of the beams and the dose delivered per beam are determined during the treatment planning process.

2.2.1 External-beam radiation therapy treatment planning

2.2.1.1 Treatment simulation

Preparation of an EBRT treatment plan requires visualization of the internal patient anatomy to localize the diseased tissue and identify critical healthy tissue that must be spared. The patient anatomy is most commonly imaged using computed tomography (CT). Radioopaque markers are placed on the surface of the patient for the CT scan to provide an external reference of the internal patient anatomy for alignment during treatment. The values associated with the voxels of a CT image are in terms of Hounsfield units (HU), which are defined as

$$HU(x,y) = \frac{\mu(x,y) - \mu_{\text{water}}}{\mu_{\text{water}}} \times 1000, \tag{2.1}$$

where $\mu(x, y)$ is the mean linear attenuation coefficient of the material in the voxel located at (x, y), and μ_{water} is the linear attenuation coefficient of water. An image-value-to-density table (IVDT), which is determined from a CT scan of materials of a known range of densities, is used to convert HU to electron density. The electron density of the patient is required for the dose calculation, as discussed in Sec. 2.2.1.3.

For many lung treatments, especially SBRT procedures, a four-dimensional CT (4DCT) scan is performed during simulation to measure the motion of the tumor [Ford et al., 2003; Vedam et al., 2003]. During a 4DCT scan, a surrogate for the tumor motion (i.e., chest wall motion for lung tumors) is monitored. Based on the observed surrogate motion as a function of time, the time-stamped CT images are binned according to either the motion phase or the motion amplitude at the time of acquisition. 4DCT scans are oversampled to acquire a full CT dataset for each tumor motion bin.

Typically, only a single CT simulation is performed for a patient, making the assumption that the internal anatomy and tumor motion do not change substantially over the course of treatment. If substantial anatomical changes, especially weight loss, are observed during treatment, then the treatment simulation can be repeated and a new treatment plan prepared.

2.2.1.2 Volume definition

The International Commission of Radiation Units and Measurements (ICRU) report 50 [ICRU50, 1993] defines several volumes to be delineated on an image of the patient anatomy during treatment planning to facilitate the creation and evaluation of the plan. The gross tumor volume (GTV) is the palpable or visible extent of the disease. The clinical target volume (CTV) is an expansion of the GTV that includes subclinical microscopic disease. For the treatment to be successful, the CTV must receive sufficient dose. The planning target volume (PTV) applies margins to the CTV to account for motion due to changes in internal

anatomy and setup errors. Whereas the GTV and CTV denote anatomical volumes within the patient, the PTV considers positioning uncertainties and defines a volume relative to the linear-accelerator geometry in which the CTV is contained. van Herk et al. [2000] provide an analytical recipe for the CTV-to-PTV margin to ensure that the CTV receives a minimum of a selected percentage of the prescription dose for a given percentage of a patient population. The proposed recipe separately considers systematic positioning errors, which arise during treatment preparation, and random positioning errors, which occur during treatment delivery. However, treatment margins must also consider the dose tolerances of surrounding healthy tissues, which are contoured as organs at risk (OAR), to minimize the occurrence of toxicities.

ICRU report 62 [ICRU62, 1999] refines the volume definitions of ICRU report 50, specifying an internal target volume (ITV) to distinguish between motion due to changes in the internal anatomy and motion due to setup errors. The ITV is determined by an expansion of the CTV to account for the internal excursion of the target volume. The maximum intensity projection (MIP) of the 4DCT, in which each voxel is assigned the maximum value of the corresponding voxels from each of the binned CT datasets, is generated to contour the ITV. Because the lung tumor is much more dense than the surrounding lung tissue, the MIP readily identifies voxels through which the tumor passes at any point in the respiratory cycle.

2.2.1.3 Dose calculation

Once the treatment geometry is defined and the volumes of interest are contoured, the dose to the patient is calculated. To obtain the desired accuracy in the dose calculation within a clinically feasible period of time, a convolution-superposition algorithm is used to calculate the dose. The convolution dose calculation method was developed by Mackie et al. [1985]. This method uses energy deposition kernels that provide the distribution of energy

deposition surrounding a primary photon interaction site. The energy deposition kernels are precalculated within a water medium, thus reducing computation time for the actual dose calculation. Given these energy deposition kernels, the dose at a vector coordinate $\boldsymbol{r}$, $D(\boldsymbol{r})$, from an interaction at a vector coordinate $\boldsymbol{r'}$ in a homogeneous medium is given by

$$D(\boldsymbol{r}) = \int T(\boldsymbol{r'})A(\boldsymbol{r} - \boldsymbol{r'})d^3\boldsymbol{r'}, \tag{2.2}$$

where $A(\boldsymbol{r} - \boldsymbol{r'})$ is the energy deposition kernel and $T(\boldsymbol{r'})$ is the terma distribution, given by

$$T(\boldsymbol{r'}) = \frac{\mu}{\rho} h\nu\Phi(\boldsymbol{r'}), \tag{2.3}$$

where $\frac{\mu}{\rho}$ is the mass attenuation coefficient, which is determined from the CT simulation, $h\nu$ is the photon energy, and $\Phi(\boldsymbol{r'})$ is the primary fluence distribution [Papanikolaou et al., 1993]. Each term in Eq. 2.2 is energy dependent, so a second integration over the range of photon energies is performed for polyenergetic beams. The dose in heterogeneous media is calculated by range scaling the energy deposition kernels according to the density of the medium of interest [O'Connor, 1984]. In low-density lung tissue, for instance, the range of electrons increases relative to that in water, so the energy deposition kernels are correspondingly expanded. However, the kernel scaling method for the calculation of dose in heterogeneous media has limited accuracy in regions of lateral charged particle disequilibrium, primarily near interfaces of materials with different densities [Ahnesjö, 1989; Woo and Cunningham, 1990].

2.2.2 External-beam radiation therapy treatment delivery

2.2.2.1 Three-dimensional conformal radiation therapy

Conventional treatment planning employs a trial-and-error process to assign delivery parameters and calculate the resulting dose distribution until a suitable plan is obtained.

Treatments are delivered with either a static gantry, in which the target is irradiated from multiple discrete beam angles, or a dynamic gantry, where the gantry rotates continuously through a planned arc during treatment. Three-dimensional conformal radiation therapy (3DCRT) positions the MLC to conform to the projection of the target volume in the plane through the isocenter normal to the beam axis. 3DCRT arc treatments, known as dynamic conformal arcs, continuously reposition the MLC as the projection of the target volume changes with the gantry angle. In 3DCRT, each beam or arc delivers a uniform fluence.

2.2.2.2 Intensity-modulated radiation therapy

The concept of inverse optimization, in which the ideal fluence distribution is determined for an input set of dose constraints, was introduced by Brahme [1988]. The optimized fluence distributions are non-uniform and cannot be delivered by conventional means. Webb [1991; 1992] developed an inverse-optimization technique in which the optimal fluence distributions are delivered by modulating the beam intensity with dynamic MLC positioning, and demonstrated that such a technique could deliver more conformal dose distributions than conventional techniques. This treatment technique is known as IMRT. As with 3DCRT, IMRT can be delivered with either a static or dynamic gantry. For static gantry treatments, MLC-based IMRT can be delivered using either the sliding window technique (SW-IMRT) or the step-and-shoot technique (SS-IMRT). In SW-IMRT the radiation beam remains on while the MLC leaves translate across the field to produce the desired fluence distribution. SS-IMRT separates the delivery of each field into several MLC arrangements, or segments, and the beam is turned off as the MLC leaves transition between segments. Beam intensity can also be modulated with a solid compensator, which is fabricated in the shape of the negative of the desired fluence distribution, or by electromagnetically scanning the electron beam across the transmission target to generate the desired fluence distribution. IMRT delivered with a dynamic gantry is known as volumetric modulated arc therapy (VMAT).

In VMAT treatments, the gantry rotation speed, dose rate, and MLC position are all directly optimized, and thus can vary continuously throughout the treatment. This thesis work considered only SS-IMRT delivery.

MLC-based IMRT treatments, whether SS-IMRT, SW-IMRT, or VMAT, are typically comprised of numerous different complex MLC arrangements to achieve the necessary modulation for the desired dose distribution. As a result, the dose delivered from these treatments is sensitive to both the quality of the MLC model in the treatment planning software (TPS) and to the accuracy of the MLC position during treatment. To verify that the treatment can be delivered as planned, delivery quality assurance (DQA) is completed prior to the initiation of treatment. DQA is performed by copying the planned incident fluence distribution to a CT dataset of a dosimeter in-phantom, typically a planar or array dosimeter, and calculating the dose distribution in the phantom geometry. The treatment is then delivered to the phantom, and the delivered dose distribution is measured. The measured and calculated dose distributions are spatially registered and compared to verify agreement within tolerances.

The standard metric for the comparison of two dose distributions is the gamma index, which is a quantitative combination of dose-difference and distance-to-agreement (DTA) evaluations [Low et al., 1998]. A dose-difference evaluation determines the percentage difference in dose between corresponding coordinates in the reference and evaluated distributions, and is sensitive to small positioning errors in regions of high dose gradient. The DTA evaluation serves as a complement to the dose-difference evaluation, determining for each coordinate in the reference distribution the minimum distance to a coordinate in the evaluated distribution with the same dose. Interpolation of the evaluated distribution is typically required to locate a point at which the dose agrees exactly with the reference distribution. The DTA evaluation is not commutative, so the higher-resolution distribution is normally

chosen as the evaluated distribution to minimize the distance between interpolated data points. The gamma index combines the dose-difference and DTA evaluations as follows:

$$\gamma(\boldsymbol{r}_{\text{ref}}) = \min\{\Gamma(\boldsymbol{r}_{\text{ref}}, \boldsymbol{r}_{\text{eval}})\}\forall\{\boldsymbol{r}_{\text{eval}}\}, \tag{2.4}$$

where

$$\Gamma(\boldsymbol{r}_{\text{ref}}, \boldsymbol{r}_{\text{eval}}) = \sqrt{\frac{\|\boldsymbol{r}_{\text{ref}} - \boldsymbol{r}_{\text{eval}}\|^2}{\Delta d^2} + \frac{[D(\boldsymbol{r}_{\text{eval}}) - D(\boldsymbol{r}_{\text{ref}})]^2}{\Delta D^2}}, \tag{2.5}$$

$\boldsymbol{r}_{\text{ref}}$ and $\boldsymbol{r}_{\text{eval}}$ are coordinates in the reference and evaluated distributions, respectively, $D(\boldsymbol{r})$ is the dose at $\boldsymbol{r}$, and Δd and ΔD are the tolerances for the DTA and dose-difference evaluations, respectively. A γ value less than or equal to unity indicates agreement between the compared distributions within the defined tolerances. Standard tolerances are 95 % agreement within a dose difference of 3 % and a DTA of 3 mm [Ezzell et al., 2009]. Like the DTA evaluation, the gamma index is not commutative.

2.3 Impact of respiratory motion on external-beam radiation therapy

As discussed in Sec. 2.2.1.2, target motion is accounted for in a treatment plan with increased treatment margins to ensure that the target remains within the treated volume. However, the planned dose distribution is calculated on a static image of the patient. Therefore, patient motion during treatment results in delivery errors relative to the planned dose. This section discusses the impact of target motion on the delivered dose distribution.

2.3.1 Respiratory motion

Respiration is cyclical. During inhalation the diaphragm contracts and descends, causing the lungs to expand and fill with air. The opposite occurs during exhalation: the diaphragm

relaxes and ascends, expelling air from the lungs. Consequently, the motion of internal organs due to respiration is periodic, with the greatest component along the superior-inferior axis [Korin et al., 1992]. Given the cyclical and primarily one-dimensional nature of respiratory motion, Lujan et al. [1999] proposed the following parameterization to describe the position, $z(t)$, of organs that move with respiration:

$$z(t) = z_0 - b\cos^{2n}(\pi t/\tau - \phi), \tag{2.6}$$

where z_0 is the organ position at full exhale, b is the amplitude of the motion, τ is the period of the breathing cycle, ϕ is the initial phase of the breathing cycle, and n is a parameter that dictates the asymmetry of the respiratory motion (i.e., incongruence of time spent in full inhale and exhale phases). In an application of Eq. 2.6 to 331 respiratory traces measured from 24 patients, George et al. [2005] found that the correlation coefficients describing the quality of the fits were similar for $n = 1$ and $n = 2$, demonstrating that respiratory motion can be well-modeled with a symmetric waveform. Many studies of respiratory motion that utilize Eq. 2.6 use representative values of 1 cm to 2 cm and 3 s to 5 s for the amplitude and period, respectively [Jiang et al., 2003; Berbeco et al., 2006; Seco et al., 2007]. One limitation of Eq. 2.6 is the assumption of a constant amplitude and period. Cycle-to-cycle variations in respiratory motion parameters have been observed in numerous studies [Tobin et al., 1983a,b; Bruce, 1996; Blackall et al., 2006]. Furthermore, nonnegligible drifts in baseline position have been observed during respiration [Engelsman et al., 2005; Shirato et al., 2006; Trofimov et al., 2008; Zhao et al., 2011]. Kissick et al. [2008] proposed a revised model for respiratory motion to incorporate the time dependence of the motion parameters:

$$z(t) = z_0(t) + b(t)\cos^{2n}[\pi t/\tau(t)], \tag{2.7}$$

where the time dependence of the motion parameters is modeled by applying offsets randomly sampled from rectangular distributions to the mean values of the motion parameters.

Both Eq. 2.6 and Eq. 2.7 make the assumption that respiratory motion is one-dimensional. However, from fluoroscopic monitoring of gold markers implanted in or near lung tumors in twenty patients, Seppenwoolde et al. [2002] observed motion along the lateral and anterior-posterior axes in some patients that was comparable to the motion component along the superior-inferior axis. Additionally, hysteresis was observed in the motion of many tumors, in which phase differences between the motion components along the three axes resulted in different trajectories during inhale and exhale.

2.3.2 Blurring effect

As previously discussed, the planned dose distribution is calculated on a static image of the patient. However, due to respiration, the internal anatomy of the patient moves during treatment. The motion of the internal anatomy results in the blurring of the planned dose distribution. The planned dose is averaged over the path of respiratory motion, reducing dose gradients. Thus, blurring errors are dependent on the motion trajectory (i.e., amplitude and baseline trends) but not the motion frequency. Assuming that the internal anatomy does not deform with respiration (i.e., only rigid translations or rotations) and that the spatial dose distribution does not vary with motion, then the blurred dose distribution, which is the expected delivered dose in the presence of motion, is given by the convolution of the static dose distribution and the probability density function (PDF) of the tumor position. However, errors of up to 5 % have been observed when the convolution method is used to estimate the blurred dose distribution in the lung [Beckham et al., 2002; Craig et al., 2003].

Portions of the anatomy that do not move outside regions of planned uniform dose are unaffected by blurring. Furthermore, the dose to a given voxel can be no less than the

planned minimum dose over the trajectory of that voxel. Therefore, the delivery errors of greatest consequence due to dose blurring are restricted to the periphery of the target volume, where broadening of the planned penumbra results in a dose deficit. These errors are accounted for with the use of increased treatment margins, as discussed in Sec. 2.2.1.2 with the definition of the ITV, or with motion management to restrict the extent of the motion during treatment, as discussed in Sec. 2.3.4.

2.3.3 Interplay effect

While blurring errors are limited to regions of non-uniform dose, Yang et al. [1997] demonstrated in an investigation of tomotherapy treatments that exposure of an oscillating target with a slit beam translating along the axis of oscillation could produce dose perturbations within the treated volume. For a given target motion amplitude, the dose perturbations varied with the motion frequency, reaching a maximum when the target and beam moved with similar speeds. This observation was verified by Yu et al. [1998], and later refined by Kissick et al. [2005], which found delivery errors in excess of 300 % relative to the treatment of a static target. The delivery errors were attributed to interplay between the motion of the beam and the target. The concept of interplay is illustrated in Fig. 2.1, reproduced from Bortfeld et al. [2002]. The two stars indicate the same point at different phases (i.e., inhalation and exhalation) of the same motion trajectory. It is apparent that the dose received by the highlighted point is dependent on the initial phase of the motion. Interplay errors are distinct from blurring errors because, while changes in motion amplitude will minimally impact the dose to the marked point, changes in motion frequency will greatly impact the delivered dose.

The concept of interplay was further refined by Kissick et al. [2008], which proposed that interplay could be interpreted as interference between the characteristic modulation frequencies of the treatment delivery and the motion frequency of the target. Potential

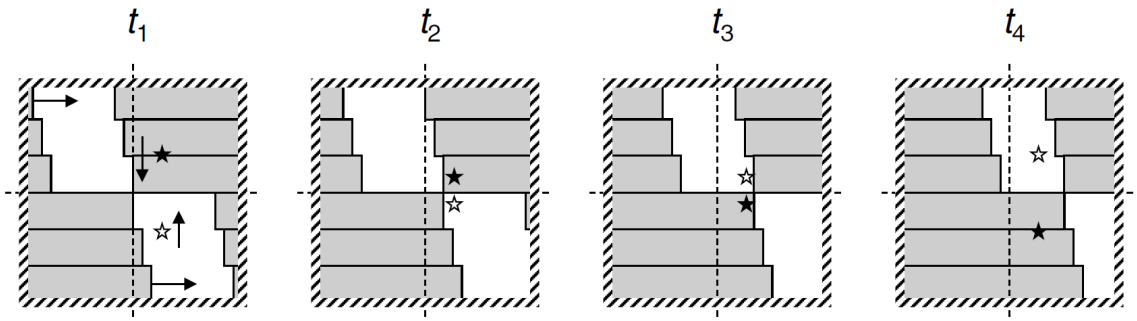

Figure 2.1: Illustration of the interplay effect from Bortfeld et al. [2002]. The four panels illustrate advances in time ($t_4 > t_3 > t_2 > t_1$) in the delivery of a treatment. The two stars indicate the same point at different phases of the same motion trajectory. Depending on the initial phase of motion, the indicated point is either shielded or exposed for the entire treatment.

modes of delivery modulation include couch motion in tomotherapy treatments, changes in dose rate in VMAT treatments, and changes in the positioning of the MLC and the gantry. In the case of SS-IMRT treatments, interplay errors arise when the beam-on times for individual beam angles or MLC segments are comparable to the target motion period, resulting in insufficient sampling of the target position PDF. Consequently, the delivered dose is dependent on the initial phase of the motion as it determines which portion of the target position PDF is sampled. This concept is illustrated in Fig. 2.2, which demonstrates the treatment of a target oscillating with period T using a field modulated with a period of T_{G} [Kissick et al., 2012]. In the limit that the target motion period is much shorter than the duration of MLC segments or beam angles, the target position PDF is well-sampled, and the dependence of the delivered dose on the initial phase of motion is minimized. In this limit, there are only blurring errors. In the opposite extreme, if the target motion period is much longer than the duration of segments or beams, then the limit of a static geometry is approached. The nodes in the figure indicate values of T_G that are integral multiples of T. In these cases the target position PDF is fully sampled, and the delivery errors reduce to zero.

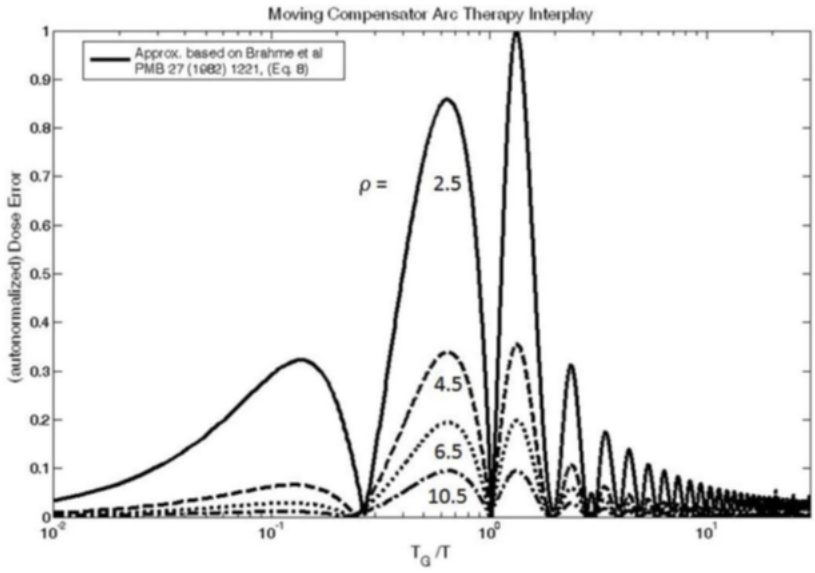

Figure 2.2: Plot of delivery errors determined analytically for the treatment of a circular target oscillating with period T with a beam modulated with period T_G. As the target motion period becomes relatively short, the motion PDF becomes well-sampled and the limit of blurring errors is approached. As the target motion period becomes increasingly long, the limit of a static geometry is approached. ρ indicates the radius within the target at which errors were accumulated. Figure reproduced from Kissick et al. [2012].

To summarize the types of treatment errors due to respiratory motion, the blurring effect is a systematic offset of the planned dose distribution due to differences in the patient anatomy during treatment planning and delivery, while the interplay effect manifests as random variations in the delivered dose from the expected, blurred dose distribution due to a dependence on the initial phase of motion. While blurring errors only occur in regions of non-uniform dose, primarily near the periphery of the target volume, interplay errors can occur throughout the treated volume.

2.3.4 Respiratory motion management

The expansion of treatment margins to mitigate delivery errors due to respiratory motion is limited by the dose tolerances of healthy tissue. Therefore, in addition to the use of increased treatment margins, measures are taken to restrict the motion of the target volume during treatment. Respiratory motion management techniques include respiratory gating, breath hold, abdominal compression, and real-time tumor tracking.

During respiratory-gated treatments, the target position is monitored, and radiation is only delivered when the target lies within a predefined range of positions, termed the gate. The gate can be defined in terms of the phase or the amplitude of the target motion. The width of the gate determines the residual amplitude of the target motion during treatment [Berbeco et al., 2005]. The target motion is typically monitored via a surrogate external marker, such as the chest wall, but radiographic imaging of fiducial markers implanted in or near the target volume can also be used [Shirato et al., 2000]. Gates centered about the full-exhale or full-inhale positions are commonly selected. The exhale position is more reproducible, but lung volume is greatest during the inhale phase, thereby decreasing the relative volume of treated lung tissue and improving lung sparing [Vedam et al., 2001].

Breath-hold treatments are similar to gated treatments, but the initiation and termination of radiation delivery is performed manually, and the patient is not permitted to

breathe freely. Instead, the patient inhales to and maintains a reproducible lung volume; while breath is held, radiation is delivered. To improve the reproducibility of the lung volume during breath hold, a spirometer can be used to monitor the volume of air flow in and out of the lungs [Hanley et al., 1999]. A more invasive option is active-breathing control, in which the spirometer is connected to a balloon valve, forcing a breath hold at a specified lung volume [Wong et al., 1999].

Rather than limit radiation delivery to a select range of the target motion waveform, abdominal compression restricts the amplitude of respiratory motion. Compression of the abdomen limits the contraction of the diaphragm, and therefore reduces the excursion of the target volume due to respiration [Lax et al., 1994]. Because the motion amplitude is reduced, radiation can be delivered over the entirety of the respiratory cycle, thereby improving the efficiency of treatments using this motion-management technique relative to respiratory gating and breath hold.

A primarily experimental motion-management technique is real-time MLC tracking, in which the planned MLC positions are continuously adjusted to track the motion of the target volume. This technique requires monitoring of the target position, prediction of future target motion to account for the latency in MLC positioning, revision of planned MLC positions during treatment, and adaptive treatment planning to reconstruct and accumulate the delivered dose [Cho et al., 2009]. The first clinical implementation of real-time MLC tracking was recently completed for a prostate cancer patient [Keall et al., 2014].

2.4 Project motivations and goals

2.4.1 Recommendations of Task Group 76

The report of Task Group 76 of the AAPM addresses the implementation of respiratory motion management techniques [Keall et al., 2006]. This Task Group recommends the con-

sideration of respiratory motion management if the amplitude of motion exceeds 5 mm or if significant sparing of healthy tissue can be achieved. As noted by Kissick and Mackie [2009], the basis of criteria for the use of motion management on motion amplitude alone disregards the frequency dependence of interplay errors. The Task Group 76 report justifies the exclusion of interplay considerations from its recommendations based on the results of analytical [Bortfeld et al., 2002] and experimental [Jiang et al., 2003] studies which demonstrated that interplay errors average out over the full course of a fractionated treatment. Each of these studies modeled respiratory motion as a regular, one-dimensional sinusoid that was invariant over the course of thirty fractions. With the assumption of a random motion phase at the start of each fraction, both studies found that the distribution of delivered doses over a full treatment course had a standard deviation of 1 % to 2 %, suggesting that interplay errors are negligible. However, the Task Group 76 report acknowledges that fractionation alone should not be relied upon to mitigate interplay errors, and calls for further investigation of the interplay effect under more realistic conditions.

2.4.2 Review of interplay investigations

Following the release of the Task Group 76 report, numerous analytical, experimental, and computational studies of the interplay effect have been completed. Berbeco et al. [2006] investigated interplay errors in the delivery of individual fields, single fractions, and thirty-fraction treatments of a five-field SS-IMRT treatment plan. Using radiographic film, the dose distribution of each field was separately measured for eight equally spaced initial phases of a one-dimensional, sinusoidal motion waveform. The dose distribution for a treatment fraction was compiled by randomly sampling the motion phase for each field and summing the respective distributions. The maximum standard deviation in delivered dose per pixel over 1000 compilations of dose distributions was reduced from 5.4 % for a single fraction

to 0.71 % for thirty fractions, indicating that variations in delivered dose due to interplay become negligible over a full treatment course.

Court et al. [2010b] completed a more comprehensive experimental investigation of interplay errors, considering conventionally fractionated SS-IMRT, SW-IMRT, and VMAT treatment plans prepared by three separate treatment planning systems. Each field of each treatment plan was individually measured for multiple random initial phases of a one-dimensional surrogate motion waveform recorded during treatment of a lung patient. Measurements were made with twenty micro-metal-oxide-semiconductor field-effect transistors (MOSFETs) implanted within a 3D-printed tumor model, which was made to move within an anthropomorphic thorax phantom. Dose distributions for treatment fractions were compiled as in Berbeco et al. [2006]. The expected delivered dose per fraction was estimated as the mean dose over an infinite number of fractions. The number of fractions required for 95 % of the delivered dose distribution to agree with the expected dose within 5 % was determined, and only a single-arc VMAT plan with intentionally increased complexity required more than five fractions to achieve the specified agreement, suggesting that interplay errors are rapidly averaged out with fractionation.

Whereas Berbeco et al. [2006] and Court et al. [2010b] considered the impact of fractionation on interplay errors, several other studies investigated the sources of interplay errors and methods to mitigate them. Seco et al. [2007] considered the impact of planned MU per segment on the magnitude of interplay errors in SS-IMRT treatments. Fewer MU per segment results in shorter segment delivery times, which in turn deteriorates the sampling of the target position PDF. In an analysis of approximately 3000 clinical IMRT beams, it was found that more than 80 % of the segments delivered 5 MU or less, accounting for more than half of the total dose delivered. Ionization chamber measurements were completed for field sizes of 4×4 cm^2, 6×6 cm^2, and 10×10 cm^2 for ten equally spaced initial phases of a one-dimensional, sinusoidal motion waveform. For each field, measurements were taken for

several MU settings, resulting in delivery times ranging from 1 s to 48 s. Compiling these measurements as in Berbeco et al. [2006] to simulate conventionally fractionated treatment deliveries with segments of constant MU, a standard deviation in dose per fraction of up to 35 % resulted for segment delivery times less than half of the motion period. Therefore, even over a treatment of thirty fractions, a prominence of segments that are comparable to the motion period in duration can produce substantial interplay errors.

Based on the results of Seco et al. [2007], increasing the segment delivery time relative to the motion period should reduce interplay errors. Court et al. [2008] completed a comprehensive investigation of interplay errors in SW-IMRT in an effort to determine the maximum dose rate for which the dose delivered for each fraction is within ± 10 % of the planned dose, given the observation that the biological effectiveness of a given fractionation schedule can be impacted if the standard deviation in dose per fraction exceeds 10 % [Bortfeld and Paganetti, 2006]. The dose distribution from a slit field defined by the MLC incident on a water-equivalent-plastic phantom was calculated for MLC separations ranging from 0.2 cm to 5.0 cm. Simulations were then completed in which the dose to the central $4 \times 4 \times 4$ cm^3 volume of the phantom was accumulated as the phantom underwent one-dimensional sinusoidal oscillations and the dose distribution stepped across the phantom. Separate simulations were performed for eight equally spaced initial phases of motion. The resulting differences in accumulated dose from the planned dose were determined for a range of MLC speeds, target motion amplitudes, and target motion periods. For a given MLC separation and target motion waveform, the maximum MLC speed, and therefore maximum dose rate, for which delivery errors were less than 10 % was determined.

While the methods of Court et al. [2008] were demonstrated to prevent per-fraction delivery errors exceeding 10 %, the required universal reduction in the treatment dose rate can produce prohibitively long treatments. In an investigation of interplay errors in SS-IMRT, Ehler and Tomé [2009] proposed a method of selective dose-rate modulation in which

only the fields that are most susceptible to interplay errors are delivered with a reduced dose rate. Using a 3D target motion kernel determined from a ten-phase 4DCT dataset and planar dose calculations for each beam segment, the delivered dose over ten fractions of 2 Gy was determined for dose rates ranging from 100 MU/min to 500 MU/min, assuming a random initial phase of motion for each fraction. The mean standard deviation in dose per fraction over the projected area of the target volume was determined for each field and dose rate to identify which fields demonstrated the greatest reduction in interplay errors with a reduction in dose rate. Application of this technique reduced the range of standard deviation in dose per fraction for individual fields from 1-18 % to 0.1-9 %.

Many recent investigations of interplay errors have developed methods to more accurately calculate dose in the presence of motion, either for the purpose of post-treatment dose reconstruction or pre-treatment error prediction. Litzenberg et al. [2007] developed a technique in which delivered dose is reconstructed using Monte Carlo simulations. The technique uses log files from the linear accelerator, which record the MLC position and beam status every 50 ms, and the motion of electromagnetic transponders implanted in the target volume measured during treatment. During the simulation of a treatment delivery, the time is sampled from a rectangular distribution prior to the transport of each new source particle. If the beam was on at the sampled time, then the MLC position and target position are determined from the log file and motion trace, respectively. To simulate motion, the position of the isocenter within the CT dataset is shifted opposite of the observed motion. This dose reconstruction technique was extended by Jensen et al. [2012] to include compatibility with 4DCT datasets. Instead of modeling target motion by shifting the isocenter, each particle is transported through the appropriate phase of the 4DCT dataset based on the phase of the motion at the sampled time. This approach models the deformation of the anatomy with respiration; however, it requires the use of deformable registration to combine the resulting dose distributions calculated on each phase.

A method to estimate the maximum interplay errors for a given treatment plan prior to delivery was developed by Li et al. [2012; 2013]. On a 4DCT dataset of the patient, the dose distribution from the planned treatment is calculated separately for each phase. The expected dose delivered to the moving target is determined as the mean of the doses calculated on each phase using deformable registration. The bounds of potential interplay errors are found by determining the maximum and minimum doses delivered to each voxel over the phases of the 4DCT dataset and taking the difference from the expected dose.

Although many investigations of the interplay effect have been completed, assumptions made by the authors for simplicity limit the applicability of the results. These assumptions include one-dimensional respiratory motion [Berbeco et al., 2006; Court et al., 2008, 2010b] and invariance of respiratory motion within [Berbeco et al., 2006; Seco et al., 2007; Court et al., 2008] and between fractions [Berbeco et al., 2006; Seco et al., 2007; Court et al., 2010b]. Perhaps the most egregious assumption is the constancy of the baseline position of the target volume. Kissick et al. [2008] demonstrated for tomotherapy treatments that the dose delivered to a target following a motion defined by Eq. 2.7 exhibits modulations in regions of planned uniform dose. However, these modulations were not observed when the target volume followed a regular, sinusoidal motion with a period and amplitude representative of typical respiratory motion. The dose modulations were attributed to interference of the low-frequency variation in the baseline position of the target with the couch motion. This same conclusion was reached by Chaudhari et al. [2009], which simulated the dose delivered in tomotherapy treatments of a target that moved according to measured surrogate motion waveforms. With motion amplitudes of as little as 5 mm, delivery errors in excess of 10 % were observed in regions of planned uniform dose.

Tudor et al. [2014] extended the investigation of interference between patient motion frequencies and characteristic treatment delivery frequencies in tomotherapy treatments. The dose delivered from a tomotherapy treatment to a phantom that followed measured

surrogate motion waveforms was calculated. The calculations were then repeated after applying frequency filters to the motion waveforms corresponding to the characteristic frequency ranges of MLC motion, gantry motion, and couch motion. It was determined that the great majority of the delivery errors resulted from low-frequency drifts in the target position within the characteristic frequency range of couch motion. Dose errors of up to 9.0 % were observed for a peak-to-peak motion amplitude of only 3 mm, which is below the threshold for motion management recommended by AAPM Task Group 76 [Keall et al., 2006]; these errors were reduced to 1.3 % when the variations in baseline position were filtered out. Therefore, failure to consider the low-frequency components of respiratory motion results in substantial underestimation of interplay errors.

It is apparent that the use of Eq. 2.6 to model respiratory motion neglects the low-frequency components of motion. However, a 4DCT scan cannot provide a faithful measurement of tumor position as a function of time over an extended period, either. Although a 4DCT scan is acquired over a series of respiratory cycles, the images are binned to create a full dataset of a single respiratory cycle; the assumption is made that all subsequent respiratory cycles follow the same motion. Furthermore, a 4DCT scan requires approximately one minute to complete, whereas the time between the start and end of radiation delivery in a typical treatment fraction can be five to ten minutes. The difference in time scales between imaging and treatment could result in the failure to resolve positional drifts that occur over the course of a treatment. For instance, Richter et al. [2011] observed that baseline drifts of 10 mm, 6 mm, and 4 mm within a motion with an amplitude of 23 mm over a 60 s, 120 s, and 240 s period, respectively, could not be resolved by a 4DCT scan, which required approximately 60 s. Therefore, dose reconstruction and interplay error prediction techniques that employ 4DCT scans may not accurately quantify potential errors resulting from low-frequency components in tumor motion [Jensen et al., 2012; Li et al., 2012, 2013].

2.4.3 Project goals

As has been discussed in this chapter, current recommendations for the use of respiratory motion management consider only the amplitude of the observed motion, making the assumption that frequency-dependent errors average out over the delivery of multiple treatment fractions [Keall et al., 2006]. However, the studies that were referenced as evidence that interplay errors average out over many fractions modeled respiratory motion as regular, one-dimensional sinusoids with representative motion parameters [Bortfeld et al., 2002; Jiang et al., 2003]. Ensuing studies of tomotherapy treatments demonstrated that substantial delivery errors could occur in the presence of irregular target motion, even with a motion amplitude below the recommended threshold for the use of respiratory motion management, due to interference between the couch motion and low-frequency drifts in the target motion [Kissick et al., 2008; Chaudhari et al., 2009; Tudor et al., 2014]. Corresponding investigations of interplay errors due to irregular target motion during treatments with C-arm linear accelerators, though, have not been completed. As asserted by Kissick and Mackie [2009], characteristic delivery modulation frequencies vary between treatment modalities, requiring separate characterization of each modality to develop appropriate frequency-dependent criteria for the management of respiratory motion.

The overall goal of this project was to characterize delivery errors due to the interplay effect in SS-IMRT treatments of the lung. Monte Carlo simulations were used to quantify interplay errors over a comprehensive range of target motion frequencies. To that end, a Monte Carlo model of a linear accelerator was developed and experimentally validated. To verify the simulations of the interplay effect, a 3D radiochromic film stack dosimeter was developed and characterized. Measurements of interplay errors in the delivery of SS-IMRT plans were made using the film stack dosimeter and compared with simulated results. Using Monte Carlo simulations, interplay errors over individual treatment fractions and complete treatment courses, both conventionally fractionated and hypofractionated, were quantified.

The results of this work provide an experimental basis for the recommendation of frequency-dependent respiratory motion management criteria.

Chapter 3

Film and TLD dosimetry methods

3.1 Film dosimetry methods

3.1.1 Radiochromic film

Radiochromic films are high-resolution, planar dosimeters that undergo a color-changing chemical reaction when exposed to radiation. The change in the optical density (OD) of the film due to exposure can be measured using a laser densitometer or, more commonly, a flatbed document scanner [Devic et al., 2004; Paelinck et al., 2007]. With calibration, the change in the OD of the film can be equated to the dose received by the film.

Ashland Specialty Ingredients (Wilmington, DE) manufactures radiochromic film under the Gafchromic® trade name. Gafchromic® film dosimeters are nearly tissue equivalent, and their response to ionizing radiation is independent of dose rate and minimally dependent on energy for energies above 100 keV. However, the response of Gafchromic® films is dependent on temperature and humidity during storage, exposure, and readout, so it is recommended that a consistent procedure be followed for the storage and handling of the films [Niroomand-Rad et al., 1998].

The Gafchromic® external-beam-therapy (EBT) line of radiochromic films has been specifically designed for use in external-beam-therapy applications, with a minimum sensitivity of 1 cGy. These films have an active layer comprised of needle-shaped diacetylene monomers that form cross-links when exposed to radiation. This polymerization reaction turns the colorless active component blue, creating a primary absorption peak within the red range of the visible spectrum at a wavelength of 636 nm. The rate of the polymerization reaction quickly saturates after exposure, but remains nonzero for an extended time [Martišíková et al., 2008].

There have been three models of Gafchromic® EBT film: EBT (which has been discontinued), EBT2, and EBT3. Cross-section views of the three film models are shown in Fig. 3.1. The cross section of EBT film is symmetric, with two 17 μm-thick active layers each adhered to a polyester substrate and separated by a surface layer. Unlike EBT film, EBT2 film is asymmetric, with a single, thicker active layer, although a slightly reduced total active thickness. To improve stability between production lots of films, the gelatin binder from EBT film was replaced with a synthetic polymer. The most apparent difference between EBT and EBT2 film is the yellow color of the latter, which comes from a marker dye incorporated into the active layer. This marker dye reduces the sensitivity of EBT2 film to ambient light [Andrés et al., 2010]. The differences between EBT2 and EBT3 film are relatively minor. EBT3 film has a symmetric cross section and silicon spheres incorporated into the polyester film surfaces to reduce the severity of Newton's ring artifacts when the film is read with a flatbed scanner. Newton's ring artifacts are interference patterns from multiple reflections between the film and flatbed surfaces that arise due to nonuniform contact between the film and the glass scanner bed. EBT3 film was determined to be much more susceptible to damaged edges when cut; therefore, EBT2 film was chosen for this work.

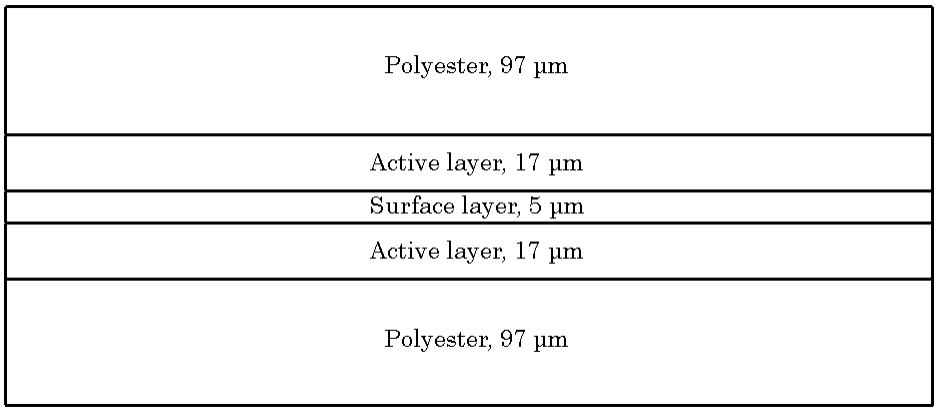

(a)

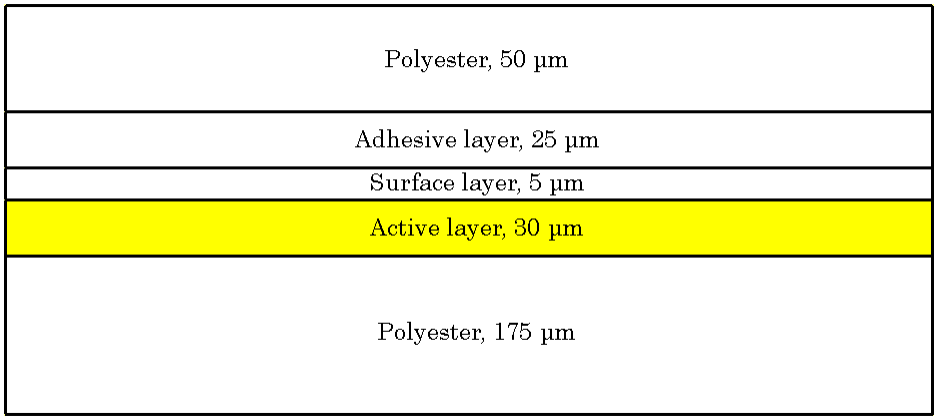

(b)

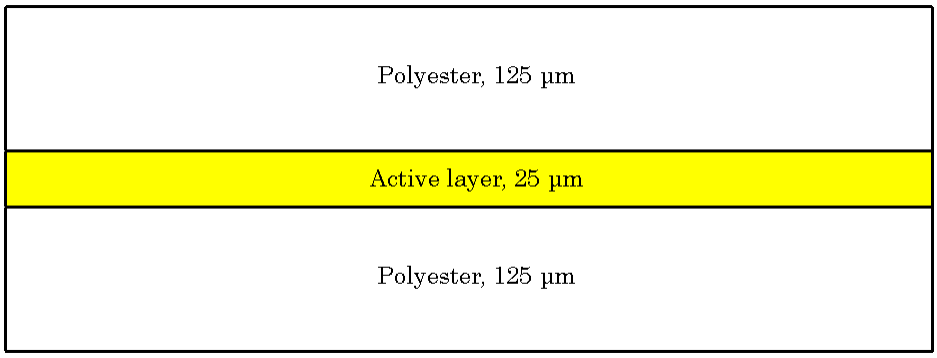

(c)

Figure 3.1: Cross sections of Gafchromic® (a) EBT, (b) EBT2, and (c) EBT3 film. Figures not to scale.

3.1.2 Film handling techniques

The films used for the characterization of the flatbed scanner, which is discussed in Sec. 3.1.4, were from lot A10061001B, while the films used in the development and characterization of the film stack dosimeter, which is discussed in Ch. 4, were from lot A06281101A. Films were handled at all times using latex gloves to minimize the accumulation of any surface contaminants. All films were stored together in an opaque envelope to minimize exposure to ambient light and to ensure consistent environmental conditions. For all film measurements, film pieces were cut from 20.3×25.4 cm^2 sheets. Changes in the OD of recently cut pieces of radiochromic film have been observed [Klassen et al., 1997]; therefore, all film pieces were cut at least one week prior to exposure. The measured OD of radiochromic films can vary 7 % to 13 % depending on the orientation of the film on the scanbed [Lynch et al., 2006; Andrés et al., 2010]. To ensure consistent orientation of the film pieces during readout, each piece was marked immediately after cutting to denote the orientation relative to the original film sheet.

3.1.3 Film scanning procedure

The films in this work were scanned using an EPSON® Expression® 10000XL flatbed document scanner (Epson America, Long Beach, CA), shown in Fig. 3.2. The scanner was set to professional mode, 48-bit color (16-bit depth in each of the red, green, and blue color channels), and a resolution of 72 dpi with all image adjustments turned off. Film images were saved in the tagged image file format.

The signal across the surface of the scanbed is nonuniform, reaching a maximum at the center of the scanbed and decreasing toward the edges [Lynch et al., 2006; Devic et al., 2006; Paelinck et al., 2007; Menegotti et al., 2008; Saur and Frengen, 2008; Ferreira et al., 2009]. To minimize the impact of this nonuniformity on film measurements, all films were scanned at the center of the scanbed where the signal is most uniform. The characterization

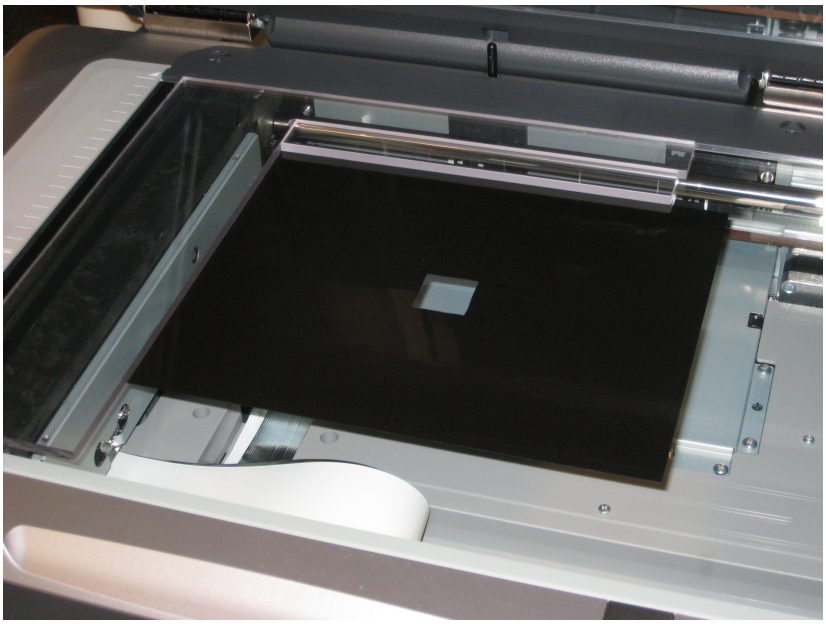

Figure 3.2: Image of the flatbed document scanner used to read films. The polycarbonate frame used for positioning reproducibility and the film masks are shown on the scanbed.

of the uniformity of the 10000XL scanner is discussed in Sec. 3.1.4.2. A polycarbonate frame and film masks cut from saturated radiographic films, shown in Fig. 3.2, were used to reproducibly position films at the center of the scanbed. The reproducibility of film positioning was verified using a film piece with a pin prick along each edge. The frame, mask, and pricked film were positioned on the scanbed and scanned. The entire setup was then removed, repositioned, and scanned again. The positions of the pin pricks in the images of the two trials agreed within one pixel (approximately 0.35 mm).

In addition to ensuring reproducible positioning of films on the scanbed, the film masks also prevented the detection of scattered light originating from outside the extent of the scanned film, which can result in an increased transmission signal near the edges of the film [Mersseman and De Wagter, 1998]. Two additional saturated radiographic films with central openings slightly smaller than the scanned films were stacked beneath the film mask. These additional films supported the edges of the scanned films and prevented any contact with the scanbed surface, thereby eliminating Newton's ring artifacts [Kairn et al., 2010].

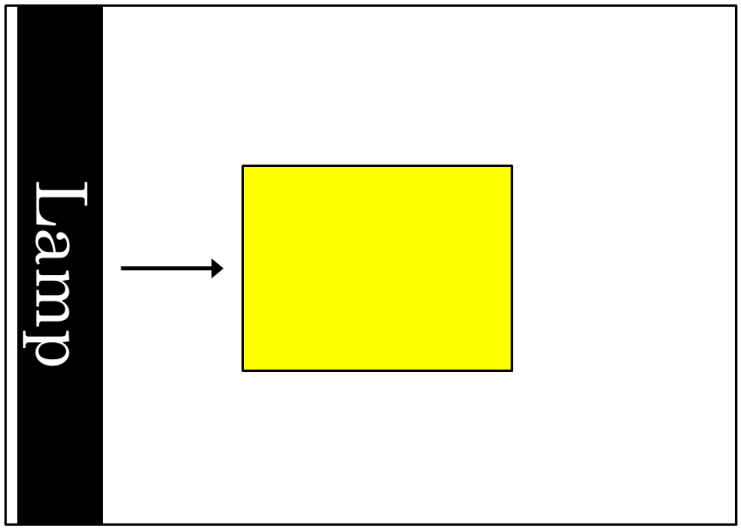

Figure 3.3: Schematic of the portrait scanning orientation. Relative to the original sheet of film, the film is positioned such that the long edge is parallel to both the long edge of the scanbed and the axis of translation of the scanner lamp.

Prior to scanning of films, five warm-up scans were taken of the empty scan bed. The upper transparency was then raised, and the scanner temperature was allowed to stabilize for 30 min. Each film was scanned once with the 50 μm polyester layer on top. All films were scanned in portrait orientation (Fig. 3.3), which is more sensitive to changes in OD as a function of dose [Lynch et al., 2006; Andrés et al., 2010]. Films were scanned in the same order in which they were exposed to maintain a consistent development period and minimize any uncertainty due to the continuing polymerization of the film postexposure [Devic et al., 2010]. Neutral density filters with OD of 0.3, 0.5, 0.7, and 1.0 were positioned on the scanbed to monitor the stability of the scanner throughout a scanning session. A plot of the relative transmission measured through each of the filters over sixty consecutive scans is shown in Fig. 3.4. The relative transmission through each filter varies consistently with a peak-to-peak variation of less than 0.5 % and no evidence of a trend. After all films were scanned, a final scan of two stacked, saturated radiographic films was taken for a measurement of the background scanner signal.

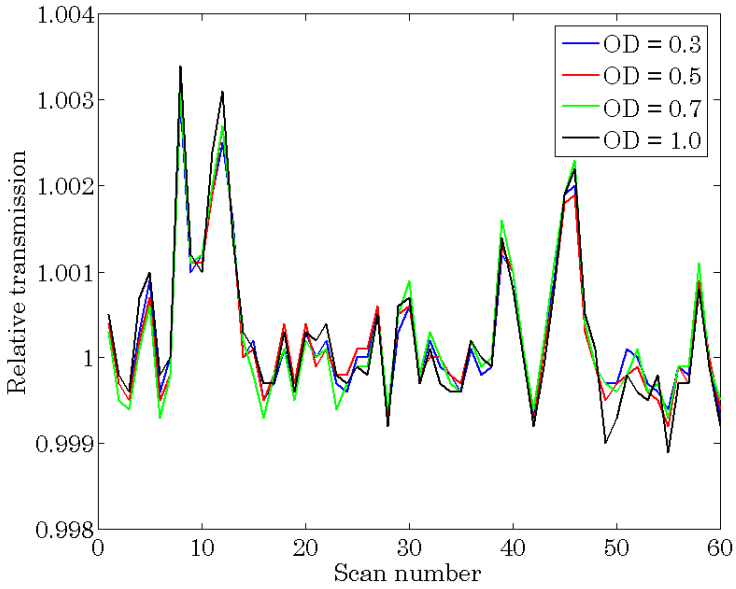

Figure 3.4: Transmission measured through neutral density filters with OD of 0.3, 0.5, 0.7, and 1.0 over sixty consecutive scans. The plotted values are normalized to the median transmission.

3.1.4 Flatbed scanner characterization

The 10000XL flatbed scanner was characterized for use in the analysis of radiochromic film. In particular, the performance of the scanner over repeated scans of the same film and the uniformity of the scanner signal over the surface of the scanbed were investigated.

3.1.4.1 Repeated film scanning

An investigation of the constancy of the measured transmission through a single piece of film over repeated scans was motivated by inconsistent results in the literature. The 10000XL flatbed scanner has an ultraviolet lamp which, it has been hypothesized, could cause a nonnegligible degree of polymerization of the film with successive scans or could warm the film and impact the measured OD. For instance, using an EPSON® Expression® Pro 1680 flatbed document scanner, Lynch et al. [2006] observed increases of 0.09 % to 0.5 % in the OD of EBT films per degree Celsius increase in the temperature of the scanbed. The EBT

films were exposed to doses ranging from 27.1 cGy to 361 cGy, with the greater variations occurring for the films exposed to lower doses. Also using a Pro 1680 flatbed scanner, Paelinck et al. [2007] observed increases of up to 3.5 % in the OD of EBT films exposed to doses ranging from 0 cGy to 396 cGy over 105 consecutive scans. The increase in OD was attributed to development of the film due to exposure to the ultraviolet lamp. However, after an initial five warmup scans using a 10000XL scanner, Ferreira et al. [2009] did not observe any variation greater than 0.15 % in the measured transmission through EBT films exposed to doses ranging from 0.5 cGy to 3.0 cGy over twenty consecutive scans. Similarly, using a 10000XL scanner with EBT2 films exposed to doses ranging from 0 cGy to 300 cGy, Richley et al. [2010] did not observe any trend in measured transmission over 50 consecutive scans, with a maximum variation of 0.8 %.

To investigate the variation in measured transmission through EBT2 film scanned repeatedly with the 10000XL scanner, sheets of film were exposed to doses ranging from 0 Gy to 3 Gy using the University of Wisconsin Accredited Dosimetry Calibration Laboratory (UWADCL) Theratron 1000 ^{60}Co irradiator (Theratronics, Ontario, Canada). The films were exposed to a 10×10 cm^2 field at a source-to-film distance of 100 cm. The scanner was warmed up according to the procedure in Sec. 3.1.3. The film was centered within the scanbed and scanned twenty times consecutively. The mean pixel value within the central 1×1 cm^2 region of the images in the red, green, and blue channels was determined for each scan. The results for a film exposed to 2 Gy are shown in Fig. 3.5. For the film shown, twenty consecutive scans were taken on two consecutive days, denoted trial 1 and trial 2, to test the reproducibility of the results and to test for permanent changes in the film. The data in the red and green channels undergo maximum variations of ± 0.4 % without any apparent trend. However, the data in the blue channel increases by approximately 3 % over the course of the twenty scans, following a continuously increasing trend. There is no evidence of a permanent change in the film, though, as the measured transmission values for

the initial scans on each day are consistent within 0.04 %. To test for a correlation between the trend in the blue-channel signal and film temperature, a thermocouple was affixed to the scanbed to monitor the temperature. Over a series of 35 consecutive scans, the scanbed temperature increased between 1 °C and 1.5 °C. Based on the results of Lynch et al. [2006], no significant change in the measured transmission would be expected for a temperature change of 1 °C to 1.5 °C in a film exposed to 2 Gy, and this conclusion is consistent with the measurements in the red and green channels. Therefore, these results could be an indication that the measured transmission in the blue channel is more sensitive to changes in the film temperature.

3.1.4.2 Scanner uniformity

The signal across the surface of flatbed document scanners has been shown to be nonuniform, depending both on the position on the scanbed and the OD of the film, with greatest variation along the dimension orthogonal to the axis of translation of the scan lamp [Lynch et al., 2006; Devic et al., 2006; Paelinck et al., 2007; Menegotti et al., 2008; Saur and Frengen, 2008; Ferreira et al., 2009]. Thus, to properly characterize the uniformity of the scanner signal, uniformly exposed films of varying OD are required. Given the challenge of uniformly exposing a 20.3×25.4 cm^2 film sheet, many investigators instead have uniformly exposed smaller film pieces and scanned them repeatedly across the surface of the scanbed [Paelinck et al., 2007; Saur and Frengen, 2008; McCabe et al., 2011]. However, as shown in Fig. 3.5, the signal in the blue channel undergoes an increasing trend over repeated scans. Thus, using a single, smaller piece of film, it would not be possible to distinguish variations in the uniformity of the scanner response from the trend in the measured transmission through the film.

This thesis work utilized a technique similar to that of Lynch et al. [2006], which used a 20.3×25.4 cm^2 EBT film exposed to sunlight to achieve the exposure uniformity necessary

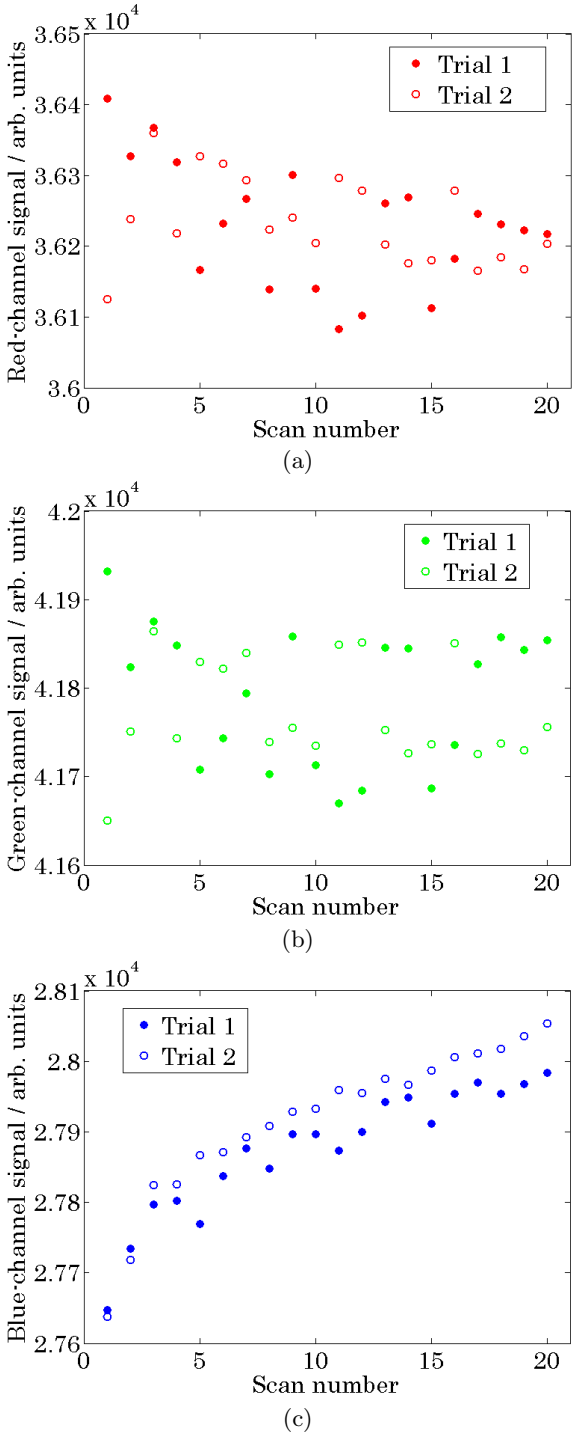

Figure 3.5: Comparison of the variation in the (a) red-, (b) green-, and (c) blue-channel signals over 20 consecutive scans of a piece of EBT2 film exposed to a dose of 2 Gy. The two trials were performed for the same sheet of film on consecutive days.

to characterize the uniformity of the scanner signal. A single sheet of EBT2 film was taped to a 5 cm-thick slab of polymethyl methacrylate (PMMA) and exposed to sunlight for intervals of 1 h to 2 h. After each exposure interval, the film was centered on the scanbed and allowed to thermally equilibrate for 15 min. A single scan was taken, and the film was placed back in the sunlight for the next exposure interval. After a cumulative exposure time of 15 h, the OD of the film exceeded that of a film exposed to 2 Gy. From the red- and blue-channel data of each image, a profile through the center of the film orthogonal to the axis of translation of the scan lamp was extracted. A second-order polynomial was fit to each profile to model the nonuniformity of the scanner signal as a function of both position and OD. For the entire set of polynomials, the maximum peak-to-peak variation over the central 14 cm span of the scanner was less than 0.6 %. This is less than the peak-to-peak variation in the transmission measured over consecutive scans of the same film, indicating that the magnitude of the correction for scanner uniformity is less than the noise of the scanner. Therefore, no corrections were applied for the nonuniformity in the scanner signal.

3.1.5 Film calibration and analysis

The response of EBT2 film was calibrated separately for each linear accelerator used. For each calibration, a total of 66 3×3 cm^2 pieces were cut from three film sheets. Sets of six calibration films were exposed to nominal doses of 0, 20.0, 30.0, 45.0, 67.5, 101, 152, 228, 342, 513, and 769 cGy, with minor deviations due to the inability to deliver partial MU. Each set of six calibration films was comprised of two pieces from each original film sheet to minimize the uncertainty due to interfilm nonuniformity. Films were exposed between two $30 \times 30 \times 5$ cm^3 slabs of Virtual Water™ (Med-Cal, Inc., Verona, WI) at a source-to-film distance of 100 cm. The field size was 10×10 cm^2 at the position of the films. The films were positioned such that the 50 μm polyester layer faced the source. The dose rate at the depth of the calibration films was measured using an Exradin A12 ionization chamber and

a Max 4000 electrometer (Standard Imaging, Inc., Middleton, WI). The dose delivered by a given number of MU was determined using the following equation:

$$D = k_Q N_{D,w}^{^{60}\mathrm{Co}} M_{\mathrm{raw}} P_{\mathrm{TP}} P_{\mathrm{ion}} P_{\mathrm{pol}} P_{\mathrm{elec}}, \tag{3.1}$$

where M_{raw} is the charge measured with the ionization chamber, $N_{D,w}^{^{60}\mathrm{Co}}$ is the calibration coefficient for the ionization chamber obtained from the UWADCL, P_{elec} is the calibration coefficient for the electrometer obtained from the UWADCL, and the beam-quality correction factor (k_Q), temperature-pressure correction (P_{TP}), ion recombination correction (P_{ion}), and polarity correction (P_{pol}) were determined according to the recommendations of AAPM Task Group 51 [Almond et al., 1999].

The calibration films were exposed individually. All of the films originating from a given sheet were exposed in order of increasing dose before progressing to films from the next sheet. The films were scanned individually, before and after exposure, in the order in which they were exposed to establish a consistent postexposure development period for each film. The exposure of six film pieces per dose from three separate film sheets reduces the uncertainty due to intrafilm and interfilm nonuniformity. Additionally, since each film is scanned only once, the scanning of six films per dose in a staggered sequence reduces the uncertainty due to stability of the scanner.

The film response to a given dose was quantified by the net OD, which is defined as:

$$net\,OD = OD_{\mathrm{exp}} - OD_{\mathrm{unexp}} - \Delta OD_{\mathrm{control}}$$

$$= \log_{10}\left(\frac{PV_{\mathrm{unexp}} - PV_{0,\mathrm{unexp}}}{PV_{\mathrm{exp}} - PV_{0,\mathrm{exp}}}\right) - \log_{10}\left(\frac{PV_{\mathrm{unexp,control}} - PV_{0,\mathrm{unexp}}}{PV_{\mathrm{exp,control}} - PV_{0,\mathrm{exp}}}\right), \tag{3.2}$$

where OD_{exp} and OD_{unexp} are the OD of the exposed and unexposed films, respectively, and $\Delta OD_{\mathrm{control}}$ is the change in the OD of the control film. These quantities are determined us-

ing the measured pixel value of the unexposed film (PV_{unexp}), exposed film (PV_{exp}), control film before ($PV_{\text{unexp,control}}$) and after ($PV_{\text{exp,control}}$) exposure, and background scanner signal measured after scanning the unexposed ($PV_{0,\text{unexp}}$) and exposed ($PV_{0,\text{exp}}$) films. Within a dose range of 0 Gy to 4 Gy, the red channel is most sensitive to changes in the OD of the film [Richley et al., 2010]. Therefore, the quantities in Eq. 3.2 were determined by extraction and analysis of the images in the red channel. Alternative film analysis methods have been proposed that use the data in two or all three color channels [Micke et al., 2011]. The motivation of these methods is to account for variations in the thickness of the active layer of the film. According to the Beer-Lambert law, the measured OD at any point on the film is inversely proportional to the thickness of the active layer at that point. The yellow marker dye in the active layer creates a large absorption peak within the blue range of the visible spectrum, providing a sensitive measurement in the blue channel of the film thickness that is minimally dependent on dose. It is then possible to separate contributions to the signal in the red channel from the dose to the film and variations in the film thickness. However, it was shown in Sec. 3.1.4.1 that the signal in the blue channel trends over repeated scans. Therefore, these multichannel analysis methods were not used.

Film images were analyzed using scripts that were written with MATLAB® (MathWorks, Natick, MA). The mean net OD within the central 1×1 cm^2 region of each calibration film was determined. No significant change was observed in the OD of the control films, so the $\Delta OD_{\text{control}}$ term from Eq. 3.2 was set to zero. For each calibration dose, the mean net OD of the six films was determined. A fit was then applied to the delivered dose (D) as a function of the net OD as follows:

$$D = a \cdot net\,OD + b \cdot net\,OD^{2.5}, \tag{3.3}$$

where a and b are parameters of the fit [Devic et al., 2004, 2005]. A representative calibration curve is shown in Fig. 3.6.

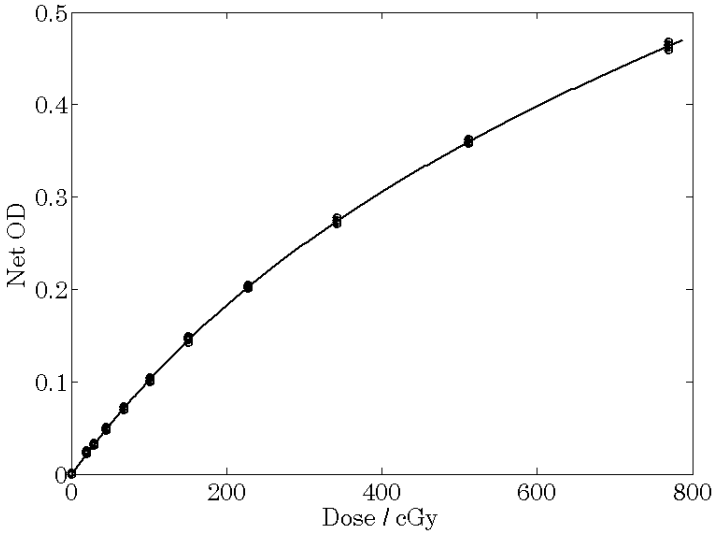

Figure 3.6: Representative calibration curve for EBT2 film dose response.

3.2 TLD dosimetry methods

3.2.1 Thermoluminescent dosimeters

Thermoluminescent dosimeters (TLDs) are a type of solid-state dosimeter. When irradiated, electron-hole pairs are created that migrate through the crystal lattice structure of the TLD. Some of the electron-hole pairs become trapped in potential wells created by impurities within the crystal lattice structure. The charge carriers are liberated when the TLD is heated, and when they recombine, light is emitted. There are wells of varying potential-energy differences within the lattice structure, requiring a range of thermal energies to liberate the trapped charge carriers. During readout, the TLD is heated and the emitted light is recorded; a plot of the luminescent output versus time, called a glow curve, is created. There are characteristic peaks within the glow curve associated with the different potential-energy wells. The total light emitted when the TLD is heated provides a measure of the dose absorbed by the dosimeter.

Thermal recombination of trapped charge carriers results in fading of the TLD signal over time following an exposure. The various peaks in the glow curve each have a recombination

half life, ranging from minutes to years. Due to this change in signal over time, consistency in the handling procedure is necessary to minimize uncertainty.

3.2.2 TLD handling procedure

In this work, $1 \times 1 \times 1$ mm^3 Harshaw TLD-100 LiF:Mg,Ti microcubes (Thermo Electron Corporation, Oakwood Village, OH) were used. The microcubes were stored within a tray with an array of numbered wells for distinction. The dosimeters were transferred between trays using vacuum tweezers to minimize damage.

The potential wells within the TLD can migrate through the lattice structure, impacting the sensitivity to radiation. Annealing the TLDs redistributes the wells throughout the lattice structure, improving the reproducibility of measurements [Attix, 1986]. In this work, the annealing procedure of Cameron et al. [1964] was followed prior to each measurement. The microcubes were first annealed in an aluminum tray at 400 °C for 1 h to reset the distribution of potential wells. After cooling on a room-temperature aluminum slab for 30 min, the microcubes were then annealed at 80 °C for 24 h. This second anneal eliminates the potential wells with a moderately short half life which can substantially impact the quality of measurements. The anneal procedure concluded by again cooling the TLDs on a room-temperature aluminum slab for 30 min. The microcubes were then stored for a minimum of 24 h prior to exposure.

Following exposure of the microcubes, a delay of at least 24 h was allowed for the shortest-lived potential wells to decay. The TLDs were read using a Harshaw 5500 TLD automatic reader. During read-out, each TLD was preheated to 100 °C prior to the collection of luminescent output. The collection of luminescent output was then initiated as the TLDs were heated to 350 °C at a rate of 25 °C/s, and held at that temperature for a total acquisition time of $16\frac{2}{3}$ s. da Rosa et al. [1999] demonstrated that the reproducibility of measurements with microcubes is strongly dependent on the consistency of the dosimeter orientation during

read out. Therefore, after the completion of the first read of the microcubes, they were marked to ensure a consistent orientation during future reads.

The TLDs used in this work were sorted from an initial batch of 301 dosimeters. TLDs were sorted based on the reproducibility of individual dose sensitivity relative to that of the entire batch, known as the chip factor. The chip factor, CF_i, of a given TLD is defined as

$$CF_i = \frac{R_{i,\text{raw}}}{R_{\text{median}}}, \tag{3.4}$$

where $R_{i,\text{raw}}$ and R_{median} are the uncorrected thermoluminescence measured by the TLD and the median uncorrected thermoluminescence measured by the batch of TLDs, respectively, after exposure to a uniform dose. The sorting procedure for the TLDs consisted of three measurements of chip factors. For each chip factor measurement, TLDs were placed in a PMMA holder with a 7.7×7.7 cm^2 array of wells. The TLDs were irradiated to an exposure of 4000 mR at a source-to-detector distance of 2 m using a G10 ^{137}Cs irradiator (Hopewell Designs, Inc., Alpharetta, GA). After three measurements of chip factors, TLDs with a standard deviation in chip factor greater than 1.5 % were excluded from future use.

3.2.3 TLD calibration and analysis

A separate calibration of the TLD response was completed for each measurement using the UWADCL ^{60}Co irradiator. Measurements of TLD chip factors were completed before and after each measurement. Six sets of five calibration TLDs were exposed to doses of 4.99, 89.7, 185, 250, 300, and 350 cGy. A lead attenuator was positioned in the beam for the 4.99 cGy exposure to reduce the dose rate, thereby extending the exposure time and minimizing the uncertainty from shutter timer error. An additional eight TLDs were left unexposed for a measurement of background exposure. The TLDs were exposed in-air within PMMA holders at a source-to-detector distance of 100 cm. The field size was 10×10 cm^2 at the

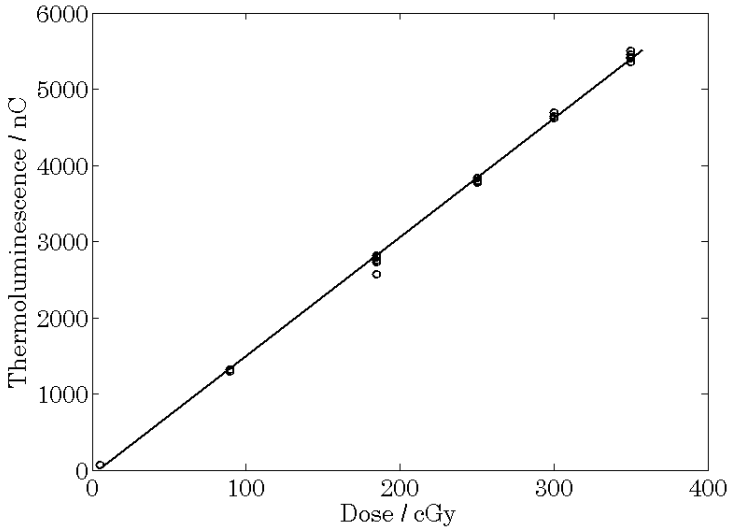

Figure 3.7: Representative calibration curve for TLD dose response.

position of the TLDs. The dose-to-water in the TLD calibration geometry was determined using a Monte Carlo-generated conversion of the UWADCL ^{60}Co air-kerma standard.

The measured thermoluminescence of the i^{th} TLD, $R_{i,\text{raw}}$, was corrected as follows:

$$R_i = \frac{R_{i,\text{raw}}}{\overline{CF_i}} - R_{\text{bkgd}}, \tag{3.5}$$

where R_i is the fully corrected thermoluminescence, $\overline{CF_i}$ is the mean of the chip factors measured before and after the exposure, and R_{bkgd} is the mean thermoluminescence measured from the background TLDs corrected for individual TLD sensitivity. For each calibration dose, the mean thermoluminescence of the five TLDs was determined. A linear fit was then applied to the dose to water as a function of thermoluminescence. A representative calibration curve is shown in Fig. 3.7. For one of the calibration TLDs exposed to 185 cGy, the measured thermoluminescence differed from that for other TLDs exposed to the same dose by 10 %. Although TLDs were sorted based on a standard deviation in response of less than 1.5 %, a larger variation in the response of the TLDs is possible. This increased variation in response is accounted for in the uncertainty of the TLD calibration (Sec. 4.4.2.6).

Chapter 4

Development and characterization of a radiochromic film stack dosimeter

4.1 Three-dimensional dosimetry

Three-dimensional dosimeters are valuable tools for verifying the commissioning of treatment planning and delivery systems. The most extensively investigated 3D dosimeters are gel dosimeters, namely Fricke gels and polymer gels. The use of Fricke gel dosimeters, which incorporate ferrous ion (Fricke) solution into a gelatin matrix [Gore et al., 1984], has been demonstrated in several studies [Appleby et al., 1987; Olsson et al., 1989; Hazle et al., 1991]. However, the accuracy of dose distribution measurements with Fricke gel is limited by diffusion of the ferric ions within the gel [Olsson et al., 1990; Schulz et al., 1990; Pedersen et al., 1997]. The diffusion rate of the ferric ions can be reduced with the incorporation of a chelator, such as xylenol orange, into the gel, but the sensitivity of the dosimeter is consequently reduced [Rae et al., 1996]. Furthermore, Fricke gel dosimeters are

subject to spontaneous thermal oxidation, thereby requiring that the dosimeters be stored in a temperature-controlled environment for a consistent duration between preparation and exposure [Rae et al., 1996].

Polymer gel dosimeters are comprised of acrylic monomers, which undergo polymerization and cross-linking reactions when exposed to radiation. The polymers increase the NMR relaxation rates of nearby water protons, permitting readout with MRI. Polymer gels have been shown to be more sensitive and spatially stable than Fricke gels [Maryanski et al., 1993, 1994]; however, when read using MRI, polymer gel measurements are dependent on the temperature during preparation, storage, and scanning [De Deene et al., 1998, 2000, 2007]. Because the polymer is insoluble in water, it is visible, permitting dose measurement by means of optical CT [Gore et al., 1996]. Polymer gel measurements read using optical CT have a higher signal-to-noise ratio than those read using MRI [Oldham et al., 2001], but are subject to substantial light scattering artifacts [Xu et al., 2003; Oldham and Kim, 2004]. Optical CT scans are also subject to large edge artifacts, due to imperfect matching of the indices of refraction of the gel, encasement, and fluid bath, thereby limiting the useful measurement volume [Kelly et al., 1998; Doran et al., 2001; Xu et al., 2004].

The most recent development in 3D dosimetry is the PRESAGE™ dosimeter, which is comprised of a solid polyurethane matrix doped with radiochromic leuco dyes [Guo et al., 2006b]. Because PRESAGE™ is a solid plastic material, there is no need for a container, thereby removing one material interface and potentially reducing edge artifacts when read with optical CT. Additionally, the exposed leuco dyes are optically absorptive, greatly reducing the occurrence of scatter artifacts. High spatial resolution has been achieved with PRESAGE™ measurements [Doran et al., 2010], and good agreement between PRESAGE™ and radiochromic film measurements, as well as calculated dose distributions, has been demonstrated [Oldham et al., 2008; Sakhalkar et al., 2009a,b; Thomas et al., 2011, 2013]. The PRESAGE™ dosimeter is sensitive to fluorescent light [Guo et al., 2006a], however,

and its response has an exponential dependence on the temperature during irradiation and storage [Skyt et al., 2011]. Furthermore, a partial uncertainty analysis from dose measurements of a high-dose-rate brachytherapy source reported substantially higher uncertainty for PRESAGE™ measurements as compared with radiochromic film [Palmer et al., 2013]. Currently, a comprehensive uncertainty analysis of PRESAGE™ measurements is not available in the literature.

To summarize the current state of 3D dosimetry, extensive experience is required not only in radiation physics, but also in polymer chemistry and quantitative imaging [Baldock et al., 2010].

4.2 Film stack dosimetry

As discussed in Sec. 3.1.1, radiochromic films are self-developing, high-resolution, nearly tissue-equivalent dosimeters with limited energy and dose-rate dependence [Niroomand-Rad et al., 1998]. Therefore, a 3D dosimeter comprised of a stack of radiochromic films offers the advantages of existing 3D dosimeters without the need for dedicated facilities to fabricate and analyze the dosimeters.

Although radiochromic films have been used as reference dosimeters to evaluate 3D dosimeters [Guo et al., 2006a; Oldham et al., 2008; Sakhalkar et al., 2009a; Palmer et al., 2013], there are few examples of the use of radiochromic films for 3D dosimetry. Initial applications of radiochromic-film-stack dosimetry used the average response of stacked films to improve the sensitivity of planar dose measurements [Cheung et al., 2001; Butson et al., 2001; Cheung et al., 2002]. Stacks of the insensitive film dosimeters were later used to make high-resolution, 3D measurements of the high-gradient dose distribution near high-dose-rate brachytherapy sources [Mourtada et al., 2003; Chiu-Tsao et al., 2004]. With the development of more sensitive EBT films, 3D measurements of external beam dose distributions became feasible. Chiu-Tsao and Chan [2009] used a stack of EBT films to measure the

dose in the buildup region of 6 MV and 15 MV photon beams. Most recently, Kim et al. [2012] used a stack of EBT2 films spaced 5 mm apart to measure the 3D dose distributions of clinical proton beams. However, film stacks have not been fully characterized as 3D dosimeters. In this chapter, the development and characterization of a radiochromic film stack dosimeter for use in megavoltage photon beam dosimetry is discussed. In particular the energy dependence, orientation dependence, and water equivalence of the film stack dosimeter are investigated. Measurements with the film stack dosimeter are compared with TLD measurements and Monte Carlo simulations. Finally, the film stack dosimeter is used to verify the delivery of an IMRT treatment plan.

4.3 Development of the radiochromic film stack dosimeter

4.3.1 Film stack dosimeter phantom housing

Spatial registration of individual films within the film stack dosimeter is paramount for accurate 3D dosimetry. A phantom housing for the film stack dosimeter was designed and fabricated to maintain alignment of the individual films. As will be discussed in Ch. 6, the film stack dosimeter phantom housing was used as the CTV in the preparation of IMRT and SBRT lung plans. Therefore, the phantom housing must be representative of the size of a lung tumor to generate realistic treatment plans. Eligibility for SBRT protocols is typically limited to patients with tumors no larger than 5 cm in diameter [Timmerman et al., 2010], but the use of SBRT for lung tumors with a diameter of up to 7 cm has been demonstrated [Fakiris et al., 2009].

The film stack dosimeter phantom housing was designed as a spherical volume with a cylindrical cavity to house the film stack dosimeter. The dimensions of the phantom were chosen to maximize the volume of film within the dosimeter while maintaining a minimum phantom thickness of 5 mm. The phantom design optimization is illustrated in Fig. 4.1,

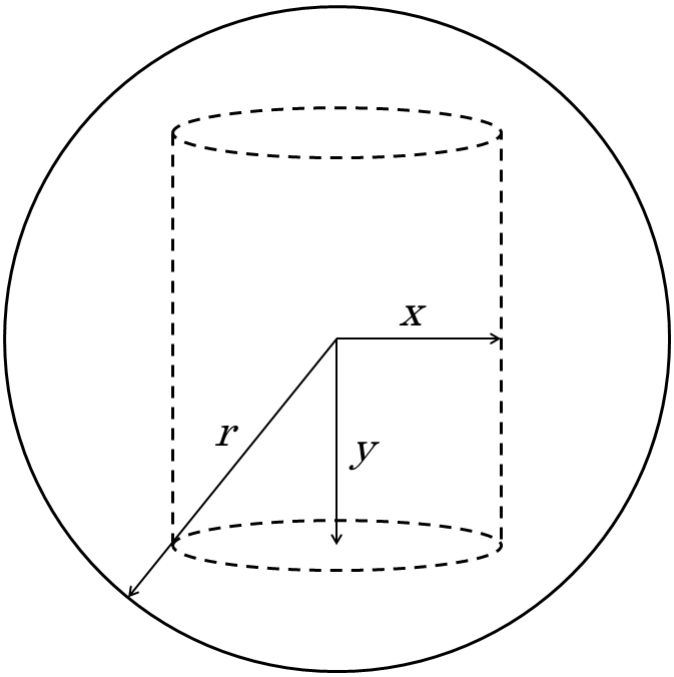

Figure 4.1: Schematic illustrating the optimization of the design of the film stack dosimeter phantom housing. For a given phantom radius r, the optimal film stack dosimeter dimensions (radius x and height $2y$) were determined by maximizing the quantity $2\pi x^2 y$ subject to the constraint $r - \sqrt{x^2 + y^2} = 0.5\,\text{cm}$.

where x is the radius of the central cavity, $2y$ is the height of the central cavity, and r is the radius of the phantom housing. The results of the optimization are shown in Table 4.1. A film stack dosimeter with a diameter of 3.84 cm and a height of 2.72 cm was developed, resulting in a phantom housing with a diameter of 5.7 cm. A tumor volume with a diameter of 5.7 cm is categorized as stage T2b/IIA; for reference, a tumor volume with a diameter of 3 cm to 5 cm is classified as stage T2a/IB [Goldstraw et al., 2007].

The film stack dosimeter phantom housing, shown in Fig. 4.2, was fabricated from Virtual Water™ (Med-Cal, Inc., Verona, WI). The spherical phantom was truncated above and below the film stack dosimeter for ease of positioning. The central cavity that maintains the alignment of the films was machined with a tolerance of ± 0.01 cm. Scribe marks on the outer surface of the phantom facilitate alignment with positioning lasers.

Table 4.1: Results of the film stack dosimeter phantom housing design optimization. For a given phantom radius r, the film stack radius x and height $2y$ maximize the film volume for a minimum phantom thickness of 5 mm.

r (cm)	2.50	2.75	2.85	3.00
x (cm)	1.63	1.84	1.92	2.04
y (cm)	1.15	1.30	1.36	1.44

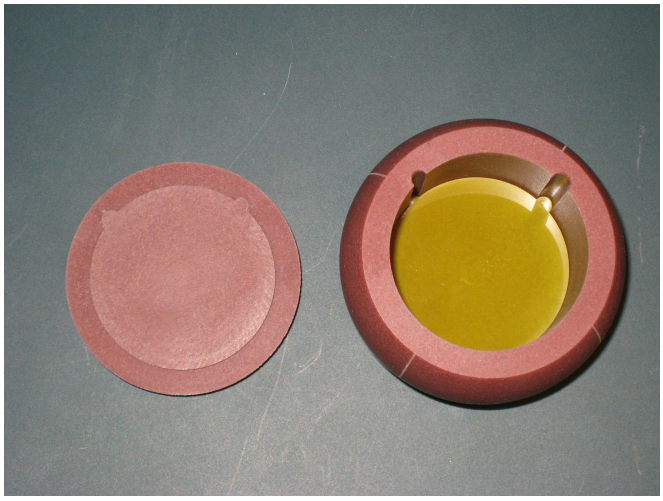

Figure 4.2: The film stack dosimeter phantom, which maintains the radial alignment of the films.

4.3.2 Film stack dosimeter

The films for the film stack dosimeter were laser-cut (Laserage Technology Corporation®, Waukegan, IL) with a tolerance of ± 0.008 cm to minimize positioning uncertainty. Given the tolerance in the fabrication of the phantom housing (± 0.01 cm) and in the cutting of the film (± 0.008 cm), the ideal film dimensions were determined by trial-and-error with sample cuts of incrementally larger films. The selected radius for the film stack dosimeter leaves a nominal radial gap of 0.008 cm between the films and the phantom housing. Based on the difference in the nominal radii of the film stack dosimeter and the phantom housing cavity, the radial positioning uncertainty of the film stack dosimeter is 0.01 ± 0.01 cm. Each film has two semicircular tabs centered on the outer diameter and separated by a 90° arc to fix the azimuthal orientation of the film stack dosimeter within the phantom housing. The two tabs have differing radii of 0.150 cm and 0.187 cm to uniquely define the top face of each film.

Films were shipped to Laserage Technology Corporation® to be cut. Each film was marked with a label on the 50 μm-thick polyester layer to ensure that all films were cut with this side up. The films were shipped in their original packaging, sealed within an opaque envelope with interleaved sheets of tissue paper. Unexposed control film pieces were also included in the shipment to Laserage Technology Corporation® to verify that films were not exposed during shipment. None of the control films exhibited a significant change in OD, indicating that the films were not exposed during shipment. For the return shipment of the cut films, the film pieces were individually packaged in plastic bags to prevent surface abrasions. To ensure that the films were properly handled during cutting, a list of handling instructions, shown in Table 4.2, was included with the shipment of films.

Once the films were received from Laserage Technology Corporation®, an initial loading of the film stack dosimeter phantom housing was completed. Individual films were loaded into the phantom housing using vacuum tweezers. Approximately 75 films were required to

Table 4.2: Instructions for handling radiochromic film that were included with the shipment of films to Laserage Technology Corporation®.

Radiochromic film handling instructions
1. Do not remove control film pieces from the box
2. Wear latex gloves when handling the film
3. Do not slide the film across surfaces or other films
4. Do not fold the film
5. Minimize exposure of the film to artificial light
6. Store the film below 25°C (77°F)
7. When cutting the film, align the film such that the label is face up and in the bottom right corner
8. Return all film pieces, including any scrap
9. Attach enclosed “Film Do Not X-Ray” labels to the exterior of the package for the return shipment

completely fill the cavity within the phantom housing. Given a cavity depth of 2.72 cm and a nominal film thickness of 285 μm, and assuming that the spacing between films is uniform, a stack of 75 films indicates a separation of 0.1 mm between films. Additionally, the top film of the stack was visibly nonparallel with the top plane of the phantom housing. The thicknesses in the center and at eight equally spaced points around the edges of five films were measured using a micrometer. The films had a thickness of 285 $\pm$ 2 μm in the center, but a thickness of 404 $\pm$ 22 μm around the edges. The laser cutting created a substantial burr of inconsistent thickness around the edges of the films, resulting in relatively large, nonuniform spaces between films. The impact of these burrs was mitigated by interleaving spacers between the films. The spacers, shown in Fig. 4.3, were laser-cut to the same dimensions as the films from sheets of Virtual Water™ that were nominally 1 mm thick. The thickness was measured at an annular array of seventeen positions over the surface of each spacer. Only spacers with a peak-to-peak variation in thickness of less than 8 μm were used. The set of spacers that were accepted for use had a mean thickness of 973 $\pm$ 6 μm. The edges of each spacer were lightly filed to prevent contact with the burrs, thereby eliminating the impact of the burrs on film spacing. The resulting film stack dosimeter is comprised of 22 films and 21 spacers. Taking the difference between the depth of the cavity in the phantom housing and the measured thickness of the film stack dosimeter under compression, the films and spacers are separated by gaps of 15 μm if uniform spacing is assumed.

4.3.3 Additional phantom housings

To facilitate the characterization of the film stack dosimeter, two additional Virtual Water™ phantoms were developed. The TLD phantom, shown in Fig. 4.4, has the same outer dimensions as the film stack dosimeter phantom. However, the TLD phantom has a layered insert that holds 125 TLD-100 microcubes distributed across five planes. The cylindrical phantom housing, shown in Fig. 4.5, is a cylindrical phantom with a 10 cm diameter and a

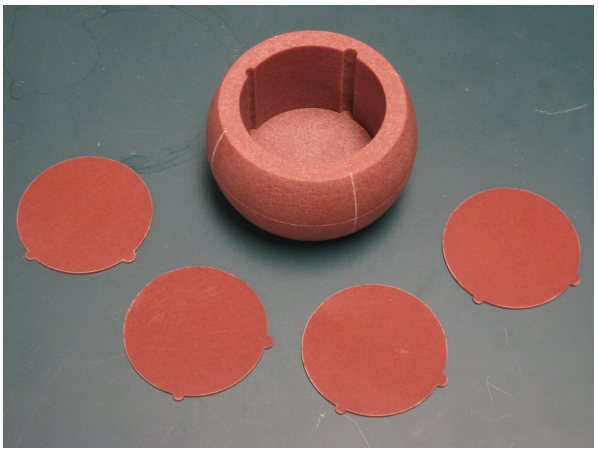

Figure 4.3: Film stack dosimeter phantom housing shown with the spacers that were interleaved between films within the film stack dosimeter.

12 cm extent. The cylindrical phantom housing has a central cavity that interchangeably accommodates both the film stack dosimeter phantom housing and the TLD phantom, thereby reducing positioning uncertainty.

4.4 Characterization of the radiochromic film stack dosimeter

4.4.1 Methods and materials

4.4.1.1 Monte Carlo radiation transport

Monte Carlo simulations were used to investigate the energy dependence, orientation dependence, and water equivalence of the film stack dosimeter. Monte Carlo simulations use random sampling of probability distributions to determine statistically expected outcomes of a given experiment. For instance, Monte Carlo radiation transport codes simulate the interactions of radiation with matter. The assumption is made that the interactions of any given particle are independent of those of other particles; therefore, each particle is transported individually. Interaction cross sections specific to the particle type and energy and

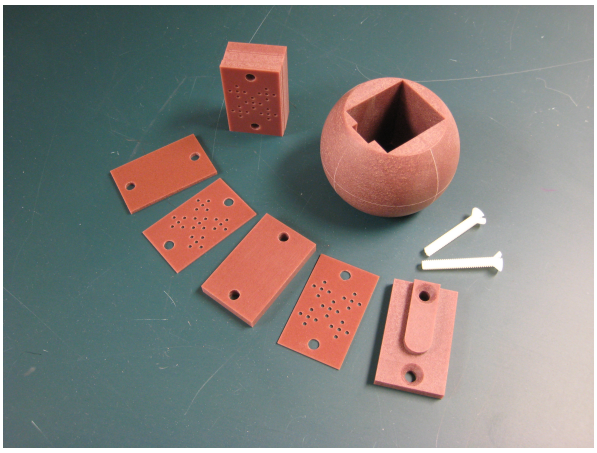

Figure 4.4: The TLD phantom, which has the same outer dimensions as the film stack dosimeter phantom housing, but has a layered central insert that holds 125 TLD-100 microcubes distributed across five planes.

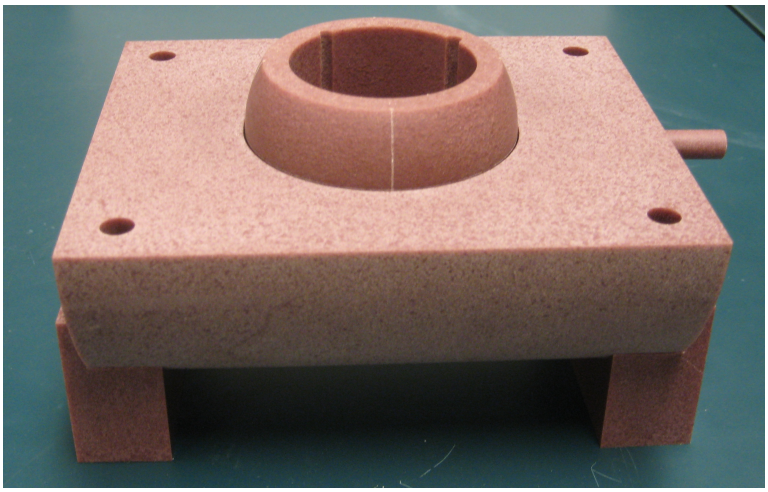

Figure 4.5: The cylindrical phantom housing, which has a central cavity that accommodates both the film stack dosimeter phantom housing and the TLD phantom interchangeably.

the medium in which the transport occurs are sampled to determine the types and locations of interactions and the resulting transfer of energy, change in trajectory, and creation of new particles. Photons undergo relatively few interactions, so each event is explicitly simulated. Electrons, however, undergo continuous Coulombic (i.e., soft) interactions in addition to discrete hard collisions, making event-by-event transport prohibitively expensive. The majority of electron interactions result in only small changes in energy and/or direction. Therefore, electron transport employs a condensed-history technique in which large numbers of interactions are condensed into single steps, after which changes in energy, direction, and position are sampled from multiple-scattering distributions [Berger, 1963]. The use of the condensed-history technique introduces the artificial parameter electron step length, which can impact the simulated results [Bielajew and Rogers, 1988].

For the characterization of the film stack dosimeter, Monte Carlo N-Particle v5.1.60 (MCNP5) radiation transport code (Los Alamos National Laboratory, Los Alamos, NM) was used. This code was chosen for its superior flexibility in modeling experimental geometries, which was necessary to accurately model the film stack dosimeter and phantom housing. The model of the film stack dosimeter varied slightly for each investigation, so the simulation geometry is discussed in detail in the sections that follow. Both cell fluence (F4) and energy deposition (*F8) tallies were used in this work. The cell fluence tally determines contributions to the fluence from a given history as the ratio of the track length of the particle through the cell and the volume of the cell [Chilton, 1978]. The energy deposition tally directly tracks the energy deposited within a cell. Taking the ratio of the tally result with the mass of the cell gives the absorbed dose to the cell. The only variance reduction technique that was employed in the MCNP5 simulations was photon collision forcing within the *F8 tally volumes. With forced collisions, each particle that passes through the specified cell is split into a collided part and an uncollided part, weighted by the probability of interaction within or escape from the cell, respectively.

The condensed-history method employed by MCNP5 for electron transport calculates energy losses based on a fixed array of energy bounds, such that the electron energy decreases by an average of 8.3 % per step [Hughes, 2005]. For each electron step, an energy bin is selected based on the electron energy, and the Landau straggling distribution [Landau, 1944] is accordingly sampled to determine the energy loss in that step. MCNP5 has three options for indexing electron energies: a bin-centered method, a nearest-group-boundary method, and an energy- and step-specific method. The bin-centered and nearest-group-boundary methods have been compared in multiple studies, each of which determined the latter is more accurate [Jeraj et al., 1999; Reynaert et al., 2002; Schaart et al., 2002]. However, for both of these indexing methods, unphysical results have been observed when simulating transport through cells with dimensions smaller than the electron step size [Reynaert et al., 2002; Hughes, 2005]. Rather than sample the Landau straggling distribution for an indexed energy, the energy- and step-specific indexing method uses the actual electron energy at the start of a step to sample the distribution. This method has been shown to accurately simulate electron transport through 10 μm-thick scoring regions [Paxton, 2012]. However, the energy- and step-specific method is also highly dependent on the user-defined number of substeps per electron step [Paxton, 2012; Koivunoro et al., 2012]. In the absence of unphysical results, the bin-centered indexing method shows better agreement with other Monte Carlo radiation transport codes than the energy- and step-specific method [Koivunoro et al., 2012].

Two simulations of a modified film stack dosimeter geometry were completed to test for unphysical results with the use of the bin-centered electron-energy-indexing method. As will be discussed in Sec. 4.4.1.3, the film stack dosimeter phantom housing was modeled as a sphere of Virtual Water™ with a diameter of 5.7 cm. The composition of Virtual Water™ was modeled as in Murphy et al. [2004]. The film stack dosimeter was modeled as a stack of 21 films, centered at the origin of the phantom housing, with 20 interleaved spacers. The

individual layers of each film were explicitly modeled according to their nominal thicknesses (Fig. 3.1). A cylindrical tally cell with a diameter of 30 μm and an extent of 1 cm was centered within the active layer of each film. In both simulations, all cells were assigned the Virtual Water™ material. In the second simulation, the cells corresponding to the film layers and spacers were removed, so that only the tally volumes remained within the phantom housing. The energy deposited within the tally cells from a beam normal to the film planes was simulated. No significant difference between the results of the two simulations was observed within a statistical uncertainty of 1 % ($k = 2$), indicating that the transport of electrons through the layers of the film stack dosimeter using the bin-centered electron-energy-indexing method is not subject to unphysical results. Therefore, the bin-centered electron-energy-indexing method was used for the characterization of the film stack dosimeter.

4.4.1.2 Energy dependence

The energy dependence of the response of a detector is nominally comprised of two components: the intrinsic energy dependence and the absorbed-dose energy dependence. The intrinsic energy dependence, $k_{\mathrm{bq}}(Q)$, is given by

$$D_{\mathrm{det}}(Q) = k_{\mathrm{bq}}(Q) M_{\mathrm{det}}(Q), \tag{4.1}$$

where $D_{\mathrm{det}}(Q)$ is the dose to the detector for a beam quality Q, and $M_{\mathrm{det}}(Q)$ is the corresponding detector response. Thus, the intrinsic energy dependence accounts for energy-dependent changes in the detector response for a given dose to the detector. The absorbed-dose energy dependence, $f(Q)$, is given by

$$D_{\mathrm{med}}(Q) = f(Q) D_{\mathrm{det}}(Q), \tag{4.2}$$

where $D_{\mathrm{med}}(Q)$ is the dose to the medium of interest at the point of measurement of the detector in the absence of the detector, and $D_{\mathrm{det}}(Q)$ is the corresponding dose to the detector. Therefore, the absorbed-dose energy dependence accounts for differences in the energy absorbed within the medium of interest and the detector for a given beam quality. The total energy dependence of a detector is the product of the intrinsic energy dependence and the absorbed-dose energy dependence.

Although the response of EBT films is minimally dependent on the energy of incident radiation in the megavoltage energy range, substantial variation in film response as a function of energy has been observed for kilovoltage energies [Richter et al., 2009]. In particular, the absorbed-dose energy dependence of EBT2 film has been shown to be as large as 50 % in the kilovoltage energy range [Sutherland and Rogers, 2010]. Although the peak energy of a 6 MV photon beam is 6 MeV, the bremsstrahlung spectrum consists of a substantial fluence below 1 MeV. Fig. 4.6 shows the simulated in-air bremsstrahlung spectra of 2×2 cm^2, 5×5 cm^2, and 10×10 cm^2 6 MV fields from a Clinac® iX accelerator (Varian Medical Systems, Inc., Palo Alto, CA). Note both the substantial component of fluence below 1 MeV and the difference between the three spectra within this energy range. As discussed in Sec. 3.1.5, the response of EBT2 film was calibrated using a 10×10 cm^2 6 MV field. However, the film stack dosimeter was used to measure the dose distribution of IMRT treatments comprised of MLC segments much smaller in area. Therefore, differences in the energy spectra of the calibration and measurement fields could require a correction for the energy-dependent response of EBT2. More importantly, changes in the energy spectrum throughout the extent of the film stack dosimeter would require a depth-dependent correction.

The energy dependence of the film stack dosimeter was investigated using Monte Carlo simulations. The spectra shown in Fig. 4.6 were each used to define a directional point source, collimated to a circular field with diameter equal to the side of the respective square

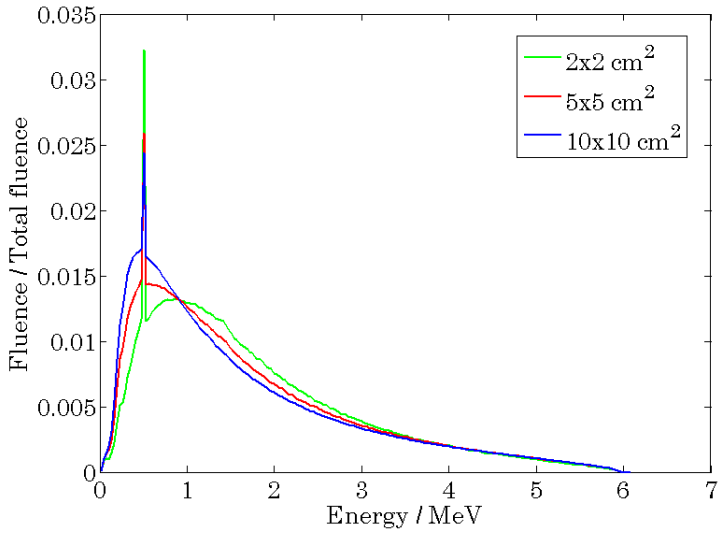

Figure 4.6: Comparison of 6 MV bremsstrahlung spectra for field sizes of 2×2 cm^2, 5×5 cm^2, and 10×10 cm^2. The energy spectra were tallied in-air at the exit of the treatment head of a Monte Carlo model of a Varian Clinac® iX accelerator [Junell, 2013]. Each spectrum was normalized to total fluence.

field, in MCNP5 simulations of the film stack dosimeter geometry. The film stack dosimeter phantom housing was modeled both alone and within the cylindrical phantom housing, centered at a source-to-axis distance (SAD) of 100 cm in both cases, according to the specifications for each. The 22 EBT2 films and 21 spacers of the film stack dosimeter were explicitly modeled within the phantom housing. The 10×10 cm^2 spectrum was also used in a simulation of the film calibration geometry, described in Sec. 3.1.5. The individual layers of EBT2 film were modeled using the nominal thicknesses from Fig. 3.1 and the compositions from Sutherland and Rogers [2010] (EBT2 lot 020609). The composition of Virtual Water™ was obtained from Murphy et al. [2004]. Using energy-binned F4 tallies, the photon fluence spectra through the active layer of the calibration film and the top, middle, and bottom films of the film stack dosimeter were simulated to discern differences between the two geometries and within the film stack dosimeter geometry.

4.4.1.3 Orientation dependence

The response of radiochromic film to ionizing radiation has been shown to vary with the relative orientation of the incident radiation [Suchowerska et al., 2001]. In their investigation, Suchowerska et al. [2001] placed pieces of radiochromic film between two halves of a cylindrical phantom and exposed the films at a series of incidence angles ranging from 0° to 90° between the beam axis and the axis normal to the film plane. The exposures were then repeated with a separate cylindrical phantom which had a central slit just large enough to accommodate the film pieces. Thus, in the first set of exposures, there was a gap between the two halves of the phantom due to the presence of the film, while in the second set of exposures, there was no air gap around the film. It was determined that the film response is minimally dependent on the orientation of the incident radiation, except for cases in which the beam axis and film-normal axis are within $\pm 1°$ of orthogonal, where the film response was found to increase up to 9 %. In the absence of the air gap around the film, the response of the film varied less than ± 1 % over all angles of incidence. Therefore, the observed orientation dependence in the response of radiochromic film can be essentially eliminated by minimizing air gaps around the film.

In this work, the orientation dependence of the film stack dosimeter was investigated using MCNP5 simulations. To verify the use of Monte Carlo simulations to investigate the orientation dependence of radiochromic film, the experiment of Suchowerska et al. [2001] was reproduced in a series of simulations. The results of these simulations compared with those of Suchowerska et al. [2001] are shown in Fig. 4.7. Qualitatively, the simulated results are consistent with those of Suchowerska et al. [2001]. For angles of incidence less than 89°, the simulated orientation dependence does not exceed the statistical uncertainty of ± 2 % ($k = 2$). Likewise, in the absence of air gaps, the simulated orientation dependence does not exceed the statistical uncertainty of ± 2 % ($k = 2$). Both the experimental and simulated results indicate an overresponse when the beam axis and film-normal plane are orthogonal;

however, the simulated overresponse is nearly double the experimental result. This could be the result of multiple discrepancies between the experimental and computational investigations. First, the simulations considered EBT2 film for consistency with this thesis work, whereas Suchowerska et al. [2001] used an older model of Gafchromic® film. The size of both the film used for the exposures and the analyzed region were not specified; the simulations modeled 3×3 cm^2 pieces of film and tallied the energy deposited within the central 1×1 cm^2 region. The use of a smaller film increases the extent of the air gap surrounding the film, which would be expected to increase the observed relative overresponse. Finally, the simulations tallied the energy deposited within the film, while the experimental study considered the variation in the net OD of the film. The net OD of film as a function of dose is sublinear, so a given relative change in net OD corresponds to a greater relative change in dose. Given the qualitative agreement between the measured and simulated results, and the differences in the two studies that are consistent with the observed discrepancies in the results, it was concluded that Monte Carlo simulations can be used to model the orientation dependence of radiochromic film.

A schematic of the geometry used for the orientation dependence simulations is shown in Fig. 4.8. The film stack dosimeter phantom housing was modeled as a sphere with a diameter of 5.70 cm to maintain an orientation-independent phantom geometry. The film stack dosimeter was modeled as a stack of 21 films and 20 spacers with the active layer of the central film centered at a SAD of 100 cm. This modification to the film stack dosimeter geometry was necessary to both tally the dose within an active layer of EBT2 and to maintain a constant tally depth as a function of beam angle. A cylindrical tally volume with a diameter of 30 μm and an extent of 1 cm was centered within the active layer of the central film in the film stack dosimeter. A directional point source was simulated with the 10×10 cm^2 spectrum from Sec. 4.4.1.2. A *F8 tally was used to simulate the energy deposited within the tally volume. Photon collisions were forced within the tally volume. Separate simula-

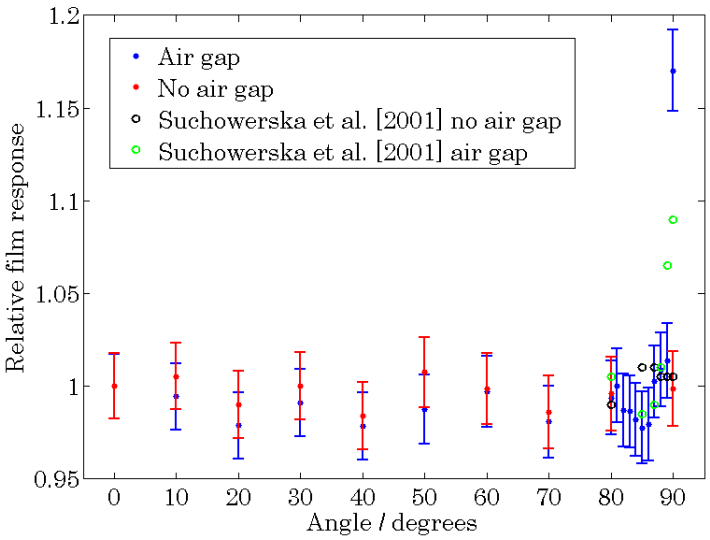

Figure 4.7: Comparison of the measured orientation dependence of radiochromic film from Suchowerska et al. [2001] and the orientation dependence of EBT2 film simulated using MCNP5. The simulated results are shown with statistical uncertainty of $\pm 2\,\%$ ($k = 2$).

tions were completed with the source positioned at a series of angles about the longitudinal axis of the tally volume. Defining ϕ as the angle in the transverse plane of the tally volume between the axis normal to the film planes and the beam axis, separate simulations were completed for $\phi \in \{0°, 10°, 20°, 30°, 40°, 50°, 60°, 70°, 80°, 82°, 84°, 86°, 88°, 90°\}$. For each beam orientation, separate simulations were completed for air gaps of 0 μm, 25 μm, 50 μm, and 100 μm between films and Virtual Water™ spacers. For the 100 μm-air-gap geometry, the film stack dosimeter was modeled as a stack of 19 films and 18 spacers for consistency in the overall height of the film stack dosimeter.

4.4.1.4 Water equivalence

EBT2 film is nearly water equivalent, with an effective atomic number, Z_{eff}, of 6.84, as compared with that of water, $Z_{\text{eff}} = 7.3$ [Arjomandy et al., 2010]. Additionally, the mass-energy-absorption coefficient of the active layer of EBT2 is within 5 % of that for water for energies above approximately 200 keV [Sutherland and Rogers, 2010]. Consequently,

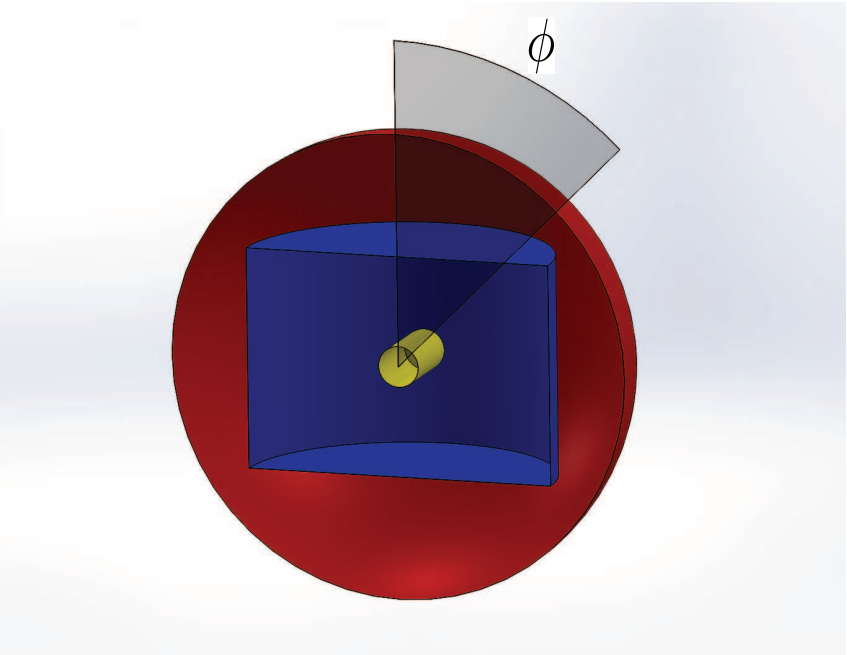

Figure 4.8: Section view through the transverse plane of the orientation dependence simulation geometry. The film stack dosimeter phantom housing, shown in red, was modeled as a sphere. The film stack dosimeter, shown in blue, is depicted as a single cylindrical volume for simplicity; however, the individual films and Virtual Water® spacers were explicitly modeled. The tally volume, shown in yellow, is enlarged for clarity. Separate simulations were completed for several values of ϕ, the angle between the beam axis and the axis normal to the film planes.

the fluence in a volume of water is minimally perturbed by the introduction of a piece of EBT2 film. However, film stack dosimeter measurements replace a greater effective volume of water with film material, in which case the difference in atomic composition may result in a greater perturbation of the fluence, thereby impacting the accuracy of dose-to-water measurements. The water equivalence of the film stack dosimeter was investigated using both measurements and MCNP5 simulations.

The percentage-depth-dose (PDD) profile was simulated in a cylindrical water volume equal in size to the cylindrical phantom housing. The water volume was modeled at a SAD of 100 cm with the beam axis normal to the curved face of the phantom. A directional point source with the 10×10 cm^2 spectrum from Sec. 4.4.1.2 was used. Cylindrical tally volumes were modeled within the water phantom along the beam axis oriented such that the circular faces were normal to the beam axis. The tally volumes had diameters of 1 mm and thicknesses of 0.1 mm, and were spaced at intervals of 0.5 mm near the depth of maximum dose (i.e., 1.5 cm) and 1.5 mm elsewhere. The energy deposited in the tally volumes was simulated using *F8 tallies. Photon collisions were forced within the tally volumes.

The results of MCNP5 tallies are normalized per source particle transported. To convert the simulated PDD profile to dose, a simulation of the reference conditions defined by AAPM Task Group 51 [Almond et al., 1999] using the source from the PDD simulation was completed. A $30 \times 30 \times 30$ cm^3 water volume was modeled at a source-to-surface distance (SSD) of 100 cm. A cylindrical tally volume, 0.61 cm in diameter and 2.36 cm in extent to represent the air cavity within a Farmer-type ionization chamber, was positioned at a depth of 10 cm with the longitudinal axis perpendicular to the beam axis. The energy deposited within the tally volume was simulated using a *F8 tally. Together with a dose measurement in reference conditions, the results of this simulation provided a conversion to dose to water from the normalization per starting particle history for the source used in the PDD simulation.

For comparison with the simulated PDD profile, the film stack dosimeter was used to measure the PDD profile of a 6 MV, 10×10 cm^2 field delivered with a Clinac® iX accelerator. Prior to exposure of the film stack dosimeter, the dose in the reference geometry defined by AAPM Task Group 51 [Almond et al., 1999] was measured using a PTW N30013 Farmer® ionization chamber (Freiburg, Germany) and a Max 4000 electrometer, both calibrated at the UWADCL. Using the results of the measured and simulated dose in reference conditions, a conversion coefficient was generated to convert the simulated dose per starting particle to dose-to-water per MU. Using this conversion coefficient and the results of the PDD simulation, the number of MU required to deliver a dose of approximately 200 cGy to the depth of maximum dose in the cylindrical phantom housing was determined. The film stack dosimeter was positioned in the cylindrical phantom housing at a SAD of 100 cm. Two separate measurements were performed with the film planes of the film stack dosimeter oriented parallel and perpendicular to the beam axis.

4.4.1.5 Comparison with TLD measurements

To verify the accuracy of dose measurements with the film stack dosimeter, a comparison was made with TLD-100 microcube measurements. The dose distribution from a 6 MV, 1.5×10 cm^2 field delivered with a Clinac® iX accelerator was measured using the film stack dosimeter and TLD-100 microcubes loaded into the TLD phantom. Within the TLD phantom, the microcubes are distributed across five planes, with five groups of five microcubes in each plane. Following the microcube sort described in Sec. 3.2.2, TLDs were grouped into 25 sets of five with a maximum difference in mean chip factor of less than 1 %. These sets of TLDs were then divided into five total groups such that the minimum difference in mean chip factor between two sets of five TLDs within a group of 25 TLDs was greater than 3 %. This method of grouping was employed to both minimize the impact of minor displacements of TLDs and facilitate the identification of major displacements. For instance, if two TLDs

within a group of five were mistakenly exchanged, the resulting error would be less than 1 % if both receive the same dose. Likewise, if two TLDs from different groups of five were mistakenly exchanged, then an error of at least 3 % would facilitate the identification of the misplaced TLDs.

Measurements were made with the phantoms positioned within the cylindrical phantom housing at a SAD of 100 cm. Two separate film stack dosimeter measurements were performed with the film planes oriented parallel and perpendicular to the beam axis. The collimator was rotated such that the short side of the field was normal to the film planes for the parallel exposure of the film stack dosimeter. Consequently, the high dose gradient at the field edge was aligned with the lower-resolution, interfilm axis of the film stack dosimeter.

The dose to water, D_{water}, measured with TLDs was calculated as

$$D_{\text{water}} = (aR + b)k_Q, \tag{4.3}$$

where R is the corrected thermoluminescence from Eq. 3.5, a and b are the coefficients determined from a linear fit of the calibration measurements, and k_Q is a correction for the differences in energy between the beams used for calibration and measurement. As discussed in Sec. 3.2.3, the TLDs were calibrated using a ^{60}Co irradiator, but measurements were made in a 6 MV field. For a given dose, TLD-100 dosimeters underrespond when exposed in a 6 MV field relative to ^{60}Co. To account for the difference in detector response, a value of 1.029 was used for k_Q [Junell and DeWerd, 2009].

4.4.1.6 IMRT delivery quality assurance

To corroborate the results of the general characterization of the film stack dosimeter for 3D dosimetry, the film stack dosimeter was used to verify the delivery of a clinical, seven-field SBRT lung procedure. The treatment plan used the step-and-shoot delivery technique and

a beam energy of 6 MV. For a more stringent test of the film positioning accuracy within the film stack phantom, it was necessary to use a plan with a treated volume smaller than that of the film stack dosimeter. Therefore, the selected SBRT plan was modified using Pinnacle^3 v9.0 TPS (Philips Healthcare, Andover, MA). The MIP of the CTV, delineated on a ten-phase 4DCT image with a slice thickness of 2.5 mm, had a diameter of 1.7 cm. The uniform PTV expansion margin about the MIP volume was reduced to 4 mm to achieve the desired target volume. Afterward, the plan was re-optimized using the existing dose-volume constraints and optimization priorities. The dose distribution was calculated using the Pinnacle adaptive convolve algorithm with a dose grid resolution of $1 \times 1 \times 1$ cm^3. The plan was normalized such that 95 % of the PTV received the prescribed dose of 50 Gy over five fractions.

Prior to measurement with the film stack dosimeter, the delivery of the SBRT plan was verified using the Delta^4 diode array detector (ScandiDos, Uppsala, Sweden). The Delta^4 detector consists of two orthogonal diode boards, intersecting to create an X-shaped cross section. Four PMMA wedges fill the spaces between the boards, creating a cylindrical phantom. Within the central 10 cm extent and 5 cm radius of the detector, the diodes are spaced 5 mm apart; elsewhere, the diodes are spaced 1 cm apart. The treatment fields and corresponding fluence distributions for the treatment plan were copied to a homogeneous, virtual CT dataset of the Delta^4 provided by ScandiDos for IMRT quality assurance applications. The CT dataset had a slice thickness of 2 mm. The total MU for the treatment plan were scaled down by a factor of five to deliver a dose to isocenter of approximately 2 Gy. The dose distribution within the Delta^4 was calculated for treatment with a Clinac® 600C/D accelerator using the IVDT provided by ScandiDos for the virtual CT dataset. The treatment was delivered using a dose rate of 300 MU/min. Two measurements were completed with the Delta^4 detector longitudinally offset by 2.5 mm between measurements to improve the spatial measurement resolution. The two measured dose distributions were

merged and compared with the calculated dose distribution using the gamma index [Low et al., 1998]. Using a global dose tolerance with dose-difference and DTA criteria of 3 % and 3 mm, respectively, the measured and calculated distributions had 99.6 % agreement, thereby verifying the delivery of the treatment plan.

With the completed verification of the SBRT treatment plan delivery, the treatment plan was measured using the film stack dosimeter. A virtual CT dataset of the cylindrical phantom housing was created by modifying the Delta^4 CT dataset using MATLAB®. The dimensions of the cylindrical Delta^4 phantom were reduced to those of the cylindrical phantom housing. At the center of the modified CT image, a volume consistent with the film stack dosimeter was identified and assigned a reduced image value. An IVDT was prepared to assign the cylindrical phantom housing a density of 1.03 g/cm^3, which is consistent with the Virtual Water™ material [Murphy et al., 2004], and the film stack dosimeter a unit density. As discussed in Sec. 3.1.5, the film response was calibrated in terms of dose to water, so it was necessary to calculate the dose to a water medium for comparison. The virtual CT dataset of the cylindrical phantom housing was exported as a DICOM file and imported into the Pinnacle^3 TPS. The planned incident fluence distribution for the SBRT plan was copied to the cylindrical phantom housing dataset, and the dose distribution was calculated using a dose grid resolution of $1 \times 1 \times 1$ mm^3. The delivery of the SBRT treatment was measured twice using the film stack dosimeter positioned within the cylindrical phantom housing. Additionally, the treatment delivery was also measured using the TLD phantom.

4.4.1.7 Film calibration and analysis

As discussed in Sec. 3.1.5, films were scanned in the portrait orientation. The response of the film stack dosimeter was calibrated and analyzed as described in Sec. 3.1.5. The entire area of each film was analyzed, except for a 0.7 mm margin from the outer diameter. Due to the continued polymerization of radiochromic films after exposure [Martišíková et al., 2008],

it is important to maintain a consistent delay between exposure and analysis of the films. Variation in the post-exposure delay prior to analysis creates variation in the measured net OD for a given dose. As with the calibration films, the films used in the film stack dosimeter were scanned individually. However, films within the film stack dosimeter were exposed simultaneously. Therefore, there is an inherent discrepancy in the time that each film was allowed to develop. To minimize the relative variation in the development time of films and the resulting uncertainty in measured dose, films were scanned seven days after exposure.

Masks were laser cut from saturated radiographic films to reproducibly center the films within the scan bed. Given the minimal positioning uncertainty within the film stack dosimeter housing and the reproducibility in the positioning of films on the scanbed, the 3D dose distribution was reconstructed by direct compilation of the individual planar dose distributions. The planar distributions were spaced 1.29 mm apart, accounting for the thickness of the films, film spacers, and air gaps.

4.4.2 Results and discussion

4.4.2.1 Energy dependence

Simulated photon spectra within both the film calibration geometry and the film stack dosimeter geometry without the cylindrical phantom housing are shown in Fig. 4.9 for exposures to 2×2 cm^2 and 5×5 cm^2 fields. The simulated spectra were each normalized to total fluence. Within the film stack dosimeter, variation in the photon spectrum is minimal. However, differences between the photon spectra in the calibration and film stack dosimeter geometries are apparent. The mean absorbed-dose energy response of EBT2 film to each energy spectrum was determined by calculating the fluence-weighted average of the absorbed-dose energy dependence reported by Sutherland and Rogers [2010] for EBT2 lot 020609. The maximum differences in absorbed-dose energy dependence between calibration

Table 4.3: Maximum differences in the absorbed-dose energy dependence, $\Delta f(Q)$, of EBT2 film between several film stack dosimeter geometries and the calibration geometry. For each geometry, $\Delta f(Q)$ differed less than 0.1 % between films within the film stack dosimeter.

Geometry	Field size (cm^2)	$\Delta f(Q)$
Without cylindrical phantom housing	2×2	1.4 %
	5×5	1.2 %
	10×10	1.1 %
With cylindrical phantom housing	2×2	1.2 %
	5×5	1.0 %
	10×10	0.40 %

films and the film stack dosimeter, termed the excess absorbed-dose energy dependence $\Delta f(Q)$, are shown in Table 4.3. The excess absorbed-dose energy dependence differed less than 0.1 % between films within the film stack dosimeter for exposure to a given field size. There is a notable change in the excess absorbed-dose energy dependence as a function of the size of the field incident on the film stack dosimeter, with a maximum difference in energy response of 1.4 % for a 2×2 cm^2 field.

4.4.2.2 Orientation dependence

The simulated dose to the film stack dosimeter as a function of incident beam angle for air gaps of different sizes between films is shown in Fig. 4.10. The error bars denote statistical uncertainty in the simulations of approximately 1 % ($k = 2$). For air gaps of 0 μm and 25 μm between films, the overall variation in the response of the film stack dosimeter is within $\pm$ 1.5 % over all incident beam angles. For air gaps of 50 μm and 100 μm between films, the overall variation in the response of the film stack dosimeter is within $\pm$ 1.5 % for incident beam angles of 0° to 88°. However, for an incident beam angle of 90° relative to the axis normal to the film planes, the film stack dosimeter exhibits an under-response of 3 % relative to 0° incidence for the larger air gaps.

The size of the air gaps between films within the film stack dosimeter was determined to be 15 μm in Sec. 4.3.2. Using the results for air gaps of 0 μm and 25 μm as reference,

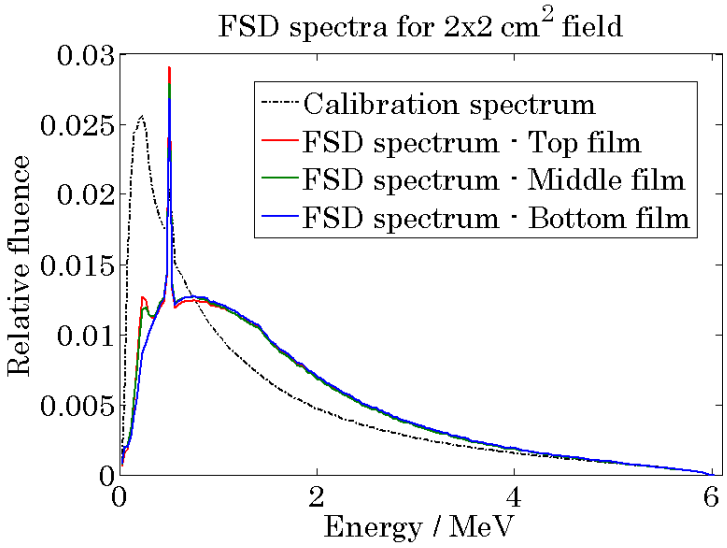

(a)

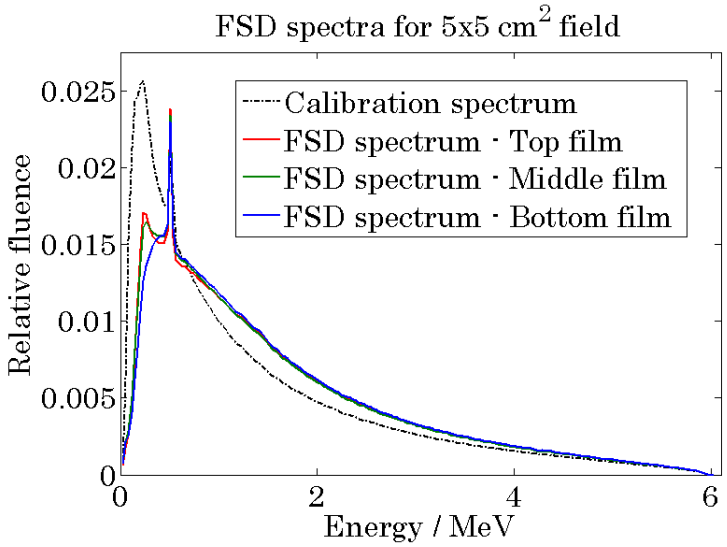

(b)

Figure 4.9: Comparison of the simulated photon spectra through film in the calibration geometry and film in the film stack dosimeter geometry without the cylindrical phantom housing from exposure to a (a) 2×2 cm^2 and (b) 5×5 cm^2 field. Each spectrum is normalized to total fluence.

the overall variation in the response of the film stack dosimeter as a function of incident beam angle is within $\pm 1.5\,\%$.

4.4.2.3 Water equivalence

The results of the water equivalence simulations and measurements are shown in Fig. 4.11. The simulated depth-dose profile was converted to dose as described in Sec. 4.4.1.4. The measured and simulated depth-dose profiles were then normalized to the maximum simulated dose. The PDD profiles measured with the film stack dosimeter oriented parallel and perpendicular to the beam axis agree with the simulated PDD profile within root-mean-square differences of $1.3\,\%$ and $1.2\,\%$, respectively. The PDD-profile measurements with orthogonal film stack dosimeter orientations agree within a root-mean-square difference of $1.4\,\%$, consistent with the results of the orientation dependence simulations.

4.4.2.4 Comparison with TLD measurements

A schematic of the measurement geometry for the film stack dosimeter and TLD measurements of a 1.5×10 cm^2 field is shown in Fig. 4.12. For measurements in the parallel orientation, the beam was incident along the y axis, and the collimator was oriented such that the short side of the field was parallel to the z axis. For measurements in the perpendicular orientation, the beam was incident along the z axis, and the collimator was oriented such that the short side of the field was parallel to the y axis. Profiles from these measurements are shown in Fig. 4.13. The profiles are taken at a depth of 4.1 cm within the cylindrical phantom housing at x offsets of -0.6 cm, 0.0 cm, and 0.6 cm. TLD and film stack dosimeter measurements are shown with overall measurement uncertainties ($k = 2$) of $5.8\,\%$ and $8.0\,\%$-$20\,\%$, respectively. Detailed uncertainty analyses of film stack dosimeter and TLD measurements are provided in Sec. 4.4.2.6. Film stack dosimeter measurements and TLD measurements agree within $5\,\%$ within the field and within 0.5 mm in the field

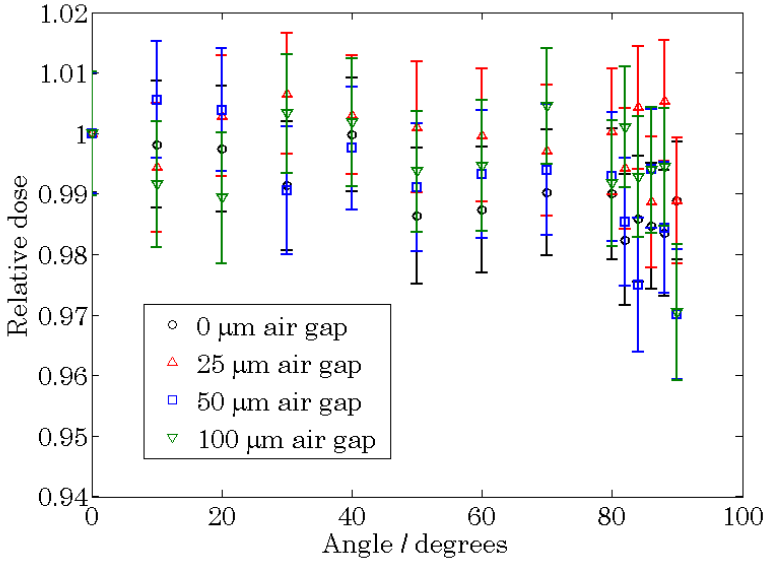

(a)

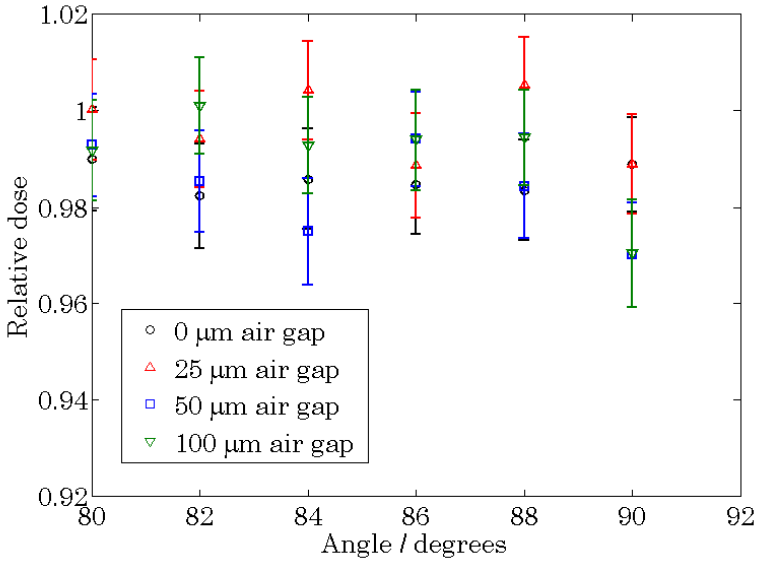

(b)

Figure 4.10: Simulated orientation dependence of the response of the film stack dosimeter. Results are normalized to 0°, where the beam axis is normal to the film planes. Results are shown (a) in 10° increments, from 0° to 90° and (b) in 2° increments from 80° to 90°. Air gaps of multiple sizes were considered between films. Error bars represent statistical uncertainty of 1 % ($k = 2$).

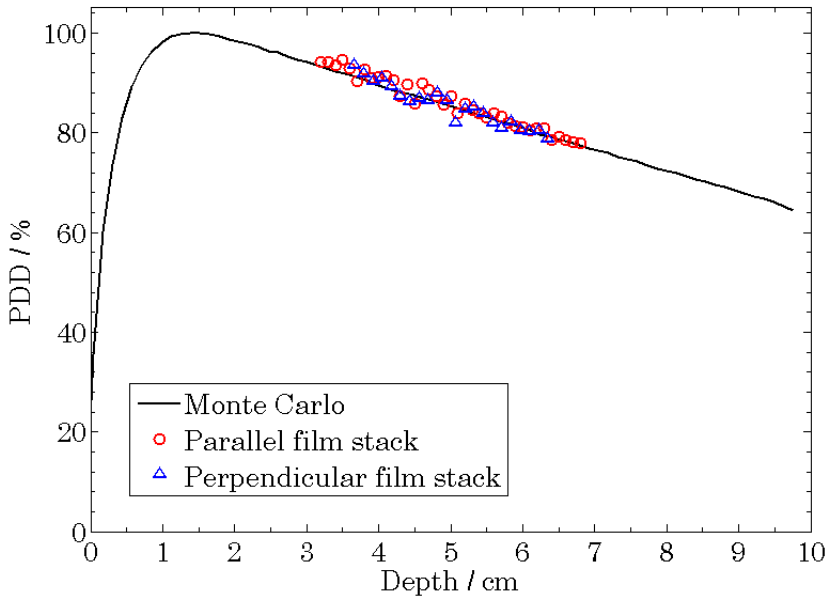

Figure 4.11: Comparison of simulated and measured PDD profiles. Separate measurements were made of a 10×10 cm^2 6 MV field with the film stack dosimeter oriented parallel and perpendicular to the beam axis. Results are presented as a function of depth within the cylindrical phantom housing. The film stack dosimeter measurements were normalized to the maximum simulated dose. For clarity, the measurement in the parallel orientation was interpolated at intervals of 1 mm.

penumbra. Furthermore, the film stack dosimeter measurements in orthogonal orientations agree within a maximum difference of 5 % within the field and 0.5 mm in the field penumbra. However, the field width measured when the beam axis was parallel to the film planes is consistently wider than that measured with the beam axis normal to the film planes.

The consistent discrepancy in field width was investigated further with modifications to the Monte Carlo simulations of orientation dependence described in Sec. 4.4.1.3. The point source was collimated to a circular field with a diameter of 1.5 cm, and the simulations in which the beam axis was oriented parallel or perpendicular to the film planes were repeated. Cylindrical tally volumes were added to the center of each active layer, and in a linear array parallel to the y axis within the central active layer, to simulate the measured field profiles. The resulting profiles simulated for the orthogonal incident beam angles were consistent in width, regardless of the size of the air gaps between films. The most likely cause for the discrepancy in measured profile widths is uncertainty in the spacing of the films within the film stack dosimeter, primarily due to the assumption of uniform gaps between films. Based on the measured profiles, the uncertainty in the film spacing is less than 0.5 mm.

4.4.2.5 IMRT delivery quality assurance

Fig. 4.14 shows dose profiles from the film stack dosimeter and TLD measurements of the SBRT plan, along with the corresponding calculated dose profiles. The coordinate geometry is consistent with that shown in Fig. 4.12. TLD measurements agreed with film stack dosimeter measurements within overall measurement uncertainties ($k = 2$) of 5.8 % and 6.0 %, respectively, as indicated by the error bars in Fig. 4.14. Comparing the two measurements made with the film stack dosimeter, 68 % of points agree within ± 2.75 % and 95 % of points agree within ± 5.5 %.

The calculated dose distribution was imported into MATLAB®. A script was prepared to perform a 3D gamma analysis comparing two input distributions according to

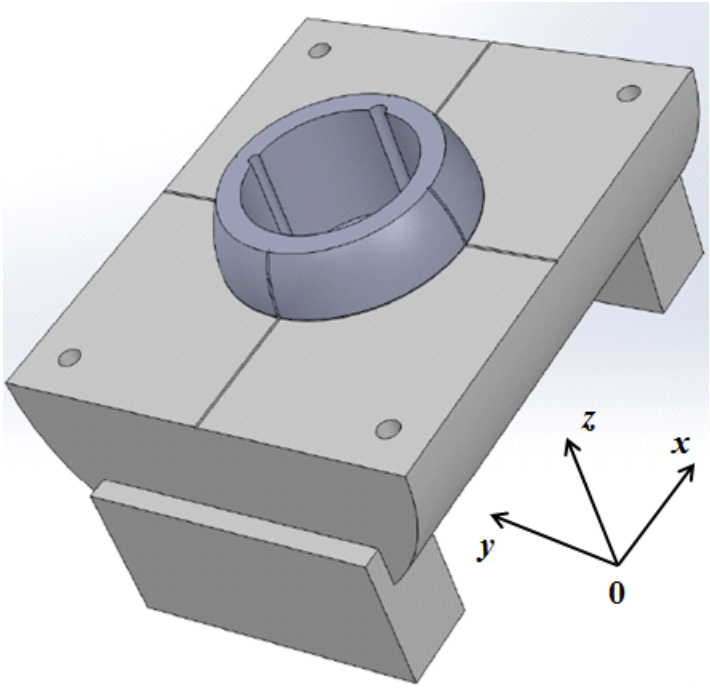

Figure 4.12: Schematic of the coordinate geometry for the measurements of the 1.5×10 cm^2 field. For measurements in the parallel orientation, the beam was incident along the y axis, and the collimator was oriented such that the short side of the field was parallel to the z axis. For measurements in the perpendicular orientation, the beam was incident along the z axis, and the collimator was oriented such that the short side of the field was parallel to the y axis.

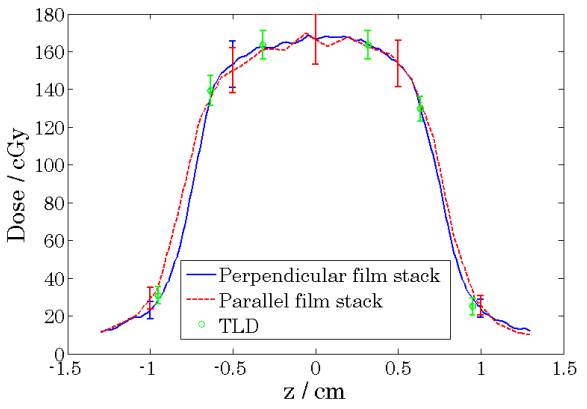

(a)

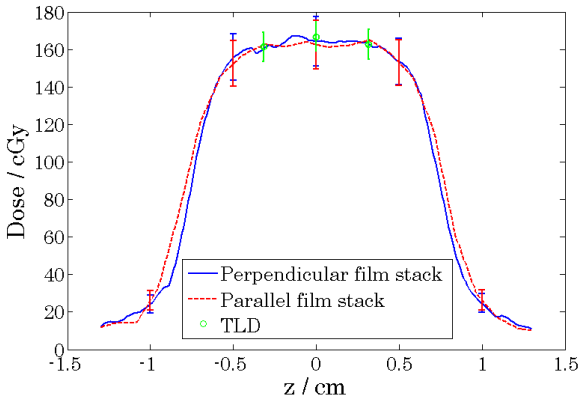

(b)

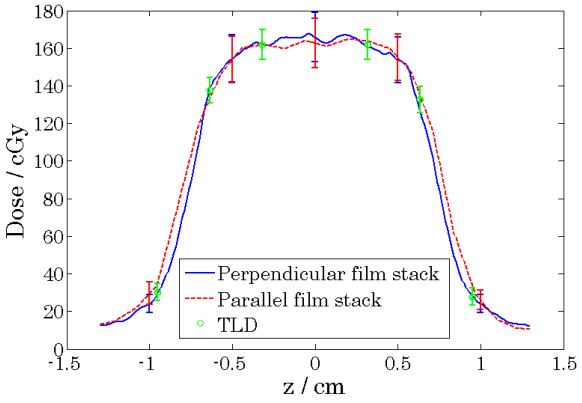

(c)

Figure 4.13: Profile measurements of a 1.5×10 cm^2 6 MV field performed with the film stack dosimeter and TLD microcubes. Separate measurements were made with the film stack dosimeter oriented parallel and perpendicular to the beam axis. Profiles were measured at a depth of 4.1 cm within the cylindrical phantom housing, at offsets along the x axis of (a) -0.6 cm, (b) 0.0 cm, and (c) 0.6 cm. Error bars indicate expanded overall measurement uncertainties ($k = 2$) of 5.8 % for TLD measurements and 8.0 % to 20 % for film stack dosimeter measurements.

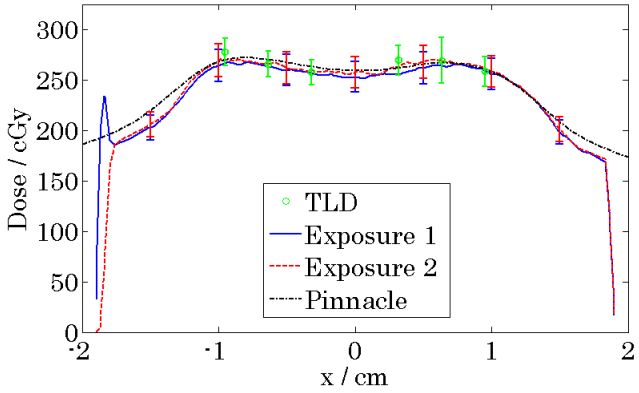

(a)

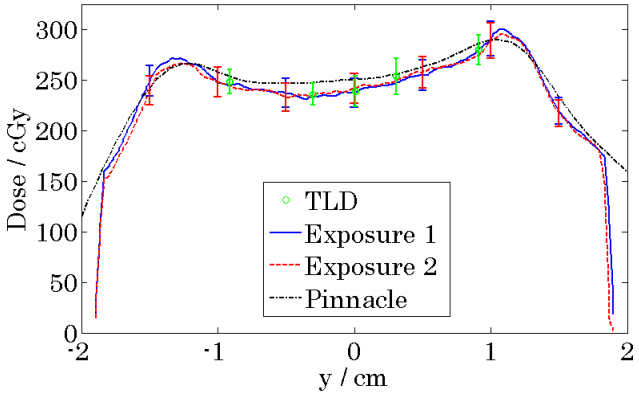

(b)

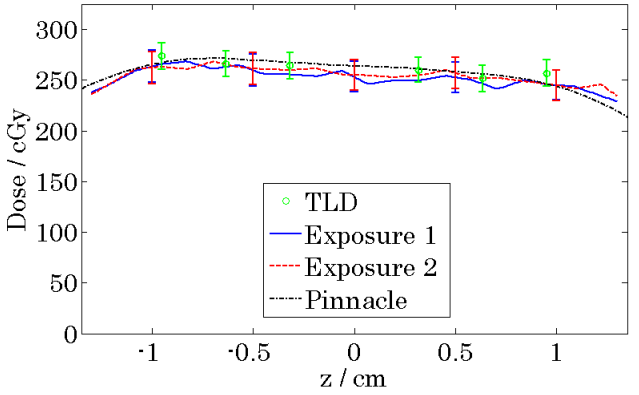

(c)

Figure 4.14: Calculated and measured dose profiles of a SBRT procedure. Two measurements were made with the film stack dosimeter oriented parallel to the treatment couch (Exposure 1 and Exposure 2), and an additional measurement was made with TLD microcubes. Profiles are shown along the axes (a) $y = 0.0$ cm, $z = -0.6$ cm, (b) $x = 0.0$ cm, $z = -0.3$ cm, and (c) $x = -0.6$ cm, $y = 0.0$ cm, where the origin is at isocenter. Error bars indicate expanded overall uncertainties ($k = 2$) of 5.8 % for TLD measurements and 6.0 % for film stack dosimeter measurements.

the methodology from Low et al. [1998]. The calculated distribution was compared with the film stack dosimeter measurements using the 3D gamma index. Because the film stack dosimeter measurements had a higher resolution than the calculated dose distribution, the gamma evaluation was performed for each voxel in the calculated distribution, searching through the measured distribution. Noise in the searched distribution results in an underestimation of delivery errors when using the gamma evaluation [Low and Dempsey, 2003]. To reduce the noise in the measured distributions, a median filter was applied in which each voxel was assigned the median value of the set of neighboring voxels. Using the same gamma criteria that were used with the Delta^4 measurement in Sec. 4.4.1.6, namely, a global dose tolerance with dose-difference and DTA criteria of 3 % and 3 mm, respectively, the film stack dosimeter measurements have 99 % agreement with the calculated dose distribution, which is consistent with the Delta^4 measurement. Using more stringent gamma criteria, namely, a local dose tolerance with dose-difference and DTA criteria of 3 % and 2 mm, respectively, the film stack dosimeter measurements have 96 % agreement with the calculated dose distribution. Moreover, the film stack dosimeter and Delta^4 measurements identified similar trends between the delivered and calculated dose distributions, including an underdosed region near the center of the treated volume, which is visible in Fig. 4.14b. The agreement between the film stack dosimeter measurements and the calculated dose to water and TLD measurements, as well as the consistency with Delta^4 measurements, further validates the results of the film stack dosimeter characterization.

4.4.2.6 Uncertainty analysis

The uncertainty budgets for measurements with the film stack dosimeter and TLD microcubes are given in Tables 4.4 and 4.6, respectively. All Type B uncertainties were conservatively assumed to follow rectangular distributions. The uncertainties provided in the

tables were estimated by propagating the uncertainty in each parameter through the appropriate dose determination equation (i.e., Eq. 3.3 or 4.3).

Film stack dosimeter The uncertainty in the film stack dosimeter measurements is a function of dose. The uncertainty budget shown in Table 4.4 is for film exposed to a dose of 340 cGy; the variation in uncertainty with dose is shown in Fig. 4.15. The uncertainty due to differences in the postexposure delay prior to scanning was estimated based on the development of EBT film as a function of time determined by Martišíková et al. [2008], assuming an uncertainty of ± 2 h. The ± 2 h uncertainty is primarily due to exposing and scanning calibration films and the film stack dosimeters at the same time. If film stack dosimeters are exposed and scanned separately from calibration films, then an uncertainty in the postexposure delay of ± 15 min is readily achievable. From the results of Devic et al. [2010], an uncertainty of ± 2 h in development time results in a dose uncertainty of $\pm 1\,\%$ for films scanned 24 h after exposure. Assuming the development of the film is linear with time within that 4 h window, then an uncertainty of ± 15 min in the postexposure delay would result in a dose uncertainty of $0.13\,\%$. Therefore, the film stack dosimeter can be scanned as little as 24 h after exposure without greatly impacting the measurement uncertainty.

The intrafilm uniformity considered the uncertainty due to variations in the net OD over the analyzed region of a single film. This was determined by taking the standard deviation of the pixel value within the analyzed region of each calibration film. For films exposed to a given dose, the maximum standard deviation was propagated through the dose determination to estimate the uncertainty. The uncertainty in the background scanner signal was determined in the same way, but instead using the image of the saturated radiographic film.

The interfilm uniformity accounted for differences in the net OD of multiple films exposed to the same dose. The uncertainty due to interfilm uniformity was determined by taking the standard deviation of the net OD of films exposed to the same dose. Additionally, since

Table 4.4: Uncertainty budget for the film stack dosimeter measurements. The values shown are percentage uncertainties propagated through the dose determination. The intrafilm and interfilm uniformity, as well as the calibration uncertainty, are dependent on the dose to the film; the estimates shown are for a dose of 340 cGy.

Parameter	Type A	Type B
Post-exposure delay		0.05
Intrafilm uniformity	1.1	
Interfilm uniformity	0.92	
Positioning		0.23
Scanner background	0.75	
Energy dependence		0.81
Orientation dependence		0.72
Water equivalence		0.75
Quadratic sum	1.6	1.3
A and B Quadratic sum	2.1	
Film calibration	2.2	
Total uncertainty	3.0 ($k = 1$)	
Expanded total uncertainty	6.0 ($k = 2$)	

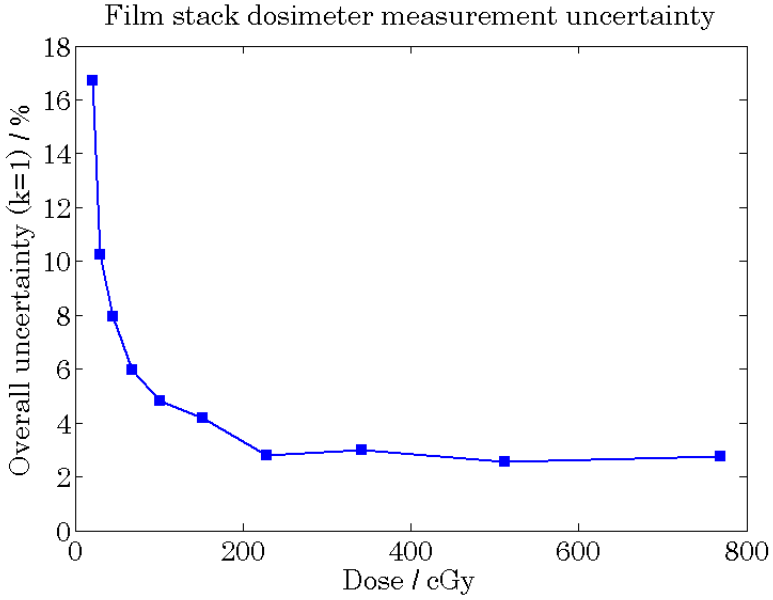

Figure 4.15: Overall uncertainty ($k = 1$) in film stack dosimeter measurements as a function of dose.

six films were individually scanned for each dose, the uncertainty in interfilm uniformity also accounts for uncertainty due to scanner stability. Based on analysis of the images of the neutral density filters positioned on the scanbed, the scanner signal deviated less than 0.5 % from a baseline level.

A positioning uncertainty of ± 2 mm was assumed. The resulting uncertainty in dose was determined by calculating the relative difference in dose at a distance of 1 m from the source due to a 2 mm change in position based on the inverse-square reduction in fluence with distance.

The uncertainty due to the energy dependence, orientation dependence, and water equivalence of the film stack dosimeter were estimated based on the variations in response determined in this thesis work due to each of these parameters. For instance, a maximum energy dependent response of ± 1.4 % was observed. Assuming a rectangular distribution for the variation in response gives an uncertainty contribution of 0.81 %. For the measured air gap size of 15 μm, the maximum orientation dependent response was ± 1.25 %; a rectangular distribution was again assumed. The maximum root-mean-square difference between PDD profiles measured with the film stack dosimeter and simulated within a water volume was 1.3 %. Assuming that the difference distribution is rectangular, this corresponds to an uncertainty of 0.75 %.

The uncertainty budget for the film calibration is shown in Table 4.5. Contributions to uncertainty from intrafilm and interfilm uniformity, positioning, and background scanner signal were estimated as previously discussed. The uncertainty from the dose-rate measurement was estimated using an adaption of Table II from the addendum to AAPM Task Group 51 [McEwen et al., 2014]. The uncertainty from the calibration curve fit was estimated by propagating the uncertainty in the fit parameters of Eq. 3.3 through the dose determination. The uncertainty in the fit parameters was quantified based on the 95 % confidence intervals of the nonlinear regression.

Table 4.5: Uncertainty budget for the film stack dosimeter calibration. The values shown are percentage uncertainties propagated through the dose determination. The intrafilm and interfilm uniformity are dependent on the dose to the film; the estimates shown are for a dose of 340 cGy.

Parameter	Type A	Type B
Intrafilm uniformity	1.1	
Interfilm uniformity	0.92	
Positioning		0.23
Scanner background	0.75	
Dose-rate measurement		1.3
Calibration curve fit		0.69
Quadratic sum	1.6	1.5
Total calibration uncertainty	2.2 ($k = 1$)	
Expanded total calibration uncertainty	4.4 ($k = 2$)	

TLD The estimated uncertainty in the TLD measurements is specific to each dosimeter due to the determination of the thermoluminescence reproducibility. The uncertainty budget shown in Table 4.6 represents the median uncertainty; the overall measurement uncertainty for each dosimeter is shown in Fig. 4.16. Repeated measurements of a given exposure were not made with the TLD phantom, so the thermoluminescence reproducibility was estimated using the standard deviation in chip factors for each dosimeter over a series of nine exposures. The standard deviation in the raw thermoluminescence reading could not be used because different TLD readers with differing sensitivities were used throughout this thesis work. The uncertainty in the chip factor was propagated through the dose determination.

A positioning uncertainty of ± 2 mm was assumed. The resulting uncertainty in dose was determined by calculating the relative difference in dose at a distance of 1 m from the source due to a 2 mm change in position based on the inverse-square reduction in fluence with distance. Although the reader stability should be accounted for with the thermoluminescence reproducibility, this uncertainty was conservatively included based on the uncertainty budget from Nunn et al. [2008]. The uncertainty in the energy dependence correction was taken from Junell and DeWerd [2009].

Table 4.6: Uncertainty budget for TLD microcube measurements. The values shown are percentage uncertainties propagated through the dose determination. The thermoluminescence reproducibility is dependent on the dosimeter; the estimates shown represent the median uncertainty.

Parameter	Type A	Type B
Thermoluminescence reproducibility	1.3	
Positioning		0.23
Reader stability		0.20
Energy dependence		2.1
Quadratic sum	1.3	2.1
A and B Quadratic sum	2.5	
TLD calibration	1.5	
Total uncertainty	2.9 ($k = 1$)	
Expanded total uncertainty	5.8 ($k = 2$)	

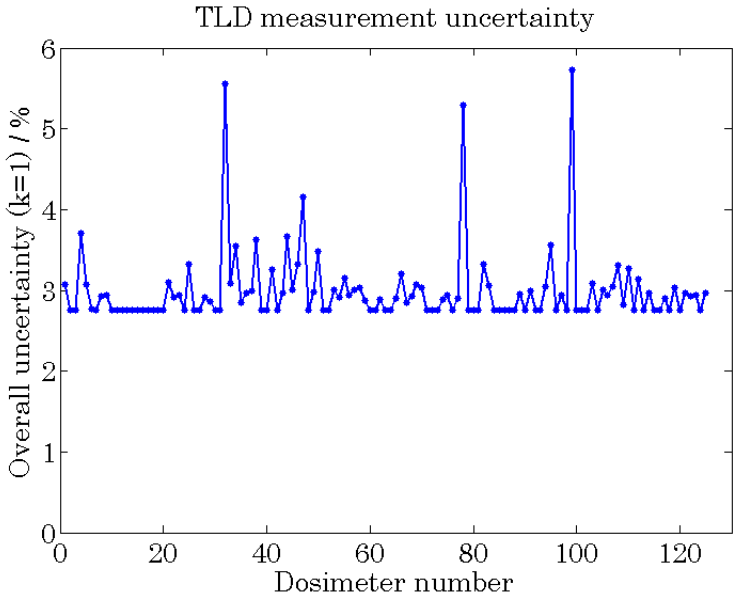

Figure 4.16: Overall uncertainty ($k = 1$) in TLD measurements for each dosimeter.

Table 4.7: Uncertainty budget for TLD microcube calibration. The values shown are percentage uncertainties propagated through the dose determination. The thermoluminescence reproducibility is dependent on the dosimeter; the estimates shown represent the median uncertainty.

Parameter	Type A	Type B
Air-kerma-rate measurement	0.73	
Conversion of air kerma to dose to water		0.14
Positioning		0.23
Reader stability		0.20
Thermoluminescence reproducibility	1.3	
Calibration curve fit		0.10
Quadratic sum	1.5	0.35
Total calibration uncertainty	1.5 ($k = 1$)	
Expanded total calibration uncertainty	3.0 ($k = 2$)	

The uncertainty budget for the TLD calibration is shown in Table 4.7. Contributions to uncertainty from positioning, reader stability, and thermoluminescence reproducibility were determined as previously discussed. Uncertainty in the air-kerma-rate measurement was determined from the UWADCL uncertainty budget for ^{60}Co air-kerma calibrations. The uncertainty in the Monte Carlo-based conversion from air kerma to dose to water was obtained from Raffi [2010]. The uncertainty in the calibration curve fit was estimated by propagating the standard deviation of the fitting parameters determined using linear regression through the dose determination.

4.5 Conclusions

A radiochromic film stack dosimeter was developed using Gafchromic® EBT2 film and characterized for the dosimetry of megavoltage photon beams. In the megavoltage energy range, the film stack dosimeter is energy independent within 1.5 %, orientation independent within ± 1.25 %, and water equivalent within ± 1.5 %. Film stack dosimeter measurements agreed with TLD measurements within an overall measurement uncertainty of 6.0 % ($k = 2$). Using dose-difference and DTA criteria of 3 % and 3 mm, respectively, film stack dosimeter

measurements of an IMRT procedure had 99 % agreement with the calculated dose distribution.

Chapter 5

Development and verification of a Monte Carlo linear accelerator model

5.1 Linear accelerator modeling procedure

In this chapter, the development and verification of a Monte Carlo model of a linear accelerator is discussed. The general procedure for generating a Monte Carlo linear accelerator model was outlined by Sheikh-Bagheri and Rogers [2002b], which investigated the dependence of simulated PDD profiles and in-air, off-axis output factors on the mean energy, energy distribution, radial intensity distribution, and divergence of the electron beam incident on the bremsstrahlung target. It was determined that the off-axis factors are dependent on mean energy and intensity distribution, while the PDD profiles are dependent primarily on mean energy, with a weak dependence on energy distribution. Thus, the authors recommend the following iterative procedure to model a linear accelerator:

- Model the physical components of the accelerator using specifications from the manufacturer.
- Using the nominal electron energy distribution, adjust the mean electron energy to match simulated PDD profiles with measured PDD profiles.
- Adjust the electron radial intensity distribution to match simulated and measured off-axis factors. If satisfactory agreement cannot be achieved, then adjust the mean electron energy as needed.
- Verify that the simulated and measured PDD profiles still agree.

A more recent study of the sensitivity of photon beam characteristics to electron beam parameters found that variation in the electron energy distribution far exceeding the nominal distribution did not result in any variation in simulated profiles, and recommended that a monoenergetic electron beam should be assumed [Chibani et al., 2011]. This study considered crossline (i.e., along the axis of lateral couch motion) and inline (i.e., along the axis of longitudinal couch motion) field profiles instead of off-axis output factors, and investigated photon beam characteristics for field sizes of 2×2 cm^2, 10×10 cm^2, and 35×35 cm^2. Of the three field sizes, the 2×2 cm^2 field was found to be the most sensitive to changes in the mean electron energy and the radial intensity distribution.

The use of crossline and inline field profiles or off-axis factors to evaluate a photon beam model creates an iterative procedure due to the dependence of these characteristics on the mean electron energy. A more direct modeling procedure, in which the radial intensity distribution is determined by matching the penumbra of simulated and measured fields, was proposed by Almberg et al. [2012]. The geometric penumbra is determined by the positions of the jaws, which are fixed for a given field size, and the source size, which is given by the radial intensity distribution. Assuming that scatter and transmission penumbrae do not appreciably impact the overall penumbra over a realistically narrow energy range,

then the radial intensity distribution can be determined by matching the simulated and measured penumbrae. Almberg et al. [2012] verified the validity of this assumption over an energy range of 0.4 MeV, and proposed the following linear accelerator modeling procedure motivated by the results of Chibani et al. [2011]:

- After modeling the physical accelerator components, adjust the mean electron energy to match simulated and measured PDD profiles for a small (i.e., 5×5 cm^2) field.
- Adjust the radial intensity distribution to match simulated and measured penumbrae for a small (i.e., 5×5 cm^2) field.
- Adjust the electron divergence to match simulated and measured transverse profiles for a large (i.e., 40×40 cm^2) field.

In this thesis work, the Almberg method was employed to model the 6 MV beam from the Clinac® 21EX linear accelerator at the University of Wisconsin Medical Radiation Research Center (UWMRRC) [Almberg et al., 2012]. However, because the maximum field size of interest in this work was 10×10 cm^2, a non-divergent electron beam was assumed.

5.2 Measurement of beam data

For reference with the Monte Carlo model, PDD, inline, and crossline profiles were measured for the 6 MV beam from the UWMRRC Clinac® 21EX accelerator. Profile measurements were made using the Standard Imaging DoseView3D scanning water tank. Profiles for fields larger than 4×4 cm^2 were measured using a Standard Imaging A18 ionization chamber, while profiles of fields 4×4 cm^2 and smaller were measured using a Standard Imaging D1H diode. Profiles were measured by continuously scanning the ionization chamber or diode. To account for temporal variations in the linear accelerator output, a second A18 ionization chamber was positioned within the field as a reference.

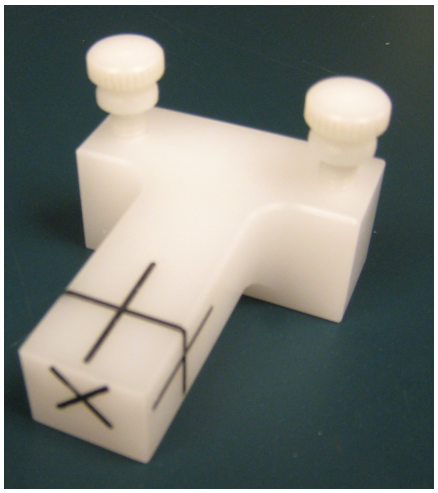

Figure 5.1: Alignment device used for leveling and centering the scanning axes of the water tank. The device was centered within the field by aligning the cross on top with the field crosshair. The level of the water surface was defined by shifting the device vertically until the submerged portion of the X and its reflection on the water surface formed a complete X.

With the gantry and collimator positioned at 0°, the water tank was centered within the light field using the crosshair as a reference. Using the alignment device shown in Fig. 5.1, the position of the water surface along the vertical scanning axis was located by shifting the vertical position until the submerged portion of the X and its reflection on the water surface formed a complete X. The alignment device was then translated along the inline and crossline axes; the level of the motion axes was adjusted as necessary to keep the alignment device at the water surface. Once the scanning axes were leveled, the scanning origin was set by centering the alignment device within the light field using the crosshair. With the alignment of the motion axes complete, the alignment device was replaced with the scanning dosimeter. The scanning origin was then redefined with the ionization chamber shifted by a distance of $0.6r_{\text{cav}}$ away from the source, where r_{cav} is the radius of the air cavity within the ionization chamber, or with the diode shifted 0.7 mm toward the source, to align the effective point of measurement with the water surface [Almond et al., 1999]. Finally, the water tank was positioned at a SSD of 100 cm using the optical distance indicator.

For each field size measured, the reference ionization chamber was positioned in the corner of the radiation field, as indicated by the shadow in the light field, outside of the path of the scanned dosimeter. PDD, inline, and crossline profiles were measured for 2×2 cm^2, 3×3 cm^2, 4×4 cm^2, 5×5 cm^2, and 10×10 cm^2 fields defined by the jaws. PDD scans were initiated at a depth of 30 cm and progressed toward the water surface to minimize the rippling of the water during the scan. Inline and crossline scans extended 6 cm beyond the full-width-at-half-maximum (FWHM) of each field. The slow scan speed setting was used with a step size of 0.1 cm and a sampling window of 200 ms.

Crossline and inline profiles were also measured for fields defined by the MLC to verify the MLC model. The Clinac® 21EX accelerator has the Millennium 120 MLC which is comprised of 60 opposing leaf pairs: the central 40 leaf pairs have a 5 mm width projected to the isocenter plane, and the outer 20 leaf pairs have a 1 cm width projected to the isocenter plane. A schematic of the Millennium 120 MLC is shown in Fig. 5.2. This MLC has a tongue-and-groove arrangement to minimize leakage between adjacent leaves. The leaf tips are rounded to maintain an approximately constant penumbra as a function of field size. As seen in the cross-section view of the MLC, the leaf edges diverge from the source. For the profile measurements of MLC-defined fields, the MLC leaf positions were defined using the Varian® MLC Shaper tool. Abutments of opposing leaves were positioned off center to avoid scanning the detector along a leaf junction. For each field, one outermost leaf on each bank was fully retracted to keep the MLC carriages outside of the scanned profile. Additionally, the detector was shifted 2.5 mm (i.e., one-half leaf width) off center for crossline scans to avoid scanning along interleaf junctions.

5.3 Linear accelerator geometry

A Monte Carlo model of the Clinac® 21EX accelerator was created using the EGSnrc user code BEAMnrc [Rogers et al., 1995]. This user code is further discussed in Sec. 5.4.1.1. A

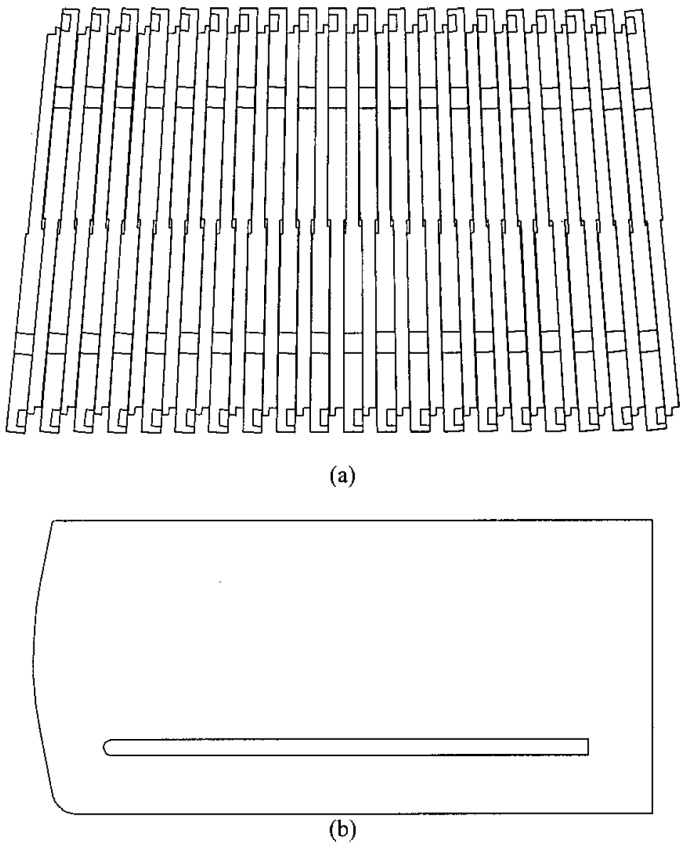

Figure 5.2: Schematic of the Millennium 120 MLC [Kim et al., 2001]. (a) Cross-sectional view of the central 40 leaf pairs showing the divergent design of the leaves and the tongue-and-groove arrangement. (b) Side view of an individual leaf showing the rounded leaf-tip design.

rendering of the model is shown in Fig. 5.3. The physical components within the head of the linear accelerator were modeled according to the dimensions and materials specified by Varian®. In particular, the bremsstrahlung target, copper target backing, primary collimator, vacuum window, flattening filter, monitor chamber, mirror, x and y jaws, Millennium 120 MLC, and light reticule were modeled.

5.4 Development of the linear accelerator model

5.4.1 EGSnrc

The EGSnrc radiation transport code was used to generate the model of the Clinac® 21EX accelerator because this Monte Carlo code has user codes designed both for the modeling of linear accelerators (BEAMnrc) and for the simulation of dose distributions in CT datasets (DOSXYZnrc). In particular, the BEAMnrc user code has a built-in macro for the modeling of the Varian® Millennium 120 MLC with dynamic positioning capability for the simulation of IMRT fields, and the DOSXYZnrc user code has a built-in script to convert CT datasets to the material and density datasets necessary for Monte Carlo radiation transport simulations.

EGSnrc simulations require that material data files containing interaction cross sections as a function of energy for each material in the simulation geometry be input separately. In this work, material data files were generated for photon energies ranging from 0.01 MeV to 55 MeV, and for electron energies ranging from 0.521 MeV to 55 MeV, corresponding to a minimum electron kinetic energy of 0.01 MeV. These data files included density corrections and radiative stopping powers from ICRU report 37 [1984]. Cross sections for Rayleigh interactions were not included in the material data files.

Several different radiation transport settings, primarily impacting sampling algorithms or interaction models used during particle transport, can be adjusted in EGSnrc simulations. Based on the results of Egan and Laub [2013], the default settings were used for the electron

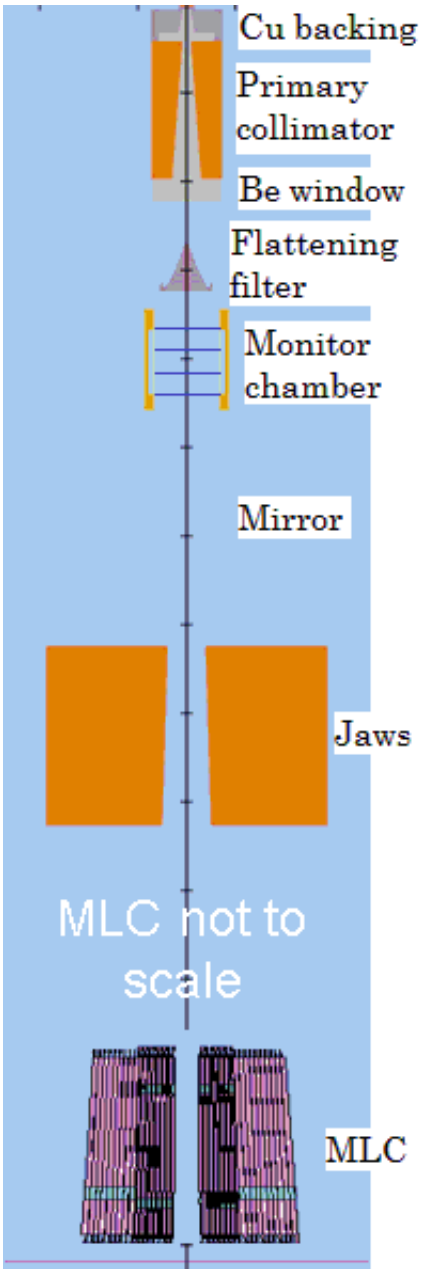

Figure 5.3: Rendering of the BEAMnrc model of the Clinac® 21EX accelerator through the $x = 0$ plane. The modeled components are as follows: target, copper backing, primary collimator, beryllium window, flattening filter, monitor chamber, mirror, jaws, MLC, and light reticule. The mirror is too thin to be visualized. The rendering plane lies within the opening of the x jaws, so they are not visible. The MLC is rendered separately, and thus is not to scale.

boundary crossing and electron-step algorithms, and for all interaction cross sections other than bremsstrahlung interactions. The bremsstrahlung angular sampling was set to the KM option to use the higher-order bremsstrahlung angular sampling from Koch and Motz [1959] instead of just the leading term. Additionally, the NRC bremsstrahlung cross sections were used. These cross sections are identical to the NIST cross sections [Seltzer and Berger, 1985], which are the basis for the radiative stopping powers provided in ICRU report 37 [1984], but with corrections applied for electron-electron bremsstrahlung. The ECUT and PCUT variables, which set the energy at which electron and photon transport, respectively, are terminated and the residual energy deposited locally, were set to 0.521 MeV (including rest mass) and 0.01 MeV.

5.4.1.1 BEAMnrc

The BEAMnrc user code for EGSnrc was developed specifically for the modeling of high-energy radiotherapy treatment units [Rogers et al., 1995]. Accelerators are modeled with this user code by specifying a series of component modules, corresponding to the physical components within the head of the linear accelerator, and their positions along the beam axis. Phase-space files, which contain the particle type, position, velocity, energy, and weight of each particle crossing a specified plane, can be scored in BEAMnrc simulations and then used as the particle source in subsequent simulations. The use of phase-space sources improves the efficiency of a series of simulations that use the same source by reducing the number of times the computationally expensive process of bremsstrahlung production must be simulated. However, phase-space sources also require increased storage capacity, since phase-space files can contain gigabytes of data.

To further improve the efficiency of linear accelerator simulations, BEAMnrc has a bremsstrahlung splitting variance reduction technique. Bremsstrahlung splitting improves simulation efficiency by reducing the number of electrons that must be transported to gener-

ate a given number of bremsstrahlung photons. When bremsstrahlung splitting is employed, normal transport of electrons is performed until a bremsstrahlung interaction occurs. Rather than create a single photon from a single bremsstrahlung interaction, N_{split} photons are created, each with weight $1/N_{split}$ relative to the weight of the interacting electron. The appropriate energy and angular distributions are sampled for each photon. The energy of the interacting electron is reduced by the energy of the first photon produced; therefore, energy is conserved on average.

Multiple bremsstrahlung splitting techniques are available in BEAMnrc, the most efficient of which is directional bremsstrahlung splitting (DBS) [Kawrakow et al., 2004]. With DBS, a splitting radius is specified at a given distance from the source, defining a conical volume. When bremsstrahlung photons are generated, Russian Roulette is performed on any photons that are not directed within this conical volume. A survival threshold of $1/N_{split}$ is established, and a random number is sampled for each photon directed outside of the conical volume. If the random number exceeds the survival threshold, then the photon is terminated; otherwise, the photon weight is increased by a factor of N_{split}. Thus, the result of DBS is a large number of low-weight photons directed within the desired field, with few high-weight photons directed outside of the desired field. Fragoso et al. [2009] demonstrated that simulated PDD and transverse field profiles for 10×10 cm^2 fields using DBS were consistent within 1 % with simulated profiles that did not use any variance reduction techniques.

5.4.1.2 DOSXYZnrc

The DOSXYZnrc user code for EGSnrc simulates dose distributions in rectilinear, voxelized geometries. Phase-space files generated in BEAMnrc simulations can be used as sources for DOSXYZnrc simulations, allowing for dose computations in complicated geometries from irradiation with a modeled accelerator. In particular, the DOSXYZnrc user code includes

the script CTCREATE, which converts CT datasets into voxelized geometries that can be used in simulations. This script uses the information in the accompanying IVDT to assign a material to each range of image values, thereby permitting the conversion of the CT data to the material and density datasets required for a Monte Carlo simulation. Simulated dose distributions are output in the form of 3DDOSE files, which contain the coordinates, dose, and standard deviation in dose for each voxel in the geometry.

When phase-space files are used as sources in DOSXYZnrc simulations, the results are normalized per starting source particle in the simulation used to generate the phase-space file. If more histories are required to achieve the desired statistics than there are particles in the phase-space file, then particles can be re-used. The parameter NRCYCL defines the number of times each particle in the phase-space source should be re-used. If the set value of NRCYCL is not sufficient to produce the desired number of histories, then the phase-space file is restarted and additional particles are sampled. When the phase-space particles are recycled, they are appropriately treated as correlated for the determination of simulation uncertainty. However, when a phase-space file is restarted, resampled particles are treated as independent, producing an erroneously low estimate of the simulation uncertainty [Walters et al., 2002]. In this work, a MATLAB® script was prepared to calculate the appropriate value of NRCYCL to run a given number of histories using a phase-space source containing a known number of particles.

5.4.2 Verification of BEAMnrc simulation techniques

In this thesis work, both DBS and phase-space sources were used to improve simulation efficiency. Prior to the application of these techniques, it was verified that the implementation in this work did not significantly impact the results.

5.4.2.1 Directional bremsstrahlung splitting

For the implementation of DBS, each bremsstrahlung interaction was split 1000 times. Kawrakow et al. [2004] demonstrated that this degree of splitting produces near-optimum simulation efficiency, and Fragoso et al. [2009] chose this value for the splitting parameter in their investigation of efficiency-enhancing parameters. Whereas previous investigations [Kawrakow et al., 2004; Fragoso et al., 2009] have used a splitting radius of 10 cm defined at a distance of 100 cm from the source for the simulation of 10×10 cm^2 fields, in this work a larger splitting radius of 15 cm at 100 cm was conservatively used.

To verify the implementation of DBS, a phase-space file was tallied at the exit of the linear accelerator head in BEAMnrc simulations both using the above DBS settings and without DBS. These phase-space files were generated for simulations of 3×3 cm^2 and 10×10 cm^2 fields. The energy spectra of photons within the phase-space files for corresponding field sizes were nearly indistinguishable. These phase-space files were each used as sources in DOSXYZnrc simulations of a $35 \times 35 \times 35$ cm^3 water volume comprised of $5 \times 5 \times 5$ mm^3 voxels at a SSD of 100 cm. PDD and crossline profiles from these simulations are shown in Fig. 5.4. For each field size, the profiles simulated with and without the use of DBS agree within the statistical uncertainty of the simulations (0.5 %, $k = 1$), so this implementation of DBS does not significantly impact simulated dose profiles.

The use of Russian Roulette on bremsstrahlung photons directed outside of the defined splitting radius creates a small number of high-weight particles. These particles can degrade the relative error of a simulation and produce erroneous results. DOSXYZnrc provides simulation results both with and without contributions from high-weight particles. These results were identical for the simulations that used DBS, confirming that high-weight particles did not contribute to the tallies.

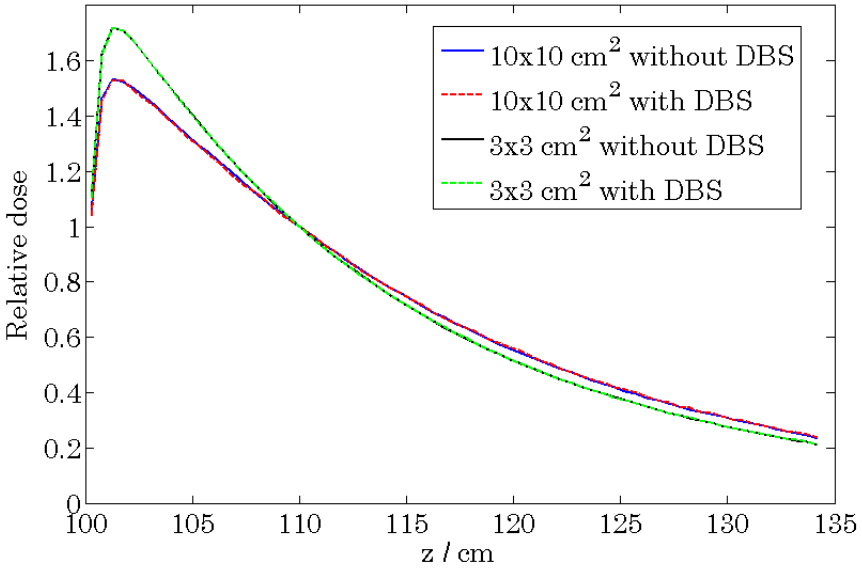

(a)

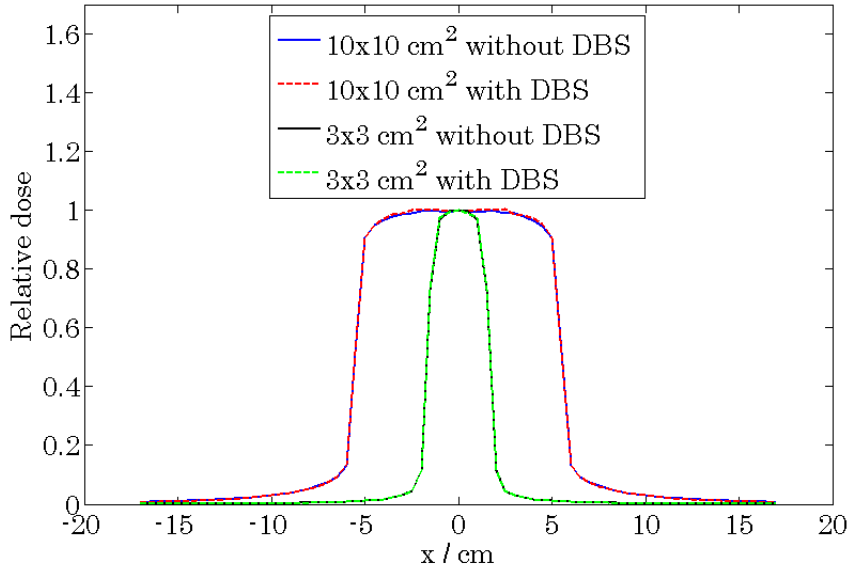

(b)

Figure 5.4: Comparison of simulated (a) PDD and (b) crossline profiles both with and without the use of DBS for 3×3 cm^2 and 10×10 cm^2 fields. Profiles were normalized to the dose at a depth of 10 cm along the beam axis.

5.4.2.2 Phase-space sources

As previously mentioned, the most time consuming component of the simulation of linear accelerators is the generation of the bremsstrahlung beam from electron interactions in the target. This process is made more efficient with the use of DBS by reducing the number of electron histories that must be simulated to produce a given number of bremsstrahlung photons. Additional improvements in efficiency can be made by limiting the number of times the bremsstrahlung production process is simulated. For instance, the components in the head of the linear accelerator can be divided into those with fixed and variable positions. While both the jaws and MLC change position with the simulation of different field sizes, all components above the jaws remain fixed. Therefore, a phase-space file can be tallied between the fixed and variable components of the accelerator head and used as a source for all ensuing simulations, requiring just a single simulation of the bremsstrahlung production process.

However, this approach assumes that changes in the scattered radiation above the jaws due to changes in the positions of the MLC and jaws are negligible. To verify this assumption, phase-space files were tallied at the exit of the accelerator head for two simulations of a given field size. The first phase-space file was generated in a BEAMnrc simulation in which transport of the electron beam through the bremsstrahlung target was modeled. The second phase-space file was generated in a BEAMnrc simulation that used a phase-space source located above the jaws, which itself was generated in a separate BEAMnrc simulation in which transport of the electron beam through the bremsstrahlung target was modeled with fully retracted jaws and MLC. The two phase-space files tallied at the exit of the accelerator head were then used in DOSXYZnrc simulations of the same water volume used in Sec. 5.4.2.1. Resulting PDD and crossline profiles from simulations of 3×3 cm^2 and 10×10 cm^2 fields are shown in Fig. 5.5. For each field size the profiles are nearly identical, demonstrating agreement well within the relative simulation uncertainty of 0.5 % ($k = 1$).

Therefore, the division of particle transport through the accelerator head into two BEAMnrc simulations does not significantly impact resulting simulations of dose distributions.

5.4.3 Optimization of modeled beam parameters

Prior to the optimization of the parameters for the electron beam incident on the bremsstrahlung target, consistency between the simulated and physical linear accelerator geometries was confirmed. In DOSXYZnrc simulations, beam angles are specified using spherical coordinates. Additionally, the modeled and physical jaws and MLC use different naming conventions, so it was necessary to verify the correspondence of the modeled and physical geometries. In this work, the coordinate transformation described by Zhan et al. [2012] was applied to convert the desired gantry, collimator, and couch angles into the necessary spherical coordinates for the DOSXYZnrc input file. Consistency between the physical and simulated geometries was then verified with the simulation of a field with asymmetric jaw settings. The two x jaws were retracted 1 cm and 5 cm from the center of the field, while the two y jaws were retracted 2.5 cm and 10 cm from the field center. Thus, it was possible to uniquely identify the collimator orientation relative to the Monte Carlo geometry based on the simulated dose distribution. Simulations were completed for the cardinal gantry, couch, and collimator orientations to verify consistency between the physical and simulated geometries.

The procedure for the optimization of electron beam parameters required the simulation of PDD, crossline, and inline profiles for multiple field sizes and a number of different electron beam energies and radial intensity distributions. Given the minor variations in the large volume of simulations that needed to be run, template input files were prepared. MATLAB® scripts were prepared to populate the variable input fields of the template files. A MATLAB® script was also prepared to analyze the dose distributions output in the 3DDOSE file format.

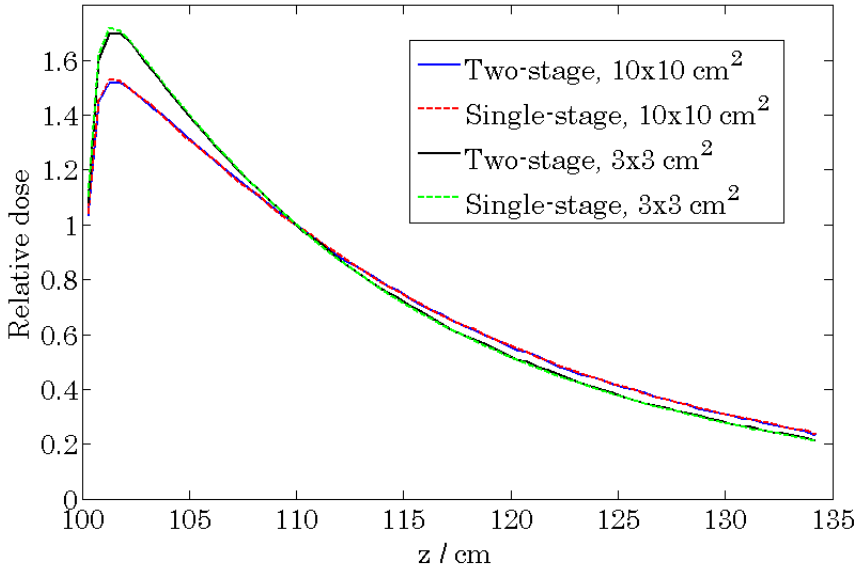

(a)

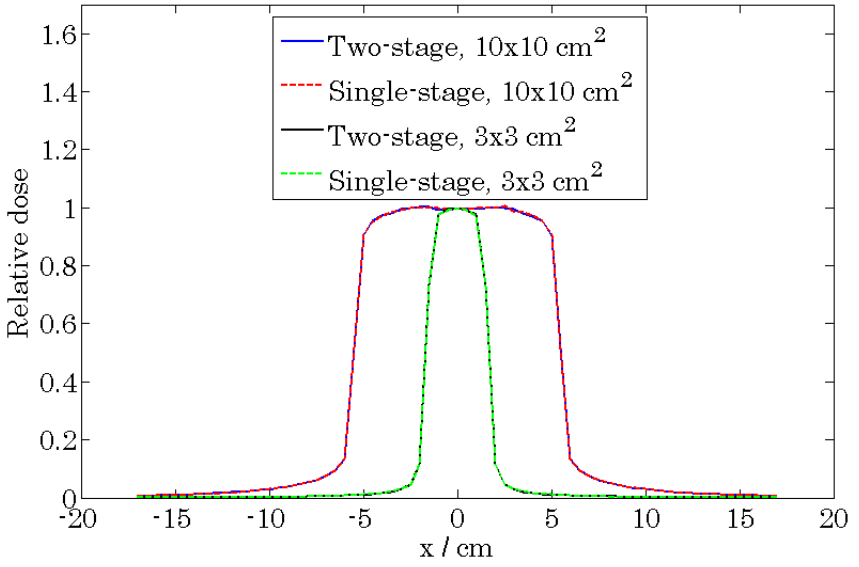

(b)

Figure 5.5: Comparison of simulated (a) PDD and (b) crossline profiles for 3×3 cm^2 and 10×10 cm^2 fields. The two-stage simulations used a phase-space source which was generated in a BEAMnrc simulation that used a phase-space source located above the jaws, which itself was generated in a separate BEAMnrc simulation in which transport of the electron beam through the bremsstrahlung target was modeled with fully retracted jaws and MLC. The single-stage simulations used a phase-space source that was directly generated by a simulation in which transport of the electron beam through the bremsstrahlung target was modeled. Profiles were normalized to the dose at a depth of 10 cm along the beam axis.

5.4.3.1 Beam energy

Previous studies [Jaffray et al., 1993; Sheikh-Bagheri et al., 2000] have measured a Gaussian radial intensity distribution for the electron beam incident on the target, so in this work, the electron beam was modeled with a circular cross section and Gaussian x and y radial intensity distributions. Following the procedure described in Sec. 5.1, the energy of the electron beam was determined first. With a nominal beam energy of 6 MV, electron beam energies of 5.9 MeV, 6.0 MeV, 6.05 MeV, and 6.1 MeV were simulated. For each energy, a phase-space file was tallied above the jaws. Each of the resulting phase-space files was used as a source in a BEAMnrc simulation for a 5×5 cm^2 field defined by the jaws. The 5×5 cm^2 phase-space files were used as sources in DOSXYZnrc simulations of PDD profiles within a $35 \times 35 \times 50$ cm^3 water volume at a SSD of 100 cm. The voxels along the beam axis were $5 \times 5 \times 3$ mm^3, with 3 mm resolution along the beam axis.

PDD profiles were extracted from the simulated dose distributions and compared with the measured PDD profile for a 5×5 cm^2 field from Sec. 5.2. The simulated profiles had a resolution of 3 mm along the beam axis, while the measured profiles were obtained with the A18 ionization chamber, which has a collection volume with a diameter of 5 mm. To account for the difference in the simulated and measured resolution, the simulated profiles were convolved with a 5 mm rectangular function, approximating the volume averaging of the ionization chamber. Agreement between the simulated and measured PDD profiles was evaluated using plots of the residuals beyond a depth of 2 cm. A comparison of the measured and simulated profiles is shown in Fig. 5.6. It is apparent that a beam energy of 5.9 MeV is too low from the downward trend in the plotted residuals, whereas a beam energy of 6.1 MeV is too high based on the upward trend in the plotted residuals. There are no apparent trends in the plotted residuals for beam energies of 6.0 MeV or 6.05 MeV, and agreement between measured and simulated profiles is within $\pm 1\,\%$ for both energies. To distinguish between these two beam energies, phase-space files were tallied at the exit

of the accelerator head for each energy with the jaws set to a 10×10 cm^2 field. The PDD profile simulations were repeated using these phase-space files, and the simulated profiles were compared with the measured 10×10 cm^2 PDD profile. The simulated PDD profile for a beam energy of 6.05 MeV demonstrated better agreement with the measured profile, so this energy was chosen for the beam model.

For each beam energy considered, there was consistent disagreement between the measured and simulated PDD profiles within the buildup region. These discrepancies have been observed in other studies [Sheikh-Bagheri and Rogers, 2002a,b], and have been attributed to inaccurate modeling of the electron contamination within the accelerator head. However, the simulated and measured profiles agree within 1 mm in the high-gradient buildup region.

5.4.3.2 Radial intensity distribution

For a beam energy of 6.05 MeV, phase-space files were tallied at the exit of the accelerator head with the jaws set to a 5×5 cm^2 field for circular Gaussian radial intensity distributions with FWHM of 0.5 mm, 1.0 mm, 1.5 mm, and 2.0 mm. These phase-space files were used as sources in DOSXYZnrc simulations of dose distributions within a $35 \times 35 \times 50$ cm^3 water volume at a SSD of 100 cm. The voxels had a 5 mm thickness along the beam axis. Along the x and y axes, the voxel width was 5 mm within and immediately outside the field, and 1 mm within a distance of 1 cm of the field edge. Profiles along the x and y axes were extracted from the simulated distributions at a depth of 10 cm and compared with the measured crossline and inline profiles, respectively. To account for the volume averaging of the A18 ionization chamber in the measured profiles, the simulated profiles were convolved with a 5 mm rectangular function. Agreement between the measured and simulated profiles was evaluated by determining the root-mean-square difference within 3 mm of the field edge.

Comparisons of the crossline and inline profiles are shown in Figs. 5.7 and 5.8, respectively. The root-mean-square differences between the measured and simulated profiles

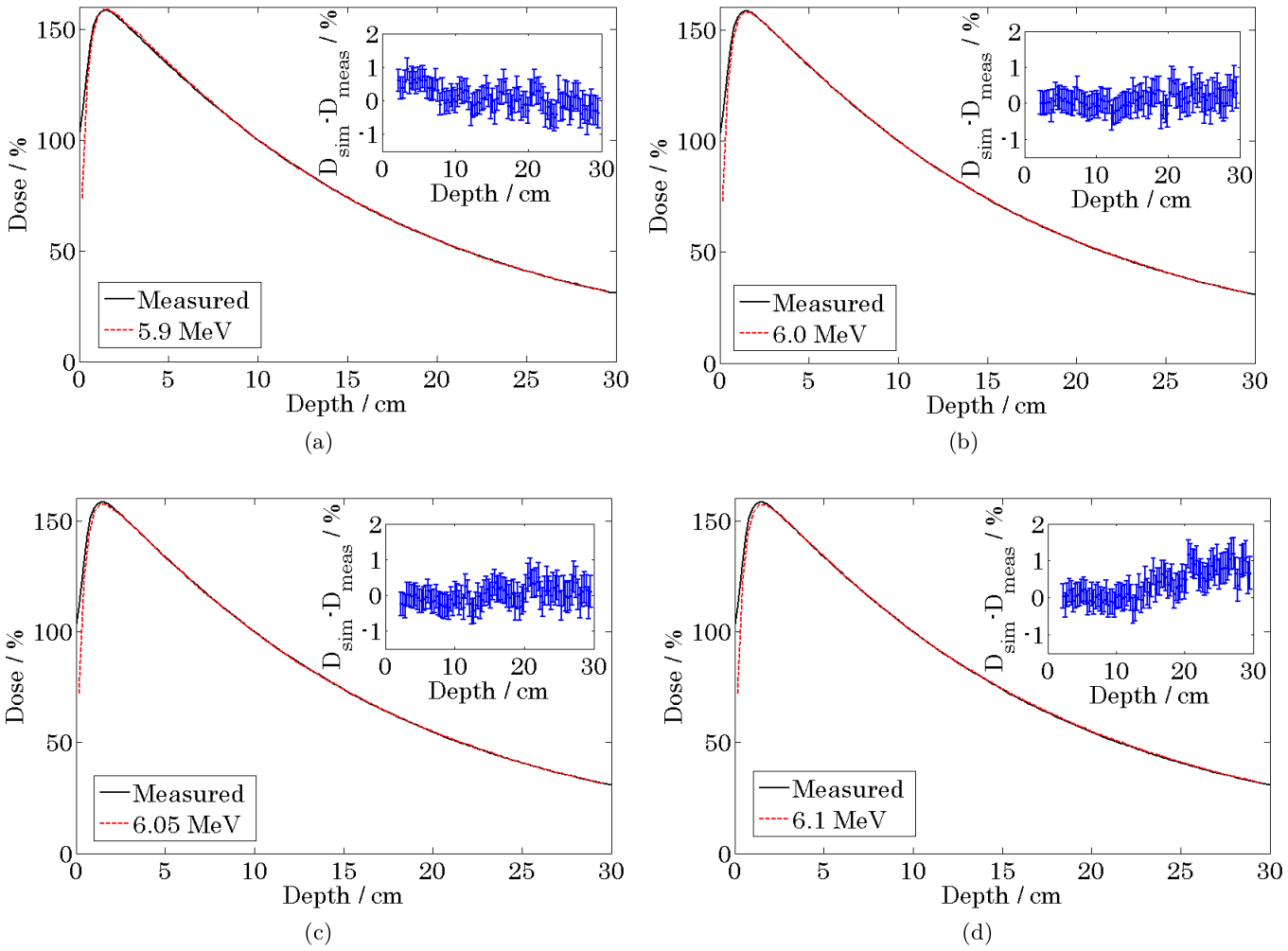

Figure 5.6: Comparison of a measured PDD profile from a 5×5 cm^2 field with simulated PDD profiles for electron beam energies of (a) 5.9 MeV, (b) 6.0 MeV, (c) 6.05 MeV, and (d) 6.1 MeV. Profiles were normalized to the dose at a depth of 10 cm along the beam axis. Figure insets show residuals between simulated and measured data with relative simulation uncertainty of approximately 0.5 % ($k = 1$).

Table 5.1: Root-mean-square differences within the penumbra of measured and simulated crossline and inline profiles for a 5×5 cm^2 field. The simulated profiles were generated for a 6.05 MeV electron beam with a Gaussian intensity distribution with a FWHM of 0.5 mm, 1.0 mm, 1.5 mm, and 2.0 mm.

FWHM (mm)	0.5	1.0	1.5	2.0
Crossline	23.0	18.8	10.4	5.3
Inline	25.4	15.9	6.2	11.8

within 3 mm of the field edge are shown in Table 5.1. For the inline profiles, the best agreement between simulation and measurement was observed for a FWHM of 1.5 mm. Based on the root-mean-square differences, the best agreement between simulation and measurement for the crossline profiles was observed for a FWHM of 2.0 mm. However, the agreement within the shoulder region of these profiles (Fig. 5.7d) is visibly degraded relative to a FWHM of 1.5 mm (Fig. 5.7c). Consequently, a FWHM of 1.5 mm along both the x and y axes was chosen for the Gaussian-distributed electron beam. The determination of a circular radial intensity distribution is consistent with the measurements of Jaffray et al. [1993] for the 6 MV beam from a Varian® linear accelerator.

5.4.3.3 Verification of beam parameters

A comparison of the optimal electron beam parameters determined in this work with those determined in other studies for the 6 MV beam from similar Varian® linear accelerators is shown in Table 5.2. In general, the parameters determined in this work are consistent with those previously determined.

To further verify the optimized electron beam parameters, measured and simulated dose profiles were compared for additional field sizes. Fig. 5.9 shows PDD profiles for a 10×10 cm^2 field, as well as crossline profiles for 2×2 cm^2 and 10×10 cm^2 fields. Overall, the agreement between measured and simulated profiles was within 2 % and 1 mm.

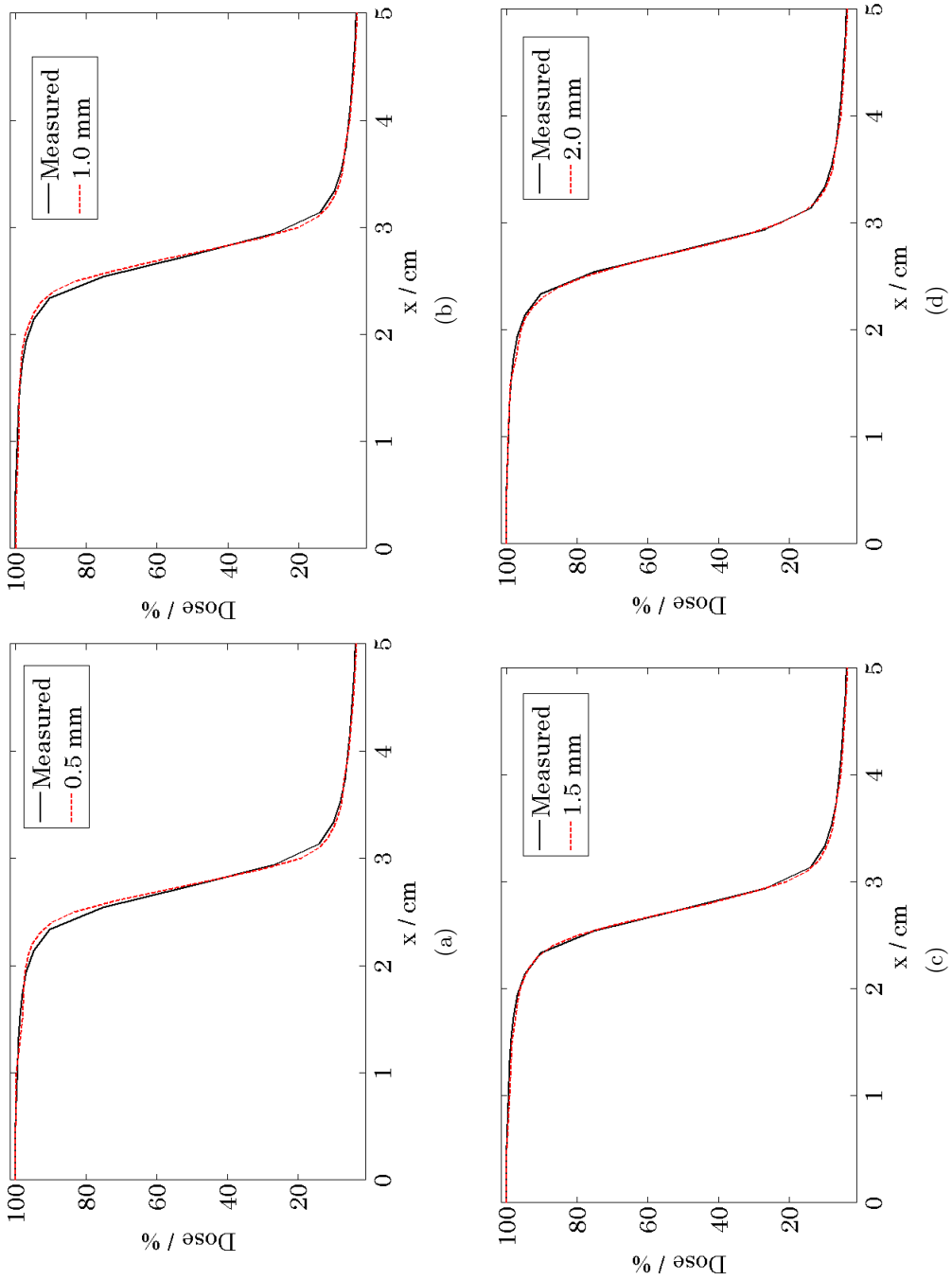

Figure 5.7: Comparison of a measured crossline profile for a 5×5 cm^2 field with simulated crossline profiles for a 6.05 MeV electron beam with a FWHM of (a) 0.5 mm, (b) 1.0 mm, (c) 1.5 mm, and (d) 2.0 mm. Profiles are shown at a depth of 10 cm, normalized to the dose at the center of the field.

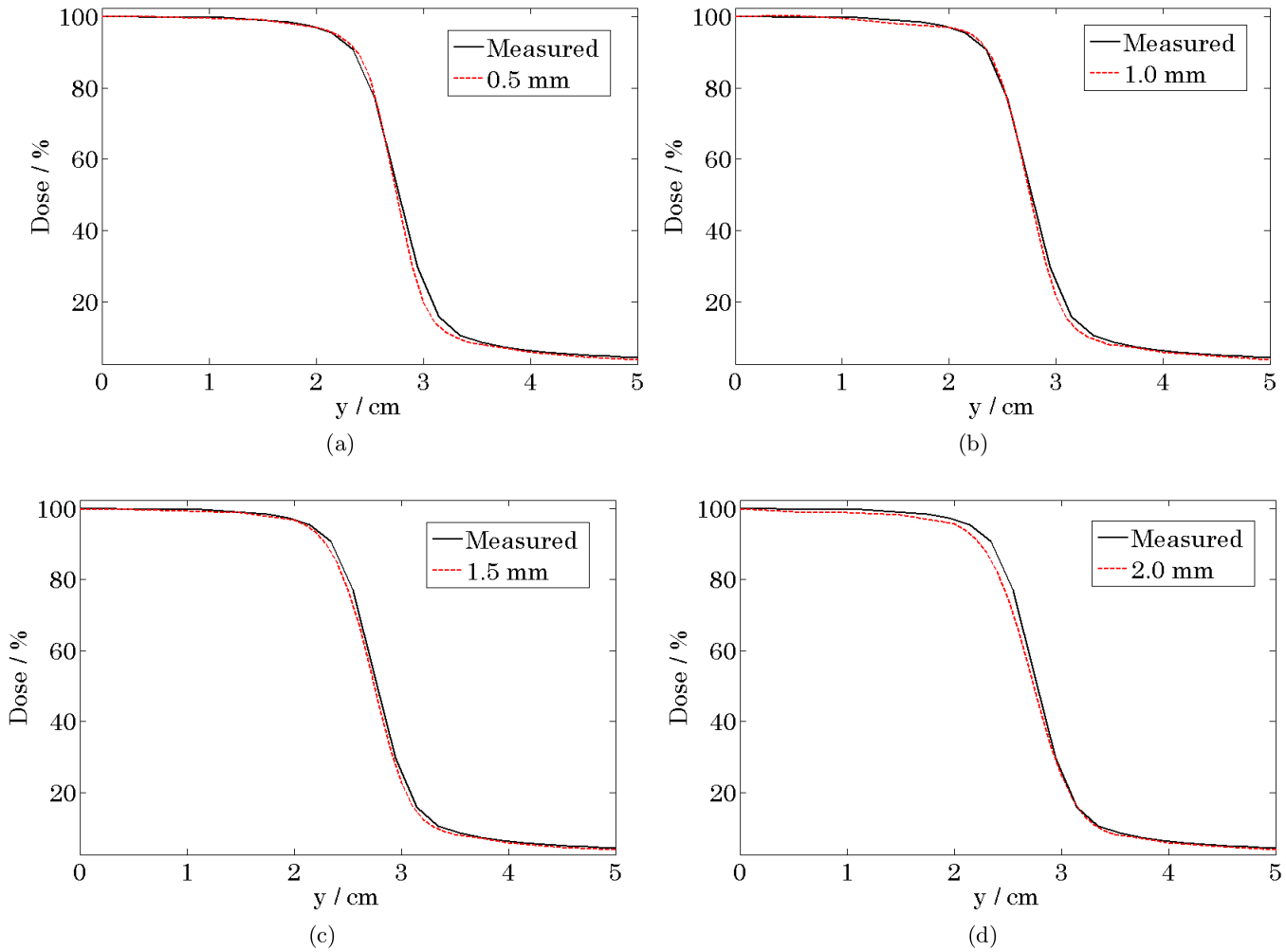

Figure 5.8: Comparison of a measured inline profile for a 5×5 cm^2 field with simulated inline profiles for a 6.05 MeV electron beam with a FWHM of (a) 0.5 mm, (b) 1.0 mm, (c) 1.5 mm, and (d) 2.0 mm. Profiles are shown at a depth of 10 cm, normalized to the dose in the center of the field.

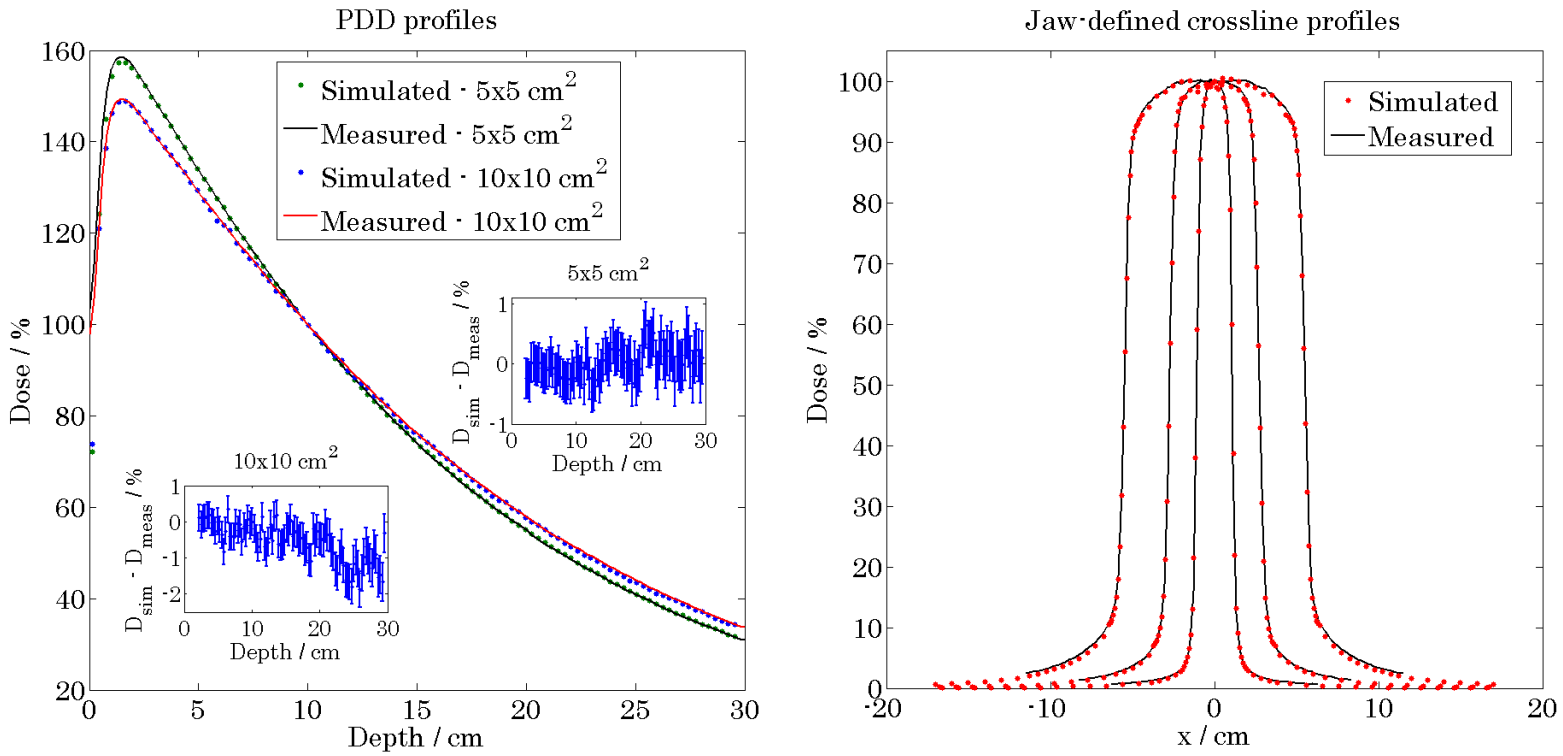

Figure 5.9: Comparison of measured and simulated dose profiles for additional field sizes. (a) Measured and simulated PDD profiles for 5×5 cm^2 and 10×10 cm^2 fields. Residuals are shown, along with relative simulation uncertainty of approximately 0.5 % ($k = 1$). (b) Measured and simulated crossline profiles at a depth of 10 cm for 2×2 cm^2, 5×5 cm^2, and 10×10 cm^2 fields defined by the jaws. Profiles were normalized to the dose at a depth of 10 cm along the central axis.

Table 5.2: Comparison of the optimized electron beam parameters determined in this work with published investigations in which 6 MV fields from similar Varian® accelerators were modeled. Note that the parameters from Sheikh-Bagheri and Rogers [2002b] are the nominal beam parameters as stated by Varian®.

Author	E (MeV)	Energy FWHM (%)	Intensity FWHM (mm)
Sheikh-Bagheri and Rogers, 2002b	6	3	1
Ding, 2002	6.02	17	1.2
Keall et al., 2003	6.2	3	1.3
This work	6.05	0	1.5

5.4.4 Modeling the MLC

The Millennium 120 MLC was modeled using the DYNVMLC component module within BEAMnrc [Heath and Seuntjens, 2003]. This component module models the tongue-and-groove design, rounded leaf tips, and the divergence of the leaves from the source. Additionally, this component module allows for MLC motion, either discrete or continuous, in the simulation of a field. Leaf motion is modeled using the planned leaf positions and the cumulative distribution function (CDF) defining the relative MU delivered for each segment. The CDF is randomly sampled prior to the transport of every source particle to determine the MLC arrangement.

The MLC was modeled according to the specifications provided by Varian®. The provided dimensions were specified at the midplane of the MLC, whereas BEAMnrc models the divergence of the MLC assuming that the input dimensions are specified at the top surface of the MLC. The necessary conversion was made by applying a magnification correction of 1.0706 to all lateral leaf dimensions.

A MATLAB® script was prepared to extract the planned MLC positions from the MLC files generated by the TPS and write them into a file that is referenced during the BEAMnrc simulation. The MLC positions specified by the TPS give the leaf positions based on the light-field projection to the isocenter plane. However, MLC positions in BEAMnrc simulations are specified as the leaf tip position in the MLC midplane, requiring a conversion

of the MLC positions from the TPS. The 4D Integrated Treatment Console computer for Varian® accelerators provides a lookup table that allows for the conversion from the light-field projection to the leaf-tip projection, as well as the magnification correction from the isocenter plane to the MLC midplane [Siebers et al., 2002]. These corrections were applied within the MATLAB® script.

Due to the increased number of MU in IMRT procedures and the use of small MLC apertures, the dose delivered by an IMRT field is highly dependent on both the leakage through the MLC and the accuracy of the leaf positions. Therefore, the consistency of the simulated leakage and leaf positions with those of the actual accelerator was experimentally verified. The MLC leakage for the Clinac® 21EX was measured using an Exradin A12 ionization chamber and a Max 4000 electrometer. The ionization chamber was positioned at a depth of 5 cm within the DoseView3D scanning water tank, which was set up at a SSD of 100 cm. The ionization chamber was oriented perpendicular to the axis of MLC motion, such that the collecting volume spanned the width of multiple leaves. The integrated ionization was measured from the delivery of 1000 MU with the jaws set to a 10×10 cm^2 field and the MLC fully retracted. This measurement was repeated twice: once with each of the MLC leaf banks fully blocking the 10×10 cm^2 field defined by the jaws. Taking the ratio of the mean blocked-field measurement to the open-field measurement, the relative leakage through the MLC was 1.6 %.

These same measurement geometries were simulated using the Monte Carlo model of the Clinac® 21EX. The density of the modeled MLC was adjusted to achieve agreement with the leakage measurement. The simulated MLC leakage as a function of MLC density is shown in Table 5.3. Based on these results, the MLC was assigned a density of 16.4 g/cm^3. This MLC density is lower than the density range of 17 g/cm^3 to 18 g/cm^3 specified by the manufacturer [Arnfield et al., 2000]. However, in this work the MLC was modeled as pure tungsten, whereas the actual MLC is composed of a tungsten alloy containing nickel,

Table 5.3: Simulated leakage through the MLC as a function of the MLC density.

Density (g/cm^3)	Leakage (%)
15.8	1.9
16.0	1.8
16.2	1.7
16.4	1.6

copper, and iron. Within the kilovoltage energy range, where the energy spectrum of a 10×10 cm^2 field peaks (Fig. 4.6), mass-attenuation coefficients for tungsten exceed those for the other elements in the alloy by as much as a factor of ten due to greater photoelectric absorption. To compensate for the greater attenuation through elemental tungsten relative to the tungsten alloy, the density of tungsten must be correspondingly reduced below that of the alloy.

To verify consistency of the simulated and actual leaf positions, the output from a series of sliding window fields was measured. The experimental setup was identical to that used for the measurements of MLC leakage. A series of SW-IMRT fields were defined in which the leaves were initially closed, then opened to a given window width which swept across a 10×10 cm^2 field before closing on the opposite side of the field. Measurements were completed for window widths of 0.5 cm, 1 cm, 2 cm, and 10 cm. These measurement geometries were again simulated using the Monte Carlo model of the Clinac® 21EX. The measured and simulated output for each window width normalized to the output for a 10×10 cm^2 field defined by the jaws are shown in Table 5.4. The simulated output is consistently higher than measured, and as the width of the window decreases, the difference increases. These results are consistent with a systematic offset between simulated and measured leaf positions. For smaller window widths, the relative positioning error is greater, so the error in the simulated output is correspondingly greater. Based on the results of Siebers et al. [2002], an offset of -0.08 mm was applied to the simulated leaf positions

defined in the midplane of the MLC. With the application of this offset, the measured and simulated output agree within 1 %.

For verification of the completed Millennium 120 MLC model, inline and crossline profiles were simulated for 2×2 cm^2, 3×3 cm^2, 4×4 cm^2, and 5×5 cm^2 fields defined by the MLC and compared with measured profiles. The resulting profiles are shown in Fig. 5.10, along with a comparison of simulated and measured profiles through a MLC arrangement that alternated two leaves open, one leaf closed. As with the profile comparisons for fields defined by the jaws, overall agreement is within 2 % and 1 mm. In particular, there is good agreement in the tails of the profiles, which are most sensitive to the MLC density.

5.5 Conclusions

A Monte Carlo model of the 6 MV beam from a Clinac® 21EX linear accelerator was developed using EGSnrc. The physical components within the head of the accelerator were modeled according to manufacturer specifications. The energy and radial intensity distribution of the electron beam incident on the bremsstrahlung target were adjusted to achieve agreement between measured and simulated PDD, inline, and crossline profiles. After optimizing the electron beam parameters, the model of the Millennium 120 MLC was verified, adjusting the leaf density to match measured and simulated leakage. Overall, the measured and simulated profiles agreed within 2 % and 1 mm.

Table 5.4: Simulated and measured output from 10×10 cm^2 fields swept by the MLC with varying leaf separations. An offset of -0.08 mm was applied to the leaf positions in the MLC midplane to improve agreement with measurement (see columns 5 and 6). Output is normalized to that for a 10×10 cm^2 field defined by the jaws.

Window width (cm)	Measured output	Simulated output	Difference (%)	Simulated output with leaf offset	Difference (%)
0.5	0.0791	0.0827	4.6	0.0794	0.38
1	0.1178	0.1210	2.7	0.1184	0.51
2	0.1742	0.1761	1.1	0.1754	0.69
10	0.5058	0.5075	0.34	0.5074	0.32

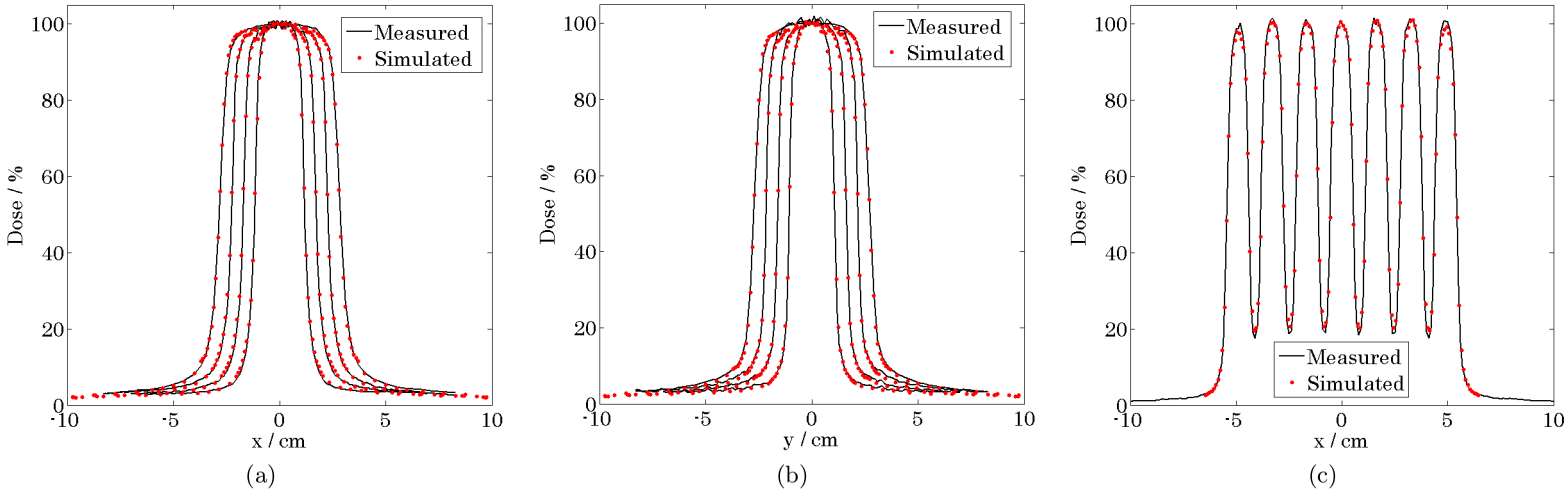

Figure 5.10: Comparison of measured and simulated profiles for fields defined by the MLC. (a) Crossline and (b) inline profiles are shown for 2×2 cm^2, 3×3 cm^2, 4×4 cm^2, and 5×5 cm^2 fields. (c) Measured and simulated profiles through a MLC arrangement that alternated two leaves open, one leaf closed. Profiles are shown at a depth of 10 cm and normalized to the dose in the center of the field.

Chapter 6

Experimental and computational investigation of the interplay effect

6.1 Experimental verification of interplay simulation methodology

In this chapter, the investigation of treatment delivery errors due to interplay between target motion and intensity modulation is discussed. The Monte Carlo accelerator model developed in Ch. 5 was used to simulate interplay errors. The experimental verification of the interplay simulation methodology is covered in this section. Two treatment plans were prepared for this investigation. The delivery of the treatment plans with the Clinac® 21EX accelerator was measured with the film stack dosimeter undergoing modeled respiratory motion. The delivered dose was then reconstructed using the Monte Carlo accelerator model for comparison with the measurements.

6.1.1 Treatment plan preparation

Two seven-field SS-IMRT treatment plans, one conventionally fractionated and one hypofractionated, were prepared for anonymized clinical CT datasets using the Eclipse v10 TPS. The Eclipse TPS was chosen because it has a built-in structure for the Exact® image-guided radiation therapy (IGRT) treatment couch, allowing for consideration of the attenuation through the couch during the plan optimization and dose calculation. Both plans were prepared using the 6 MV beam energy.

Of the two CT datasets, one had a tumor located in the lower lobe of the right lung, while the other had a tumor in the upper lobe of the right lung. Within the contoured CTV of each dataset, a contour was created with the outer dimensions of the film stack dosimeter housing. This volume was assigned a unit density, and was defined as the CTV for each treatment plan. The Boolean difference between the existing CTV contour and the film stack dosimeter contour, which gave the volume within the existing CTV but outside the film stack dosimeter, was assigned a representative lung tissue density of 0.3 g/cm^3. The residual lung was contoured as the Boolean difference between the total lungs and the film stack dosimeter contour, following the RTOG 0915 recommendation that this volume be defined as the difference between the total lungs and the CTV.

A conventionally fractionated treatment plan with coplanar fields was prepared for the CT dataset with the lower-lobe target location. ITV expansion margins of 1 mm along the left-right axis, 1 mm along the anterior-posterior axis, and 7 mm along the superior-inferior axis were used, based on the mean motion amplitude of lung tumors located in the lower lobe measured by Seppenwoolde et al. [2002]. A uniform PTV expansion margin of 5 mm was used [Ehler and Tomé, 2009]. A dose of 70 Gy delivered over 35 fractions was prescribed to cover 98 % of the PTV. Published dose-volume constraints for critical organs in conventionally fractionated treatments were used [Emami et al., 1991; Spalding et al.,

2007; Marks et al., 2010b]. Mean-dose constraints were not used in this work because the Eclipse TPS only permits the use of such constraints for VMAT optimization.

A hypofractionated treatment plan with non-coplanar fields was prepared for the CT dataset with the upper-lobe target location. ITV expansion margins of 1 mm along the left-right axis, 2 mm along the anterior-posterior axis, and 3 mm along the superior-inferior axis were used, based on the mean motion amplitude of lung tumors located in the middle and upper lobes measured by Seppenwoolde et al. [2002]. RTOG 0915 recommends the use of a uniform 5 mm PTV expansion margin if a 4DCT is used to measure the motion of the target. As will be discussed in Sec. 6.1.3, target motion waveforms were prepared using a parameterization of respiratory motion; therefore, the target motion was precisely known. Consequently, a uniform 5 mm PTV expansion margin was used. Following the RTOG 0915 protocol, a dose of 48 Gy delivered over four fractions was prescribed to cover 95 % of the PTV. Dose-volume constraints for critical organs were also obtained from this protocol.

For both treatment plans, the dose volume optimizer (DVO) optimization algorithm and the analytic anisotropic algorithm (AAA) dose calculation algorithm [Ulmer et al., 2005] were used. Heterogeneity corrections were applied during the dose calculation. Default priorities for fluence smoothing were used. The optimized fluence was converted to the delivered fluence using the leaf motion calculator (LMC). The LMC was set to bin the fluence distribution into ten intensity levels. Each field delivered an equal dose to the isocenter, and all segments within a field delivered an equal number of MU.

All critical-organ dose constraints were satisfied for the conventionally fractionated plan. The maximum dose within the PTV was 113 % of the prescription dose. The hypofractionated treatment plan had multiple minor deviations from compliance with the conformality dose constraints, but there were no major deviations as defined in the RTOG 0915 protocol.

6.1.2 Experimental geometry

The delivery of the two treatment plans was measured using the film stack dosimeter in the experimental geometry shown in Fig. 6.1. The film stack dosimeter was mounted on the end of a motion stage attached to the 4D motion phantom (Washington University in St. Louis, St. Louis, MO) [Malinowski et al., 2007] at a SAD of 100 cm. The 4D phantom is capable of fully programmable, independently controlled motion along four separate axes. Three linear motion actuators are orthogonally mounted to each other to provide 3D motion. A fourth linear motion actuator is separately mounted, aligned with the anterior-posterior axis to model surrogate (i.e., chest wall) motion. Custom motion trajectories can be executed at 50 Hz with a positioning accuracy of ± 0.2 mm. The 4D phantom was positioned such that the motion axes aligned with the positioning lasers in the treatment vault. No visible deviation was observed in the alignment along the motion axis over a motion path of ± 5 cm. The motion phantom was clamped to the treatment couch to prevent migration during the execution of programmed motion. The positioning of the 4D phantom was verified after each measurement. The LUNGMAN™ anthropomorphic thorax phantom (Kyoto Kagaku, Inc., Kyoto, Japan) was positioned to approximately locate the film stack dosimeter within the diseased lobe from the respective treatment plan. The coordinates of the treatment couch were recorded, and the positions of the lasers on the phantoms were marked to facilitate positioning reproducibility.

In order to simulate dose distributions delivered to the experimental geometry, a CT scan was taken of the setup using a Discovery™ Lightspeed® CT simulator (GE Healthcare, Waukesha, WI). The locations of the positioning lasers were marked with lead BBs to facilitate the placement of the treatment isocenter in the resulting dataset. The film stack dosimeter was scanned with an empty cavity to allow for straightforward identification in the image. A helical scan was taken of the experimental geometry with a field of view of

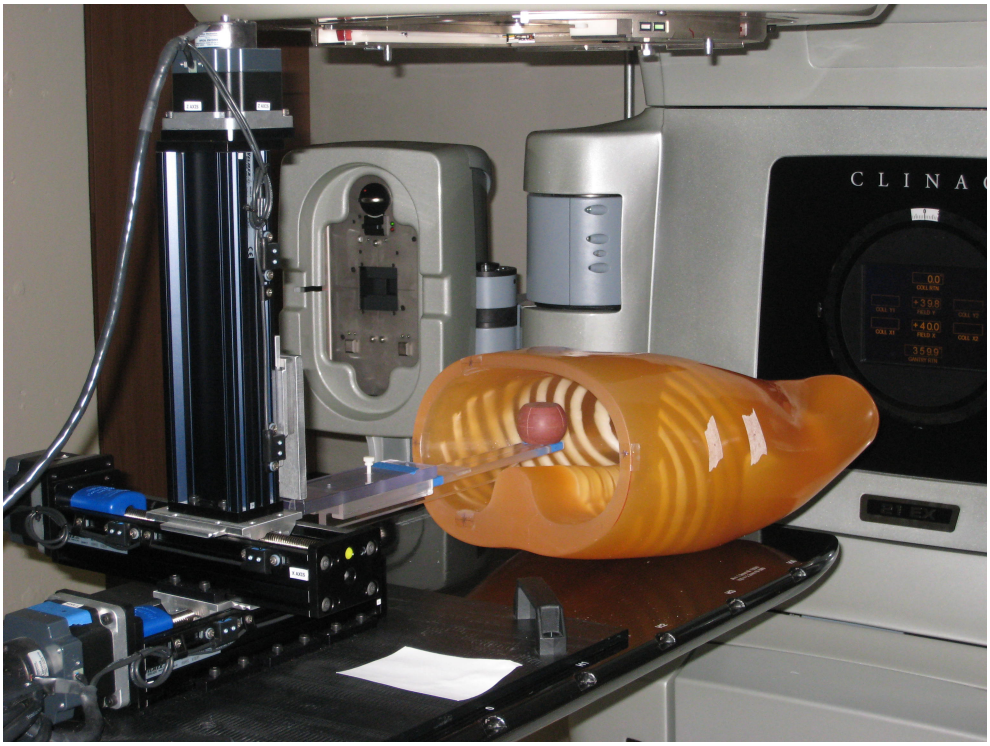

Figure 6.1: Experimental setup for the measurements of the treatment plans with the film stack dosimeter. The dosimeter was mounted at the end of a motion stage attached to the 4D motion phantom and positioned at a SAD of 100 cm. The LUNGMAN™ phantom was positioned to locate the dosimeter at the approximate disease site for the delivered treatment plan.

50 cm and the standard reconstruction technique. The scan used a tube voltage of 120 kV and a tube current of 320 mA with a slice thickness of 1.25 mm.

6.1.3 Measurement of interplay errors

6.1.3.1 Preparation of respiratory motion waveforms

The interplay simulation methodology was verified by measuring the delivery of the treatment plans prepared in Sec. 6.1.1 with the film stack dosimeter as it followed a programmed motion waveform, then reconstructing the measurements with Monte Carlo simulations for comparison. The greater the dependence of the measured dose distribution on the period and initial phase of the motion waveform (i.e., the greater the magnitude of interplay errors), the more sensitive the experimental verification is to inaccuracies in the simulated reconstruction of the treatment delivery.

For the experimental verification, both one-dimensional and three-dimensional motion waveforms were used. One-dimensional sinusoidal waveforms along the superior-inferior axis were used for simplicity; motion parameters were selected to maximize interplay errors. Simulations of interplay errors were completed for a limited range of motion periods using the procedure described in Sec. 6.1.5 to identify waveform parameters that resulted in the greatest delivery errors. Based on the investigations of interplay errors in tomotherapy treatments discussed in Ch. 2 [Kissick et al., 2008; Chaudhari et al., 2009; Tudor et al., 2014], it was expected that the greatest delivery errors would result from interference of target motion with low-frequency intensity modulation. In SS-IMRT there are three primary timescales for intensity modulation: delivery of a single segment (approximately 1 s), delivery of a single field (approximately 10 s), and delivery of successive fields (approximately 60 s). These timescales are dependent on multiple factors, including the dose per fraction, the dose rate and the complexity of the treatment plan, but these approximate timescales are representative of the relative order of magnitude of each. To sample the range of timescales

for low-frequency intensity modulation, interplay errors were simulated for motion periods of 15, 20, 30, 40, and 60 s. Four uniformly spaced initial phases of motion were simulated for each motion period. Relatively large motion amplitudes of 20 mm and 10 mm were chosen for the IMRT and SBRT plans, respectively, to further maximize potential delivery errors. As will be discussed in Sec. 6.1.5, interplay errors were quantified by reference to the simulated expected blurred dose distribution, in which the spatial fluence modulation of the treatments was simulated without temporal modulation, thereby preventing the occurrence of interplay errors. The greatest delivery errors occurred for motion periods of 30 s and 40 s for the IMRT and SBRT plans, respectively.

The three-dimensional motion waveforms used for the experimental verification were chosen to more realistically represent respiratory motion. These waveforms were generated using Eq. 6.1, which was adapted from Kissick et al. [2008],

$$\boldsymbol{r}(t) = \boldsymbol{r}_0(t) + \boldsymbol{b}(t)\cos^{2n}[\frac{\pi t}{\tau(t)} + \boldsymbol{\phi}], \tag{6.1}$$

where $\boldsymbol{\phi}$ is the initial phase of the motion and n dictates the asymmetry of the waveform. Based on the results of George et al. [2005], a value of $n = 1$ was used to model respiratory motion. The time-dependent parameters of Eq. 6.1 were defined as shown in Eqs. 6.2-6.4,

$$\boldsymbol{r}_0(t) = \boldsymbol{\mu}_{\boldsymbol{r}_0} + \delta\boldsymbol{r}_0(t), \tag{6.2}$$

$$\boldsymbol{b}(t) = \boldsymbol{\mu}_{\boldsymbol{b}} + \delta\boldsymbol{b}(t), \tag{6.3}$$

$$\tau(t) = \mu_\tau + \delta\tau(t), \tag{6.4}$$

where $\boldsymbol{\mu}_{\boldsymbol{r}_0}$, $\boldsymbol{\mu}_{\boldsymbol{b}}$, and $\boldsymbol{\mu}_\tau$ are the mean baseline offset, mean motion amplitude, and mean motion period, respectively. The mean motion parameters were determined based on the results of Seppenwoolde et al. [2002]. The mean motion period and amplitude were de-

termined using the mean results reported for the tumor locations corresponding to those used for the treatment plans in this thesis work, while the mean baseline offset was set to zero. The parameters $\delta \boldsymbol{r}_0(t)$, $\delta \boldsymbol{b}(t)$, and $\delta\tau(t)$ were each randomly sampled from a standard normal distribution and scaled by the standard deviations in the exhale position, amplitude, and period, respectively, reported by Seppenwoolde et al. [2002]. The motion parameters used to develop the one-dimensional and three-dimensional motion waveforms for each of the treatment plans are summarized in Table 6.1.

The three-dimensional waveforms were constructed cycle-by-cycle. At the start of each cycle, the parameters $\delta \boldsymbol{r}_0(t)$, $\delta \boldsymbol{b}(t)$, and $\delta\tau(t)$ were determined. A single randomly sampled value per cycle was used to determine the motion amplitude variation along all three motion axes. At transitions between cycles, the change in position was constrained to be less than 0.1 mm, and the sign of the motion velocity was preserved. The motion period was assumed to be equal for motion in all three dimensions. Motion along the lateral and superior-inferior axes was in-phase, while motion along the anterior-posterior axis led these axes by $\frac{\pi}{4}$ [Seppenwoolde et al., 2002]. Sample waveforms using motion parameters for the upper lobe target location are shown in Fig. 6.2.

6.1.3.2 Film stack dosimeter measurements

The delivery of each of the treatment plans prepared in Sec. 6.1.1 with the Clinac® 21EX was measured using the film stack dosimeter. To verify simulations of the treatment plans using the Monte Carlo model developed in Ch. 5, each treatment plan was first measured using the film stack dosimeter positioned within the cylindrical phantom housing at a SAD of 100 cm. In the absence of detector motion and the LUNGMAN™ phantom, differences between simulated and measured distributions due to positioning or geometry modeling errors were minimized, thereby isolating errors due to the beam model. For the SBRT

Table 6.1: Summary of parameters used to generate the one-dimensional (1D) and three-dimensional (3D) motion waveforms for the measurements of the IMRT and SBRT treatment plans. The subscripts LR, AP, and SI denote motion along the lateral, anterior-posterior, and superior-inferior axes, respectively. μ_x and σ_x are the mean and standard deviation of parameter x, respectively. τ, b, and r_0 are the motion period, amplitude, and baseline offset, respectively. Parameters were determined using the results of Seppenwoolde et al. [2002].

		μ_τ (s)	σ_τ (s)	$\mu_{b_{\mathrm{LR}}}$ (mm)	$\mu_{b_{\mathrm{AP}}}$ (mm)	$\mu_{b_{\mathrm{SI}}}$ (mm)	$\sigma_{b_{\mathrm{LR}}}$ (mm)	$\sigma_{b_{\mathrm{AP}}}$ (mm)	$\sigma_{b_{\mathrm{SI}}}$ (mm)	$\sigma_{r_{0,\mathrm{LR}}}$ (mm)	$\sigma_{r_{0,\mathrm{AP}}}$ (mm)	$\sigma_{r_{0,\mathrm{SI}}}$ (mm)
IMRT	1D	30	0	0	0	20	0	0	0	0	0	0
	3D	4.1	0.60	1.5	1.9	12	0.35	0.36	1.7	0.20	0.30	0.40
SBRT	1D	40	0	0	0	10	0	0	0	0	0	0
	3D	3.3	0.40	1.4	2.9	5.0	0.20	0.30	0.60	0.20	0.30	0.40

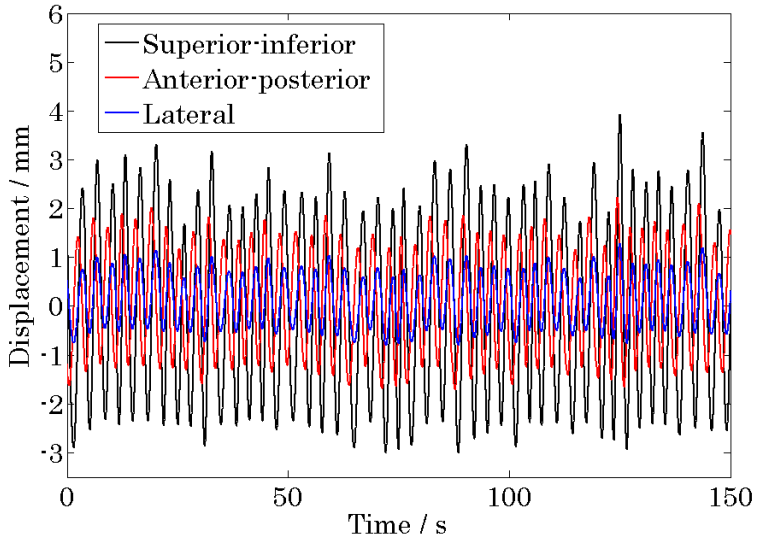

Figure 6.2: Sample motion waveforms for an upper lobe target location prepared using Eq. 6.1.

plan, the delivered MU were reduced by a factor of six to maintain an approximate dose to isocenter of 2 Gy.

Measurements of each treatment plan were then taken using the film stack dosimeter in the geometry described in Sec. 6.1.2. Measurements were taken for a static geometry, as well as with the film stack dosimeter following the one-dimensional and three-dimensional waveforms developed in Sec. 6.1.3.1. For the measurements with a moving detector, the treatment delivery was initiated at an arbitrary time after the start of the motion. In order to accurately reconstruct the treatment deliveries with Monte Carlo simulations for the verification of the interplay simulation methodology, the target position during the delivery of each MLC segment must be known. Given the programmed motion waveform for the 4D motion phantom and the planned MLC sequences from the TPS, it is only necessary to know the time at which each segment was delivered relative to the start of the programmed motion.

The 4D motion phantom uses a separate IM805 microstepping driver (Schneider Electric Motion, Marlborough, CT) for each motion axis. These drivers have a step-clock input which triggers motion along the corresponding motion axis. To monitor the execution of the programmed motion waveform, a connection was soldered to the step-clock input for the x axis, which was the most accessible, and fed through the amplifier encasing. The motion trigger pulses were measured to be approximately 15 μs wide. The Clinac® 21EX linear accelerator has a target current output from which beam pulses are indicated with square wave pulses. These pulses were measured to be approximately 3.5 μs wide with a separation of approximately 3 ms when operated at a dose rate of 600 MU/min. Measurement of both the 4D phantom step-clock input and the accelerator target current output on the same time axis provides the necessary information for the simulated reconstruction of the measurements.

Based on the measured pulse width of the accelerator target current output and the estimated delivery time for the two treatment plans, a sampling frequency of approximately 1 MHz over 10 min to 15 min was required, totaling nearly one billion samples. A Salae Logic logic analyzer (San Francisco, CA) was used to measure the 4D phantom step-clock input and the accelerator target current output. Use of the logic analyzer required the conversion of these analog signals to digital signals, which was accomplished using comparators. Although not required given the sampling frequencies achieveable with the Logic, monostables were also prepared for each of the trigger signals to broaden the digital signals and permit collection at a lower sampling frequency. The accelerator target current output pulses were stretched to approximately 2 ms, which introduces some uncertainty into the determination of the start and end times for the delivery of each segment. However, even for a motion waveform with a 1 s period, this amounts to a positioning uncertainty of just 0.5 % of the motion amplitude.

Since only the trigger signal from the x axis of the 4D phantom was available, a half-cycle of motion along the x axis was programmed at the start of each one-dimensional waveform to mark the start of the motion. This motion was sufficiently brief to finish prior to the delivery of the treatment plan. To summarize the measurement procedure for treatment deliveries with a moving detector, the data collection with the Logic was first initiated. The 4D phantom was then set in motion. An arbitrary time later, the treatment delivery was started. A 4 MHz sampling frequency was used with the Logic, permitting data collection for more than 40 min.

6.1.4 Modeling the treatment couch

The UWMRRC Clinac® 21EX accelerator has the Exact® IGRT treatment couch, which is comprised of a foam core surrounded by a carbon fiber skin. The attenuation of radiation through this treatment couch is approximately 2 % for posterior incidence, with a maximum of nearly 5 % attenuation for oblique incidence [Seppälä and Kulmala, 2011; Li et al., 2011]. For comparison with the film stack dosimeter measurements, the simulated treatment reconstructions must account for the attenuation through the treatment couch, which requires a Monte Carlo model of the couch.

A CT dataset of the Exact® IGRT couch, which could be used with the CTCREATE script in DOSXYZnrc to prepare a Monte Carlo model, was located on the MedPhys Files website hosted by Mobius Medical Systems (Houston, TX). The methodology of Teke et al. [2011], which developed a Monte Carlo model of the Exact® IGRT treatment couch using the structure set from the Eclipse TPS, was adapted to generate a model from the CT image. Without the IVDT for the CT scanner used to create the dataset, the densities of the foam and carbon fiber were assumed to be uniform throughout the respective materials. The atomic composition of the foam material provided by Teke et al. [2011] was used, and

the carbon fiber was modeled as graphite. The density of the carbon fiber was varied to match the measured attenuation through the couch as a function of gantry angle.

The attenuation through the treatment couch was measured with an Exradin A1SL ionization chamber at depth within the cylindrical phantom housing. The phantom was positioned at a SAD of 100 cm and centered longitudinally between the two indexed Lok-Bar (CIVCO Medical Solutions, Coralville, IA) positions nearest to the gantry. Measurements were taken for gantry angles between 90° and 270° in 30° increments, where 180° is posterior incidence and 90° and 270° are patient left and right, respectively. Thirty-second charge readings were taken of exposures with a 10×10 cm^2 field. Measurements at each angle were normalized to the mean of the measurements at gantry angles of 90° and 270°.

For the corresponding simulation of the attenuation through the couch, the CT dataset of the couch was inserted into the virtual CT dataset of the cylindrical phantom housing using MATLAB®. The couch data were interpolated to match the resolution of the phantom data. A Monte Carlo phantom of the merged CT dataset was generated using the CTCREATE script; however, the script did not function properly, and the Monte Carlo phantom was not correctly generated. Rather than troubleshoot the existing script, a MATLAB® script was prepared with the desired functionality of CTCREATE. This script was verified by comparing PDD profiles simulated within a rectangular water volume defined using the standard rectilinear method in DOSXYZnrc and also using the MATLAB® script to convert a virtual CT dataset of an equivalent water volume to a Monte Carlo phantom. The resulting profiles were consistent within the simulation uncertainty of 0.5 % ($k = 1$). This script was then used to generate a Monte Carlo phantom from the merged CT dataset of the treatment couch and the cylindrical phantom housing. The attenuation through the couch for a 10×10 cm^2 field was simulated for the same gantry angles at which measurements were completed. Simulations were completed for carbon fiber densities ranging from 1.0 g/cm^3 to 1.3 g/cm^3. The simulations had a statistical uncertainty of 0.8 % ($k = 1$). Percentage

Table 6.2: Percentage differences in the simulated transmission through the treatment couch relative to the measured transmission. Results are shown for different simulated densities of the carbon fiber in the treatment couch. Transmission was quantified as the dose measured at depth within the cylindrical phantom for a given gantry angle relative to the mean dose for gantry angles of 90° and 270°, for which the beam does not pass through the couch.

Gantry angle (degrees)	1.0 g/cm^3	1.1 g/cm^3	1.2 g/cm^3	1.3 g/cm^3
90	-0.38	0.23	0.63	-0.08
120	-1.6	-0.93	-1.9	-1.2
150	-0.81	-1.1	-0.23	0.39
180	-0.99	-0.36	-1.1	-1.0
210	-0.14	0.04	-0.79	-0.21
240	0.47	0.69	0.21	1.3
270	0.38	-0.23	-0.63	0.08

differences in the simulated and measured transmission through the treatment couch are shown in Table 6.2. In general, there is no apparent trend in the attenuation through the couch as a function of carbon fiber density. The uncertainty in the simulations is evident in the results for gantry angles of 90° and 270°, which should be independent of carbon fiber density, but vary by as much as 1 %. A carbon fiber density of 1.1 g/cm^3 was chosen because it resulted in the best agreement with the measured attenuation.

6.1.5 Simulated reconstruction of interplay measurements

6.1.5.1 Simulation of static measurements

For the simulation of the treatment plan measurements within the cylindrical phantom housing, the Monte Carlo phantom developed during the modeling of the treatment couch was used. Separate BEAMnrc simulations were completed to generate phase-space files for the delivery of each field of each treatment plan. The dose distribution within the cylindrical phantom housing was then simulated for the individual delivery of each field. The resulting distributions were weighted by the planned number of MU per field and summed to reconstruct the delivered dose.

As will be discussed in the next section, the simulation of the measurements with a moving dosimeter required the individual simulation of the delivery of each segment. To verify the consistency of the segment-by-segment simulation with the field-by-field simulation, the dose delivered from each segment to the cylindrical phantom housing was individually simulated. The resulting dose distributions were weighted by the planned number of MU per segment and summed to reconstruct the composite dose distribution. For the field-by-field simulations, 5×10^8 histories were completed per simulation, and for the segment-by-segment simulations, 5×10^7 histories were completed per simulation, resulting in approximately the same total number of histories for each composite dose distribution. The relative difference between the two resulting composite dose distributions, normalized to the field-by-field simulations, was determined. The relative dose-difference histograms considering the voxels corresponding to the film stack dosimeter volume are shown in Fig. 6.3 for the IMRT and SBRT treatment plans. Fitting a normal distribution to each histogram, the relative dose-difference distribution for the IMRT plan has a standard deviation of 1 %, while that for the SBRT plan has a standard deviation of 0.8 %. The mean difference between the two simulation techniques was zero for both treatment plans, verifying the consistency of the field-by-field and segment-by-segment simulations. Furthermore, since these simulations for a given treatment plan should only differ by the simulation uncertainty, the standard deviations of the resulting relative dose-difference distributions provide estimates for the uncertainty in the simulations of the composite dose distributions.

To investigate the impact of the presence of the treatment couch on the simulated dose distribution, the composite dose from the IMRT plan was simulated to the cylindrical phantom housing in the absence of the treatment couch. The relative dose-difference histogram comparing the voxels within the film stack dosimeter volume for composite distributions simulated with and without the treatment couch is shown in Fig. 6.4. Dose differences were normalized to the dose distribution simulated with the treatment couch. Fitting a normal

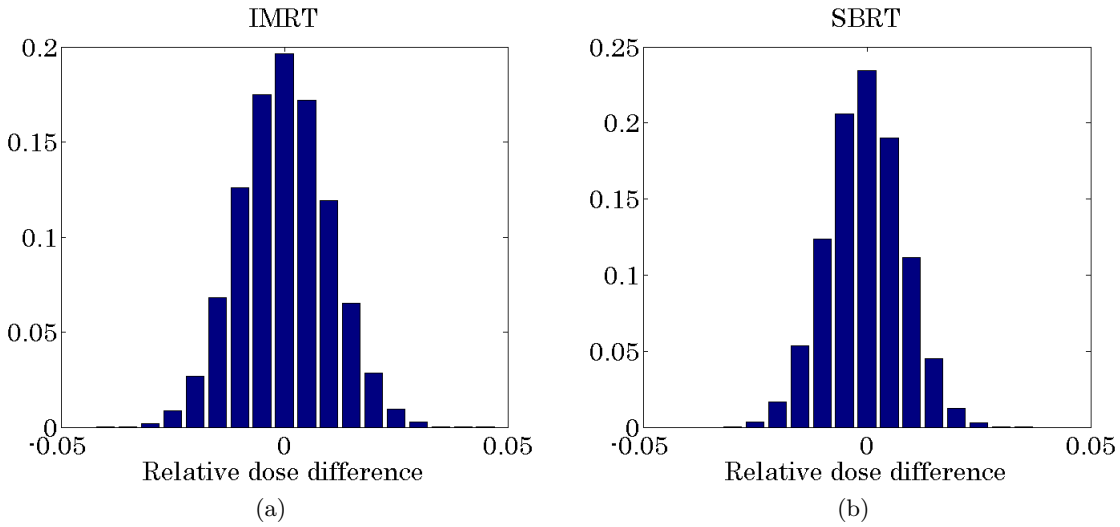

Figure 6.3: Relative dose-difference histograms comparing the composite dose delivered to the cylindrical phantom housing by the (a) IMRT and (b) SBRT treatment plans simulated using field-by-field and segment-by-segment approaches. Differences were normalized to the field-by-field simulations.

distribution to the relative dose-difference histogram, differences between the dose distributions with and without the treatment couch have a standard deviation of 0.9 %, which is within the estimated simulation uncertainty. Therefore, the presence of the treatment couch does not significantly impact the simulated dose to the film stack dosimeter, and the treatment couch was excluded from further simulations.

To investigate the impact of the MLC positioning offset determined in Sec. 5.4.4, the composite dose distribution delivered to the cylindrical phantom housing by each treatment plan was simulated with an offset of -0.08 mm applied to the planned positions of the MLC leaves. Relative dose-difference histograms comparing the composite distributions simulated with and without the application of the offset to the MLC positions are shown in Fig. 6.5. Dose differences were normalized to the dose distribution simulated without the MLC offset. With the MLC offset applied, the simulated dose shifts lower. To determine the significance of this change in simulated dose, a normal distribution was fit to each relative dose-difference

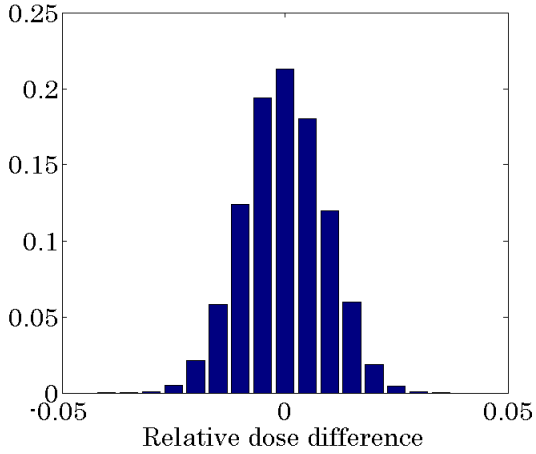

Figure 6.4: Relative dose-difference histogram comparing the composite dose delivered to the cylindrical phantom housing with and without the inclusion of the treatment couch in the simulations. Dose differences were normalized to the dose distribution simulated with the treatment couch.

histogram. The mean differences in the simulated distributions with and without the MLC offset for the IMRT and SBRT plans were -0.2 % and -0.5 %, respectively. Furthermore, the relative dose-difference distributions for the IMRT and SBRT plans had standard deviations of 0.96 % and 1.3 %, respectively. For the IMRT plan, differences between the distributions with and without the MLC offset were within the simulation uncertainty. However, for the SBRT plan, the differences between the distributions exceeded the simulation uncertainty ($k = 1$). The greater significance of the MLC offset for the SBRT plan is reasonable, given the greater proportion of smaller segment openings, which were most impacted by the MLC offset. Therefore, the MLC offset was not applied in simulations of the IMRT plan, but simulations with and without the MLC offset were completed of the SBRT plan for comparison with the film stack dosimeter measurements.

A Monte Carlo model of the LUNGMAN™ phantom was prepared using the MATLAB® script with CTCREATE functionality. Based on the negligible impact of the treatment couch on the simulated dose within the film stack dosimeter volume, the couch was excluded from the Monte Carlo model. The tissue analogs of the LUNGMAN™ phantom were

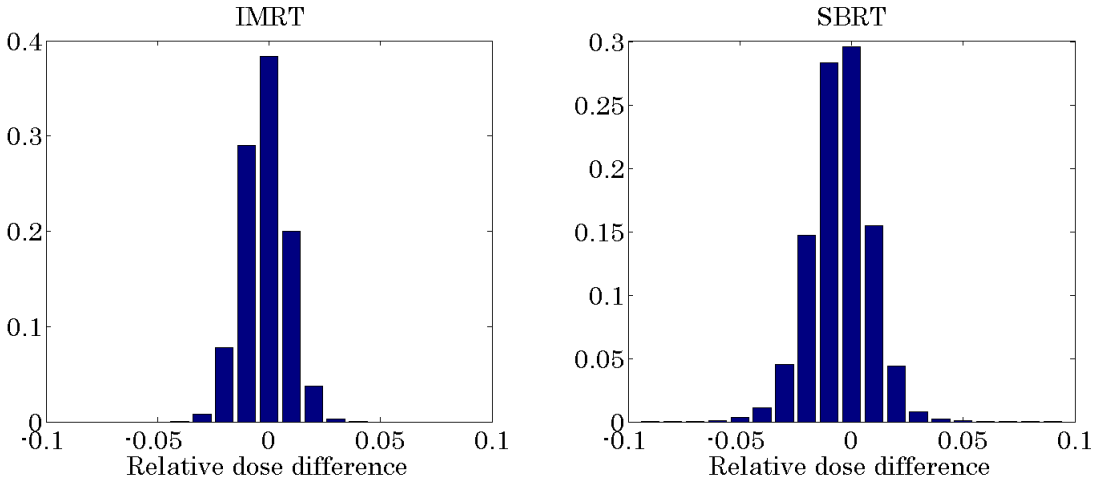

Figure 6.5: Relative dose-difference histograms comparing the composite dose delivered to the cylindrical phantom housing by the (a) IMRT and (b) SBRT treatment plans simulated with and without the application of a -0.08 mm offset to the planned MLC positions. Dose-differences were normalized to the dose distribution simulated without the MLC offset.

modeled as cortical bone, compact bone, and polyurethane. The film stack dosimeter and central cavity were each modeled as water with unit density.

DOSXYZnrc simulations provide dose and uncertainty results for each voxel within a phantom; therefore, simulations of larger phantoms have larger output files. For simulations run in parallel, as the simulations were in this work, each parallel job outputs a dose file, thereby substantially increasing the memory burden of simulations. For instance, using a Monte Carlo model of the LUNGMAN™ phantom with the native resolution of the CT dataset, the output files for each parallel job totaled approximately 150 MB. With a typical allotment of 80 parallel jobs per simulation, the total memory demand for a single simulation was approximately 12 GB. Given the segment-by-segment approach to the simulation of a treatment delivery and the resulting volume of total simulations, substantial reductions in the memory usage were required. To reduce the required memory for simulations, the CT dataset of the LUNGMAN™ phantom was subsampled to a resolution of $1.25 \times 1.25 \times$

1.25 mm^3 prior to creating the Monte Carlo model. The required memory for simulations was further reduced by excluding the treatment couch from the Monte Carlo phantom, suppressing the output of unused files, and limiting simulations to the minimum number of parallel jobs permitted by the computing system at the UWMRRC.

6.1.5.2 Simulation of measurements with moving dosimeter

For the simulation of the delivery of the treatment plans with a moving target, MATLAB® scripts were prepared to generate the necessary input files and to store the relevant details of each individual simulation. To prepare the input files, the treatment plan was selected, and the corresponding number of fields, number of segments per field, and MU per field were loaded. The time at which the delivery of each segment started and ended, relative to the start of phantom motion, was determined from the Logic measurements. The programmed motion waveform was loaded and binned into voxels with the resolution of the LUNGMAN™ Monte Carlo phantom. A loop was then executed over the number of segments in the treatment plan. For each segment, the corresponding target positions and the time spent at each position were determined. For each resulting target position, the appropriate Monte Carlo phantom was prepared if it did not already exist by shifting the film stack dosimeter data within the original LUNGMAN™ model to the current target position. The vacated voxels within the model were assigned to air. For the new Monte Carlo phantom, a separate simulation was written for the delivery of each segment in the treatment plan. Each simulation ran a number of histories equal to four times the number of particles in the phase-space file for the respective segment, resulting in approximately 10^6 to 10^7 histories per simulation, and approximately 10^9 histories per composite dose distribution. For the reconstruction of the composite dose distribution, the results of each simulation were weighted by the product of the dose rate and the time that the target spent at that location for the delivery of that segment.

The actual dose reconstruction includes delivery errors due to both interplay and blurring. In this work, interplay errors were isolated by referencing the reconstructed distribution to the delivered dose in the absence of interplay, termed the blurred distribution. To generate the blurred distribution, the temporal modulation of the treatment delivery had to be eliminated. The blurred distribution was constructed by weighting the dose distributions for the delivery of each segment to each target position based on the target position PDF for the entirety of the fraction delivery (i.e., independent of whether or not the beam was on). Effectively, this approach modeled the simultaneous delivery of every segment as the target progressed through its motion, thereby eliminating the temporal modulation of the delivery. The resulting blurred distribution was independent of the initial phase of motion, verifying the absence of interplay errors.

6.1.6 Comparison of measured and simulated dose distributions

The film stack dosimeter measurements were analyzed according to the procedure in Sec. 4.4.1.7 with a delay of 7 d between exposure and scanning of the films. The voxels in the simulated composite dose distributions corresponding to the film stack dosimeter volume were identified and extracted. The measured and simulated distributions were each normalized to the respective doses in the center of the film stack dosimeter volume. Corresponding distributions were compared using the gamma evaluation with dose-difference and DTA criteria of 3 % and 3 mm, respectively. The higher-resolution measured distributions were used as the searched distribution. The noise in the measured distributions was reduced with the application of a median filter in which each voxel was assigned the median value of the set of neighboring voxels.

The results of the gamma evaluations for the IMRT and SBRT treatment plans are shown in Tables 6.3 and 6.4, respectively. For the IMRT treatment plan, the agreement between measurements and simulations within the cylindrical phantom housing was excellent, further

Table 6.3: Comparison of film stack dosimeter measurements of the IMRT treatment plan with simulated reconstructions of the measurements. The measured and simulated distributions were compared using gamma criteria of 3 % dose difference and 3 mm DTA.

Exposure	Phantom	Motion	Gamma (%)
1	Cylindrical	Static	99.8
2	Cylindrical	Static	99.8
3	LUNGMAN™	Static	98.7
4	LUNGMAN™	Static	99.7
5	LUNGMAN™	1D	99.2
6	LUNGMAN™	1D	98.6
7	LUNGMAN™	3D	98.4
8	LUNGMAN™	3D	99.8

Table 6.4: Comparison of film stack dosimeter measurements of the SBRT treatment plan with simulated reconstructions of the measurements. Simulated reconstructions of the treatment delivery were completed both without and with the application of a -0.08 mm offset to the planned MLC positions. The measured and simulated distributions were compared using gamma criteria of 3 % dose difference and 3 mm DTA.

Exposure	Phantom	Motion	No MLC offset Gamma (%)	MLC offset Gamma (%)
9	Cylindrical	Static	99.8	99.8
10	LUNGMAN™	Static	99.8	99.8
11	LUNGMAN™	Static	98.6	99.1
12	LUNGMAN™	1D	97.5	98.4
13	LUNGMAN™	1D	97.8	97.7
14	LUNGMAN™	3D	98.8	98.6
15	LUNGMAN™	3D	98.5	97.5

verifying the Monte Carlo model of the Clinac® 21EX accelerator. In the absence of motion, there is good agreement between measurements and simulations of the IMRT plan within the LUNGMAN™ phantom, providing verification of the Monte Carlo model for this experimental geometry. For both the one-dimensional and three-dimensional target motion waveforms, there is good agreement between measurements and simulations of the IMRT plan, verifying the interplay simulation methodology.

For the SBRT treatment plan, simulated reconstructions of the treatment delivery were completed both without and with the application of a -0.08 mm offset to the planned MLC

positions. Overall, the agreement between measurements and simulations of the SBRT treatment plan is similar to that observed for the IMRT treatment plan. The impact of the MLC offset was inconsistent, improving agreement between measurements and simulations for some exposures, but worsening the agreement for others. Ultimately, the MLC offset was applied for simulations of the SBRT plan because the use of this offset improved the symmetry of dose-difference histograms comparing the simulated and measured distributions.

The sensitivity of the experimental verification procedure was tested by repeating the simulated reconstruction of the measurements with one-dimensional target motion with successive phase offsets of $\frac{\pi}{20}$ applied to the simulated motion waveform. The results of this test are shown in Table 6.5. The exposure labels correspond to the indices in Tables 6.3 and 6.4. For the SBRT treatment plan, a phase difference of $\frac{\pi}{10}$ between the measured and simulated motion waveforms was detectable, resulting in a failing gamma evaluation. The experimental verification was less sensitive for the IMRT treatment plan, for which a phase difference of $\frac{3\pi}{20}$ between the measured and simulated motion waveforms was detectable.

6.2 Simulated quantification of interplay errors

Following the completion of the verification of the interplay simulation methodology, interference errors in the delivery of the IMRT and SBRT treatment plans were investigated. Interference errors were identified and quantified for one-dimensional target motion. The impact of motion irregularity, specifically in the motion period, amplitude, and baseline offset, on interference errors with three-dimensional motion was then investigated. Finally, the cumulative delivery errors over a fractionated treatment delivery were determined.

Table 6.5: Results of the sensitivity study for the experimental verification of the interplay simulation methodology. The phase offset was applied to the simulated motion waveform for comparisons with measurements of the treatment deliveries. The exposure labels correspond to the indices in Tables 6.3 and 6.4. Gamma criteria of 3 % dose difference and 3 mm DTA were used.

Plan	Exposure	Phase offset	Gamma (%)
IMRT	5	$\pi/20$	96.0
		$\pi/10$	95.1
		$3\pi/20$	94.4
	6	$\pi/20$	94.3
		$\pi/10$	95.8
		$3\pi/20$	93.0
SBRT	12	$\pi/20$	97.7
		$\pi/10$	93.2
		$3\pi/20$	90.0
	13	$\pi/20$	93.8
		$\pi/10$	81.7
		$3\pi/20$	76.3

6.2.1 Interference in step-and-shoot IMRT

To identify and quantify potential interference errors in the delivery of the two treatment plans, treatments were simulated of a target undergoing one-dimensional, sinusoidal motion ranging in period from 1 s to 180 s. For the IMRT treatment plan, motion amplitudes of 5 mm and 15 mm were simulated, while for the SBRT plan, motion amplitudes of 5 mm and 10 mm were simulated. The 5 mm motion amplitude represents the largest motion that would be treated without management under the recommendations of AAPM Task Group 76, while the larger motion amplitudes are representative of respiratory motion for the target locations in this work [Seppenwoolde et al., 2002]. For each motion waveform, simulations were completed for twenty uniformly spaced initial phases of motion.

Simulated deliveries of each treatment plan were completed for a dose rate of 600 MU/min. Given the emergence of linear accelerators with flattening-filter-free treatment modes, and the potential application of the increased dose rate of this mode for the delivery of SBRT plans, the delivery of the SBRT plan in this work was also simulated with a dose rate of

1400 MU/min. The procedure described in Sec. 6.1.5.2 was used to prepare the necessary input files for the Monte Carlo simulations. The duration for the delivery of each segment was determined as the ratio of the MU per segment and the nominal dose rate. The delay between the delivery of segments within a given field measured with the logic analyzer was used to determine the time at which the delivery of each segment started. The delay between the delivery of successive fields was simulated as 50 $\pm$ 5 s ($k = 1$) for fields without couch rotations, and 130 $\pm$ 8 s ($k = 1$) for fields with couch rotations based on the delays measured with the logic analyzer.

Results of the simulations of interference errors for one-dimensional target motion are shown in Figs. 6.6 to 6.11. The simulated distributions which included the temporal modulation of the treatment delivery are referred to as interplay distributions, while the reference distributions that excluded temporal modulation are referred to as blurring distributions. The blurring distributions were simulated as described in Sec. 6.1.5.2. The results of the interference investigation are shown in the form of boxplots. Figs. 6.6 to 6.8 show the difference in the D_{98} of the film stack dosimeter phantom volume (i.e., CTV) between the interplay and blurring distributions normalized to the prescription dose. The D_{98} metric was recommended by ICRU report 83 [2010] as a surrogate for the near-minimum dose for the reporting of IMRT procedures. Each data point within these figures corresponds to the difference in D_{98} between the interplay and blurring distributions for a given motion waveform (i.e., amplitude, period, and initial phase). Each box represents the twenty different initial phases of motion that were simulated for a given combination of motion amplitude and period. In Figs. 6.6a, 6.7a, and 6.8a, the segment, intrafield (i.e., delivery of a single field), and interfield (i.e., delivery of successive fields) timescales are highlighted in green, blue, and red, respectively. For the IMRT plan, it is apparent from Fig. 6.6 that the greatest interference occurs with the intrafield and interfield modulations. In particular, reductions in the D_{98} relative to the blurring distribution of up to 2 % and 4 % are seen for motion

amplitudes of 5 mm and 15 mm, respectively, with maximum delivery errors for a motion period of 65 s. For typical respiratory periods of 3 s to 5 s, maximum interference errors are less than 1 %.

Simulated interference errors for the delivery of the SBRT treatment plan with a dose rate of 600 MU/min are shown in Fig. 6.7. Due to the increased dose per fraction, the representative segment and intrafield timescales for this treatment plan are approximately a factor of six greater than those for the IMRT treatment plan. With the use of couch rotations in this treatment plan, along with the increased dose per fraction, the interfield timescale is 2 min to 3 min. With the increased delivery timescales, the target position PDF is well-sampled for the shortest motion periods, resulting in negligible interference errors. As with the IMRT treatment plan, the greatest interference occurs with the intrafield and interfield modulations. Reductions in the D_{98} relative to the blurring distribution of up to 2 % and 5 % are seen for motion amplitudes of 5 mm and 10 mm, respectively, for motion periods ranging from 50 s to 135 s.

Simulated interference errors for the delivery of the SBRT treatment plan with a dose rate of 1400 MU/min are shown in Fig. 6.8. With the increased dose rate, the representative segment and intrafield timescales are correspondingly reduced by a factor of 2.3. Due to the reduced delivery timescales, larger interference errors occur for smaller motion periods. For instance, reductions in the D_{98} relative to the blurring distribution of up to 4 % are seen for motion periods as short as 30 s for a motion amplitude of 10 mm. Even with the increased dose rate, though, interference is minimal for typical respiratory periods of 3 s to 5 s. Maximum interference errors in excess of 2 % and 5 % are seen for motion amplitudes of 5 mm and 10 mm, respectively, for motion periods corresponding to the intrafield delivery timescale.

Interference errors were also quantified in terms of the difference in the volume of the CTV receiving the prescribed dose between the interplay and blurring distributions.

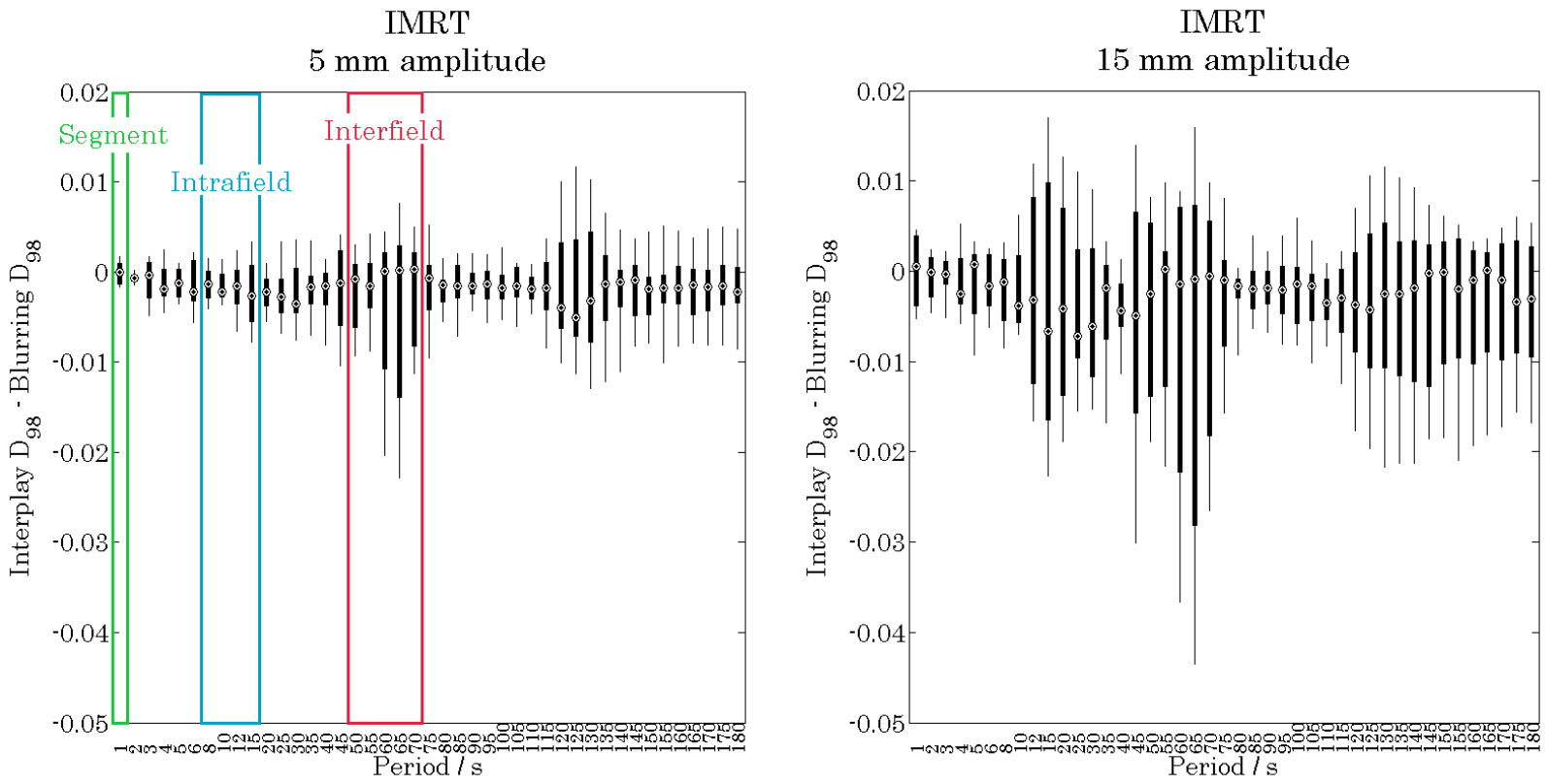

Figure 6.6: Simulated interference errors in the delivery of the IMRT treatment plan. Errors were simulated for motion amplitudes of (a) 5 mm and (b) 15 mm, and for motion periods from 1 s to 180 s. For each combination of motion amplitude and period, twenty uniformly spaced initial phases of motion were simulated. Errors are shown as the difference in the D_{98} of the film stack dosimeter phantom volume between the interplay and blurring distributions normalized to the prescription dose. Timescales for segment, intrafield, and interfield modulation are highlighted in (a).

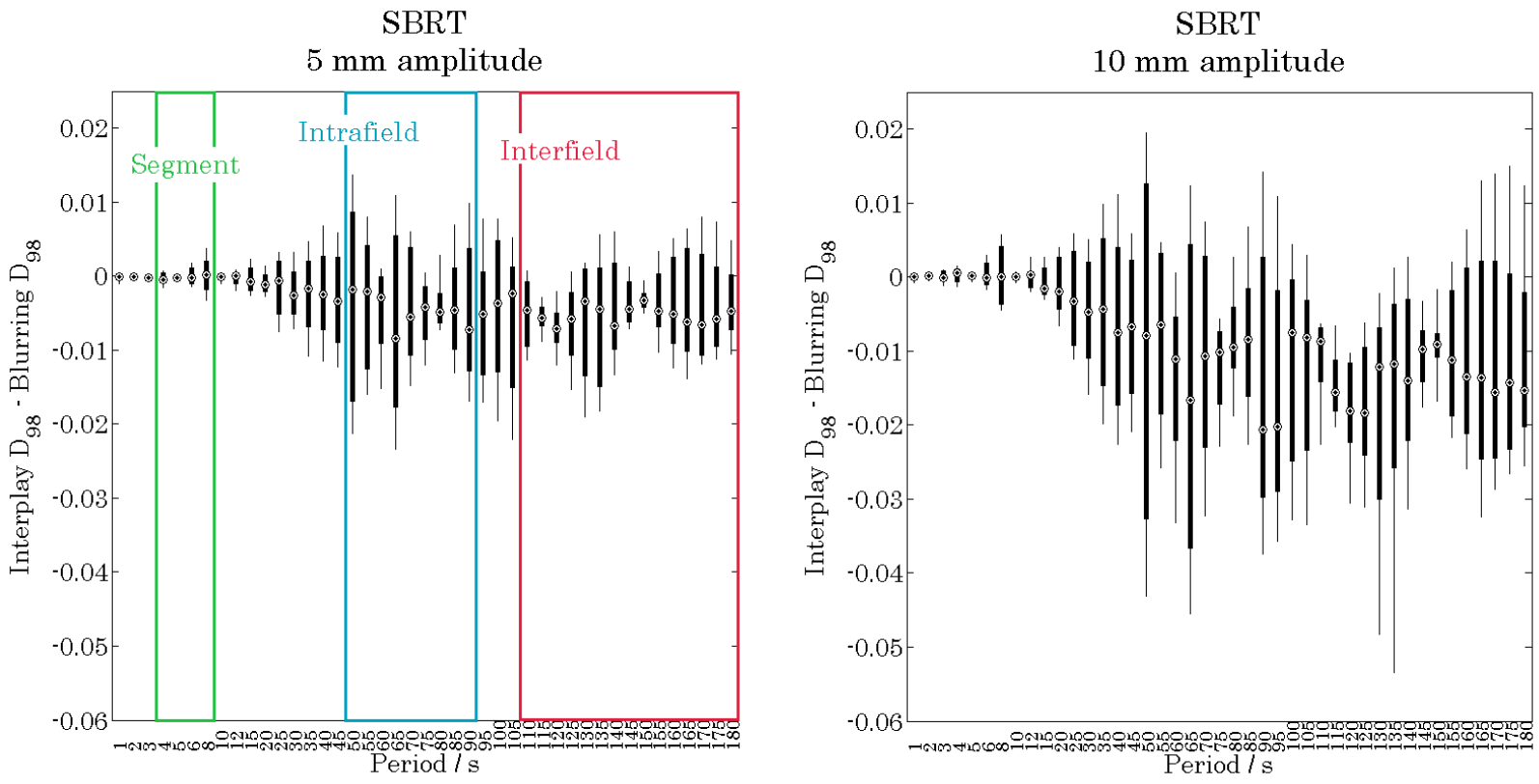

Figure 6.7: Simulated interference errors in the delivery of the SBRT treatment plan with a dose rate of 600 MU/min. Errors were simulated for motion amplitudes of (a) 5 mm and (b) 10 mm, and for motion periods from 1 s to 180 s. For each combination of motion amplitude and period, twenty uniformly spaced initial phases of motion were simulated. Errors are shown as the difference in the D_{98} of the film stack dosimeter phantom volume between the interplay and blurring distributions normalized to the prescription dose. Timescales for segment, intrafield, and interfield modulation are highlighted in (a).

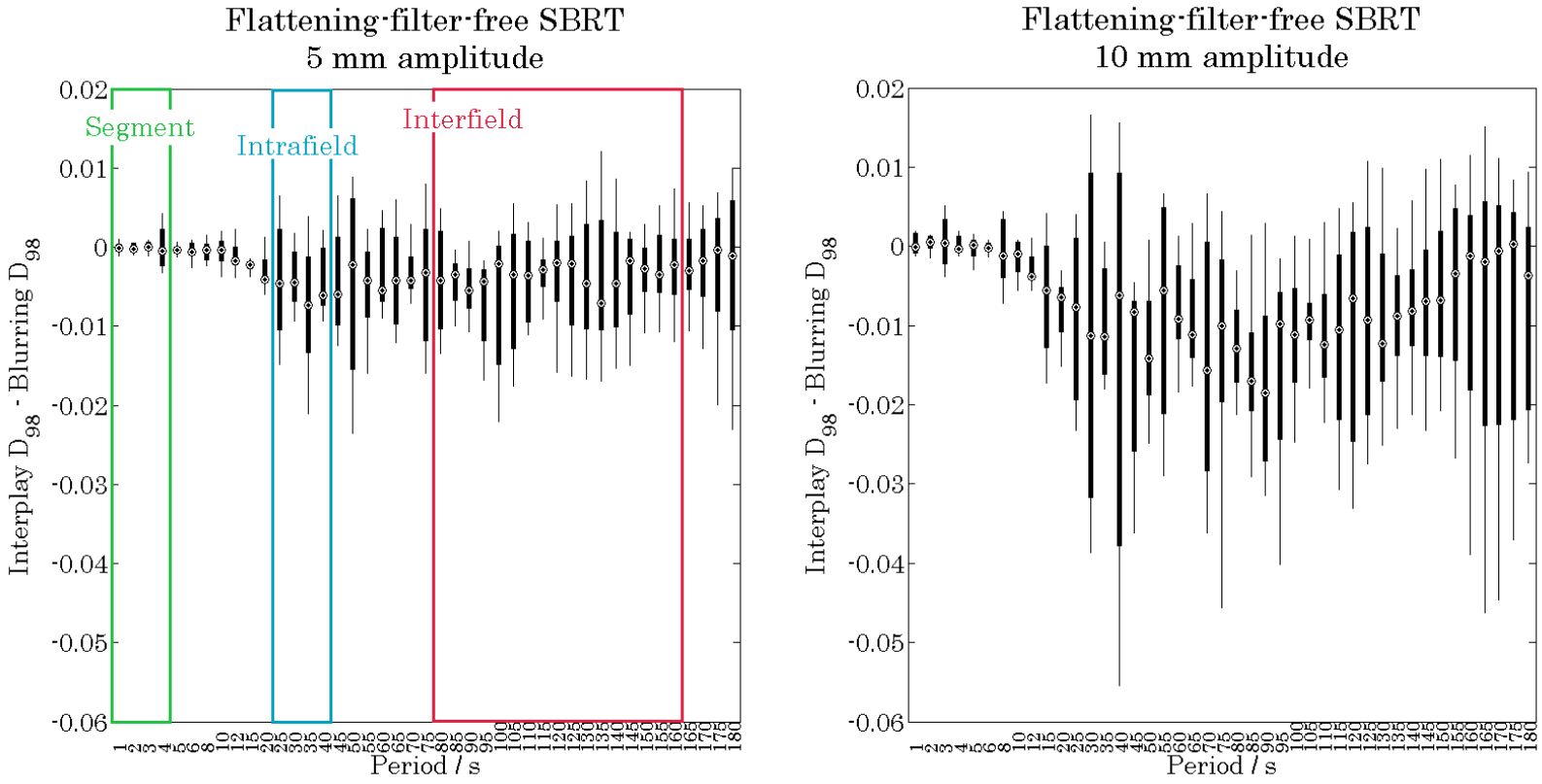

(a) (b)

Figure 6.8: Simulated interference errors in the delivery of the SBRT treatment plan with a dose rate of 1400 MU/min. Errors were simulated for motion amplitudes of (a) 5 mm and (b) 10 mm, and for motion periods from 1 s to 180 s. For each combination of motion amplitude and period, twenty uniformly spaced initial phases of motion were simulated. Errors are shown as the difference in the D_{98} of the film stack dosimeter phantom volume between the interplay and blurring distributions normalized to the prescription dose. Timescales for segment, intrafield, and interfield modulation are highlighted in (a).

Figs. 6.9 to 6.11 show the relative difference in the V_{100} of the CTV between the interplay and blurring distributions. Comparing the differences in the V_{100} with the differences in the D_{98}, the two metrics identify interference errors for consistent motion periods. For the larger motion amplitudes, reductions of 1 % to 2 % in the volume of the CTV receiving the prescription dose were seen. However, for a motion amplitude of 5 mm, for which AAPM Task Group 76 recommends the use of motion management [Keall et al., 2006], reductions in the CTV V_{100} did not exceed 1 % for any treatment delivery. While a dose deficit to just 1 % of the target volume has been shown to degrade the tumor control probability [Tomé and Fowler, 2002], dose deficits exceeding 20 % were required with such a small underdosed volume. In this work, the greatest dose deficits due to interference were less than 10 %, reducing the CTV V_{100} by less than 1 %, suggesting that interference errors are not sufficiently large to impact the tumor control probability.

While these results suggest that delivery errors due to interference in step-and-shoot IMRT are not clinically significant, they also demonstrate the importance of considering the irregularity of respiratory motion in investigations of the interplay effect. As can be seen in Figs. 6.6 to 6.11, if respiratory motion is modeled as a one-dimensional sinusoid with a motion period of 3 s to 5 s, then interplay errors are minimal. However, greater errors occurred for longer motion periods due to interference with characteristic intrafield and interfield delivery timescales. These longer motion periods are representative of lower-frequency components of respiratory motion, including changes in motion amplitude and drifts in the baseline position. Therefore, failure to realistically model respiratory motion results in an underestimation of interplay errors. The impact of irregularity in respiratory motion on interplay errors is further investigated in the next section.

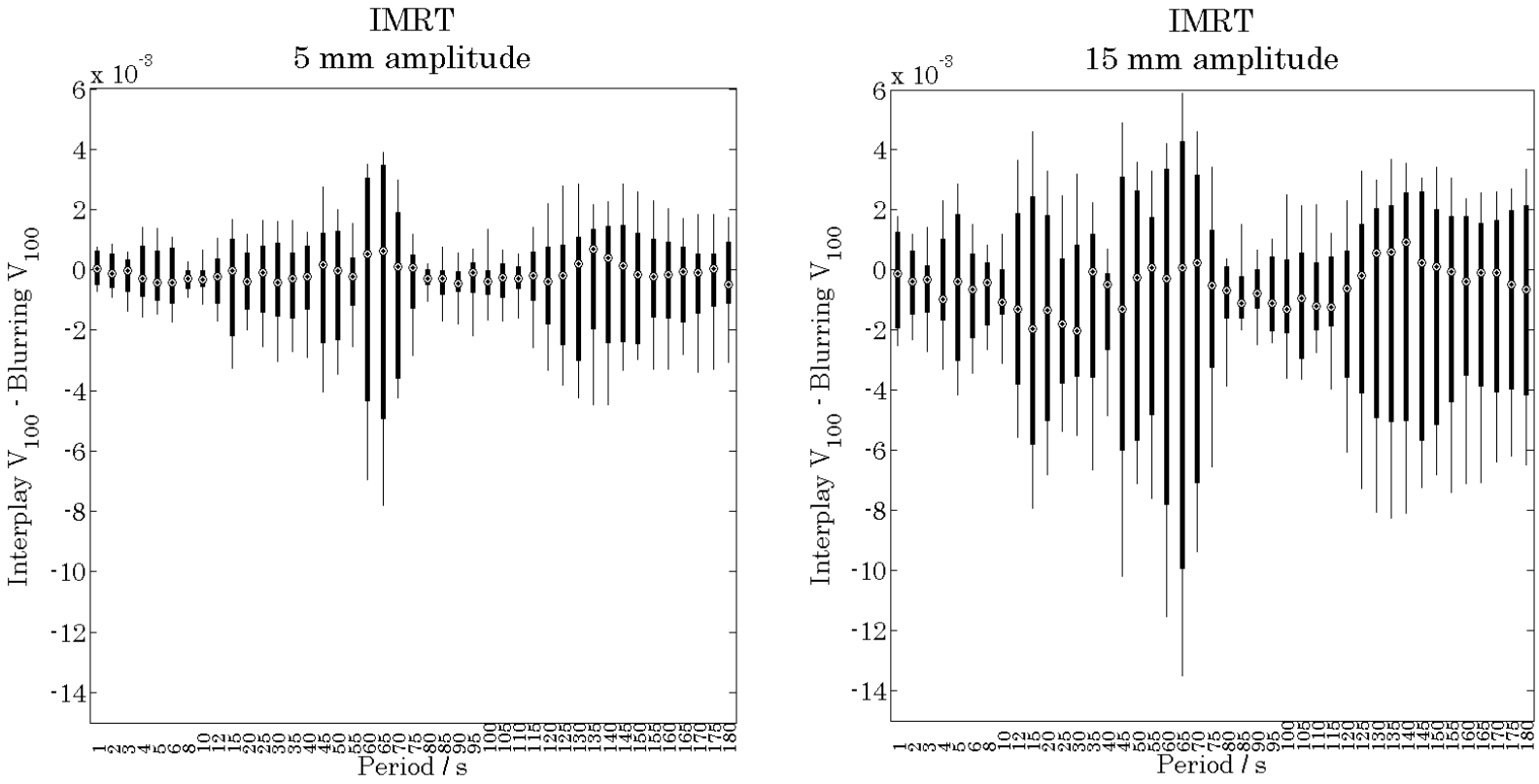

(a) (b)

Figure 6.9: Simulated interference errors in the delivery of the IMRT treatment plan. Errors were simulated for motion amplitudes of (a) 5 mm and (b) 15 mm, and for motion periods from 1 s to 180 s. For each combination of motion amplitude and period, twenty uniformly spaced initial phases of motion were simulated. Errors are shown as the relative difference in the V_{100} of the film stack dosimeter phantom volume between the interplay and blurring distributions.

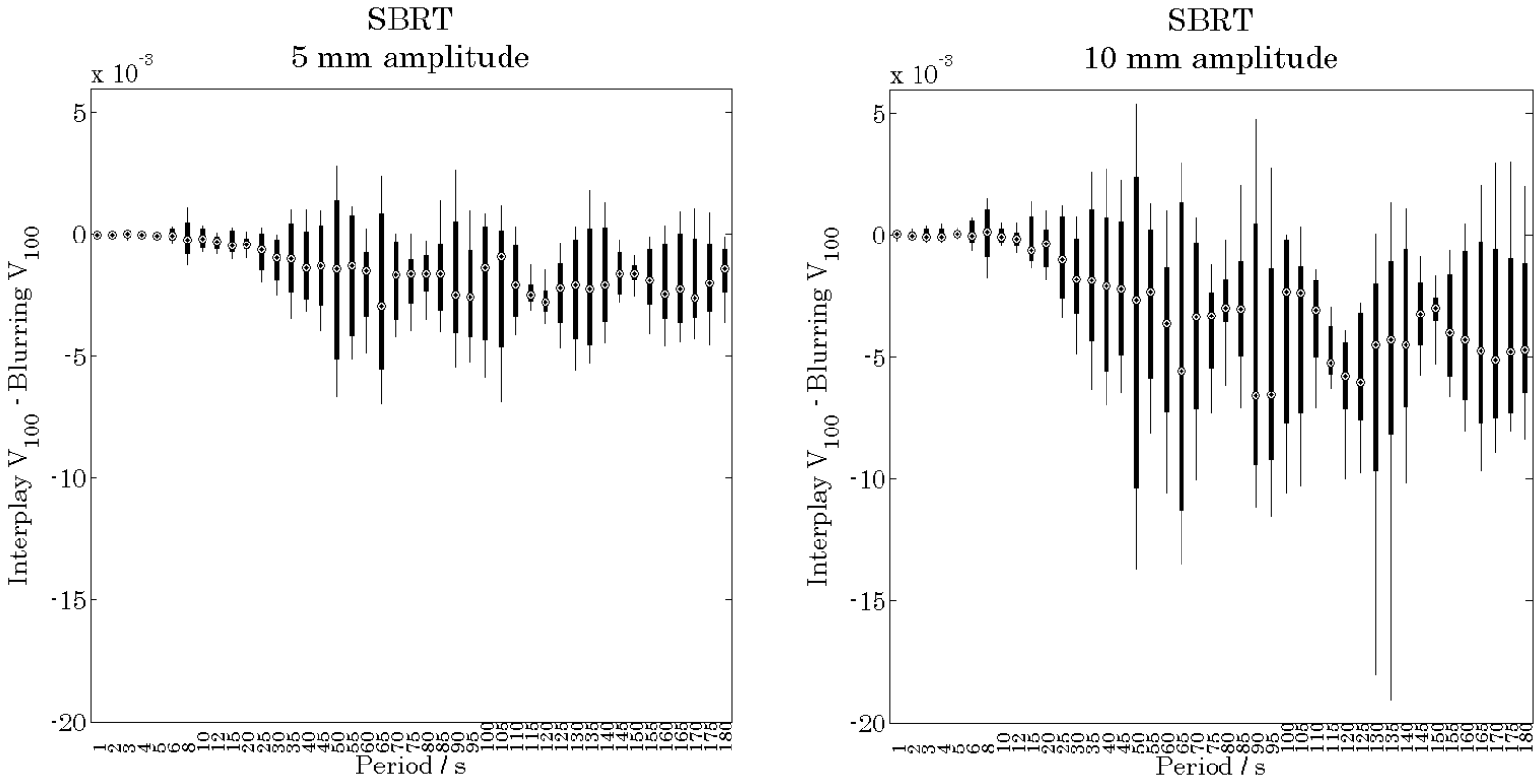

(a) (b)

Figure 6.10: Simulated interference errors in the delivery of the SBRT treatment plan with a dose rate of 600 MU/min. Errors were simulated for motion amplitudes of (a) 5 mm and (b) 10 mm, and for motion periods from 1 s to 180 s. For each combination of motion amplitude and period, twenty uniformly spaced initial phases of motion were simulated. Errors are shown as the relative difference in the V_{100} of the film stack dosimeter phantom volume between the interplay and blurring distributions.

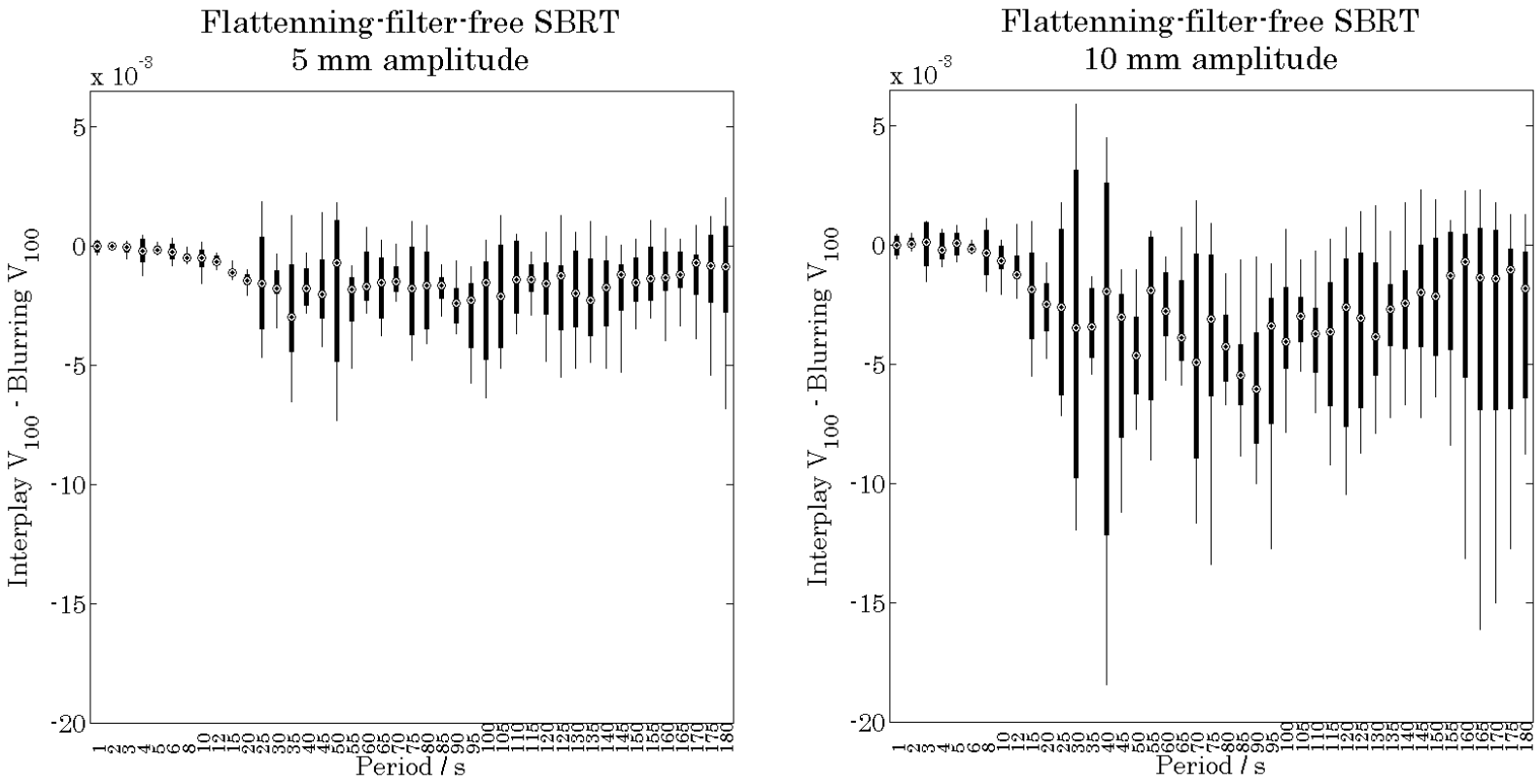

(a) (b)

Figure 6.11: Simulated interference errors in the delivery of the SBRT treatment plan with a dose rate of 1400 MU/min. Errors were simulated for motion amplitudes of (a) 5 mm and (b) 10 mm, and for motion periods from 1 s to 180 s. For each combination of motion amplitude and period, twenty uniformly spaced initial phases of motion were simulated. Errors are shown as the relative difference in the V_{100} of the film stack dosimeter phantom volume between the interplay and blurring distributions.

6.2.2 Effect of motion irregularity on interplay errors

The effect of respiratory motion irregularity on treatment delivery errors due to interplay was investigated using three-dimensional motion waveforms defined by Eq. 6.1. Three-dimensional motion waveforms were developed in which the standard deviation of either the motion period, motion amplitude, or baseline offset was incrementally varied, while the other two motion parameters were invariant. In this way, the impact of increased variability in each motion parameter on interplay errors was isolated. The mean motion parameters for the three-dimensional waveforms from Table 6.1 were used. For the IMRT treatment plan, waveforms were generated with a motion period standard deviation of 0.2 s to 1 s, motion amplitude standard deviation of 5 % to 25 % of the mean amplitude along each axis, and baseline offset standard deviation of 5 % (1 % for the superior-inferior axis) to 30 % (6 % for the superior-inferior axis) of the motion amplitude along each axis. For the variation in the motion amplitude and baseline offset, consistency with published data [Seppenwoolde et al., 2002] of the ratio of the percentage standard deviation of motion along each axis was maintained to avoid overemphasizing motion variation along any one axis. Thus, the percentage standard deviation in the baseline offset along the superior-inferior axis differed from that along the other two motion axes. With a standard deviation in motion amplitude of 25 % for the IMRT plan, approximately 5 % of the randomly sampled amplitude variations resulted in excursion of the CTV outside of the PTV. For the SBRT treatment plan, waveforms were generated with a motion period standard deviation of 0.2 s to 0.8 s, motion amplitude standard deviation of 5 % to 30 % of the mean amplitude along each axis, and baseline offset standard deviation of 5 % to 25 % of the motion amplitude along each axis. Motion along the anterior-posterior axis led that along the lateral and superior-inferior axes by $\frac{\pi}{4}$ [Seppenwoolde et al., 2002].

The methodology from Sec. 6.2.1 was used to simulate interplay errors for each of the generated waveforms. For each set of motion parameters, twenty uniformly spaced initial

phases of motion were simulated. Due to the variability in the motion parameters, the twenty different waveforms for a given set of motion parameters were not identical. Differences in the D_{98} of the CTV between the interplay and blurring distributions normalized to the prescription dose are shown in Figs. 6.12 and 6.13 for the IMRT and SBRT treatment plans, respectively. There are no apparent trends in the magnitude of interplay errors with increased variability in the motion period, motion amplitude, or baseline offset. Interplay errors were greater for the IMRT treatment plan; however, all errors were less than 1 %. These results demonstrate that the low-frequency motion components created by irregular respiratory motion do not have sufficient power to produce substantial interplay errors.

6.2.3 Cumulative interplay errors over a fractionated treatment course

The report of AAPM Task Group 76 justified the exclusion of frequency-dependent motion management criteria for the mitigation of interplay errors based on the observation that interplay errors reduce to inconsequential levels over the course of a fractionated treatment [Keall et al., 2006]. However, the studies referenced in this Task Group report assumed invariant, one-dimensional respiratory motion and a treatment consisting of thirty fractions. For hypofractionated treatments or realistic, irregular respiratory motion, the reduction in interplay errors over a fractionated treatment course may not be as substantial. In this thesis work, fractionated deliveries of each treatment plan were simulated to investigate the cumulative interplay errors over a full treatment course with variable, three-dimensional target motion.

Three-dimensional motion waveforms were prepared using the parameters in Table 6.1. Motion along the anterior-posterior axis led that along the lateral and superior-inferior axes by $\frac{\pi}{4}$ [Seppenwoolde et al., 2002]. For each treatment plan, 500 motion waveforms were generated in uniform increments of the initial phase. Interplay errors were simulated for each motion waveform following the methodology from Sec. 6.2.1, providing a set of 500

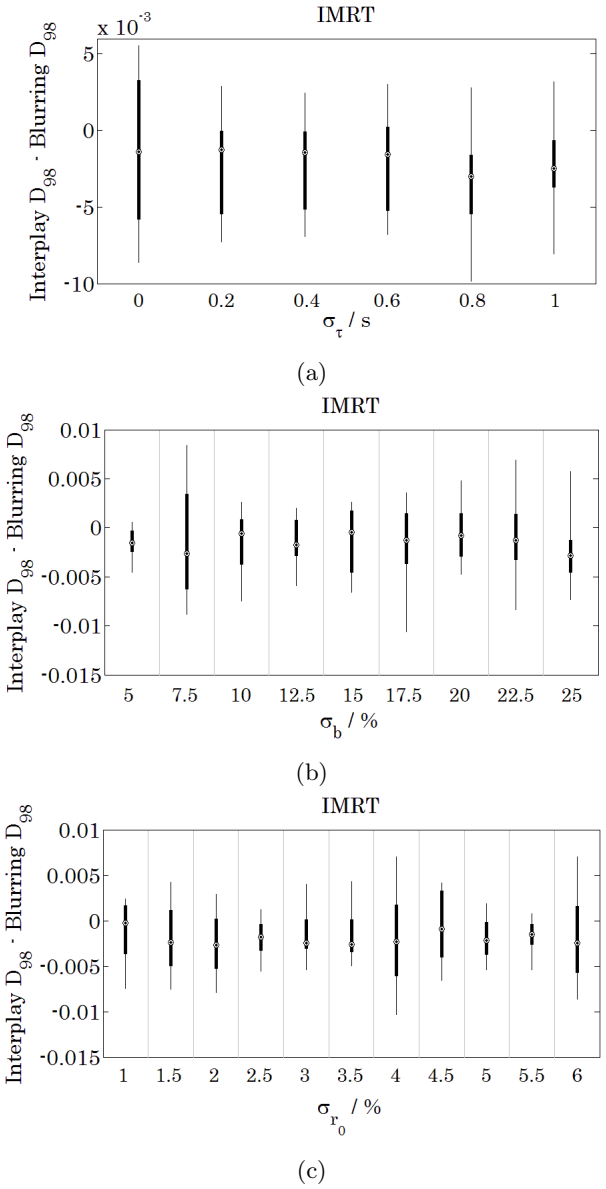

Figure 6.12: Simulated interference errors in the delivery of the IMRT treatment plan with incrementally varied (a) motion period, (b) motion amplitude, and (c) baseline offset. Results for variable motion amplitude and baseline offset are shown as a function of percent standard deviation relative to the mean motion amplitude along the superior-inferior axis. For each combination of motion parameters, twenty uniformly spaced initial phases of motion were simulated. Errors are shown as the difference in the D_{98} of the film stack dosimeter phantom volume between the interplay and blurring distributions normalized to the prescription dose.

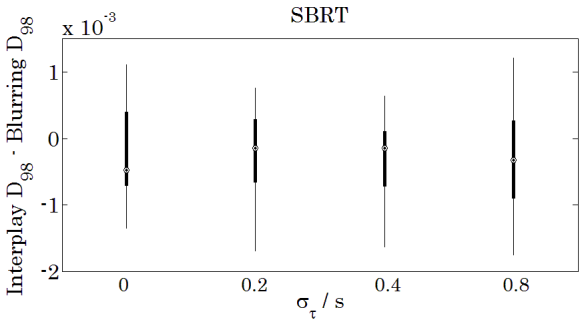

(a)

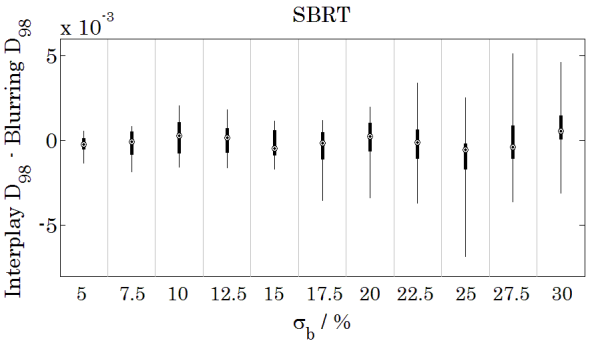

(b)

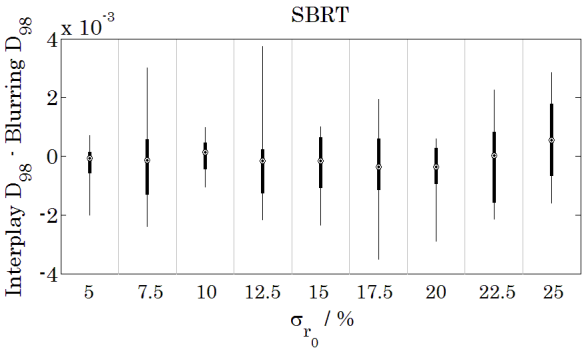

(c)

Figure 6.13: Simulated interference errors in the delivery of the SBRT treatment plan with incrementally varied (a) motion period, (b) motion amplitude, and (c) baseline offset. Results for variable motion amplitude and baseline offset are shown as a function of percent standard deviation relative to the mean motion amplitude along the superior-inferior axis. For each combination of motion parameters, twenty uniformly spaced initial phases of motion were simulated. Errors are shown as the difference in the D_{98} of the film stack dosimeter phantom volume between the interplay and blurring distributions normalized to the prescription dose.

fraction deliveries for each treatment plan. For each fraction delivery, interplay and blurring distributions were generated.

To simulate a fractionated treatment course, fraction deliveries were randomly sampled from a uniform distribution and summed. Treatment courses were simulated using both the interplay and blurring distributions for the sampled deliveries. For each treatment plan, the simulation of 500 separate treatment courses was completed. Histograms of the differences in the CTV D_{98} between the interplay and blurring distributions for each treatment course normalized to the prescription dose are shown in Fig. 6.14. For both treatment plans, the histograms of dose differences are centered at 0 %. For the SBRT treatment plan, the cumulative interplay errors over a fractionated treatment delivery are within ± 1 %. For the IMRT treatment plan, however, differences between the interplay and blurring distributions of up to ± 8 % are seen over a fractionated treatment course. Differences in the CTV V_{100} between the interplay and blurring distributions for each treatment course were also determined. Despite the differences in the CTV D_{98} shown in Fig. 6.14, there were no reductions in the volume of the CTV receiving the prescription dose in any of the simulated treatment courses for either treatment plan. Therefore, even with irregular target motion and hypofractionation, interplay errors are reduced to a negligible level over the entirety of a fractionated treatment course.

6.3 Conclusions

Interplay errors were quantified for step-and-shoot IMRT and SBRT treatment plans using the Monte Carlo model developed in Ch. 5. Step-and-shoot IMRT and SBRT treatment plans were prepared for clinical CT datasets of lung cancer patients. The use of the Monte Carlo model for the simulation of IMRT procedures and for the simulation of interplay errors was verified by comparing film stack dosimeter measurements of the delivery of each treatment plan with simulations of the treatment delivery.

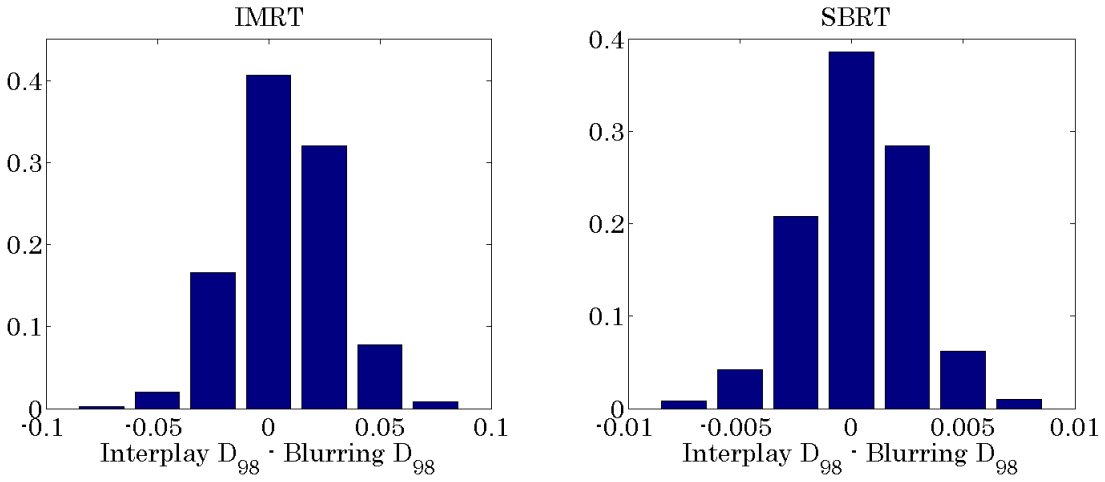

Figure 6.14: Histograms of differences in the CTV D_{98} between 500 fractionated treatment courses simulated using interplay and blurring distributions of the (a) IMRT and (b) SBRT treatment plans. Differences in the D_{98} were normalized to the prescription dose.

The delivery of each treatment plan was simulated for target motion periods of 1 s to 180 s to identify characteristic modulation frequencies of the treatment delivery and to quantify the delivery errors due to interference between the target motion and the intensity modulation. Interference errors were determined to be greatest for target motion periods corresponding to the timescales of intrafield and interfield modulation. While reductions of nearly 6 % in the CTV D_{98} were seen due to interplay in treatments with target motion amplitudes of 10 mm or 15 mm, the CTV V_{100} changed less than 1 % with target motion amplitudes of 5 mm. Likewise, increases in the standard deviations of the motion period, motion amplitude, and baseline offset did not result in CTV D_{98} changes greater than 1 %. Over a fractionated treatment course, there was no change in the volume of the CTV receiving the prescription dose due to interplay errors.

Chapter 7

Conclusions and future work

7.1 Conclusions

7.1.1 Film stack dosimeter

In this thesis work, a film stack dosimeter was developed using Gafchromic® EBT2 film. The dosimeter was comprised of 22 films with a diameter of 3.84 cm, with 1 mm-thick Virtual Water™ spacers interleaved for a total stack height of 2.72 cm. Within the film stack dosimeter phantom housing, the films were aligned with sub-millimeter precision.

The energy dependence, orientation dependence, and water equivalence of the film stack dosimeter were independently characterized. Based on the differences in the simulated energy spectra of the photon fluence through EBT2 film in the calibration and film stack dosimeter geometries, the energy dependence of the film stack dosimeter is less than 1.5 %. Additionally, the energy response differed by less than 0.1 % between films within the film stack dosimeter. For air gaps of 50 μm or greater between films, the response of the film stack dosimeter is approximately 3 % lower when the beam axis is parallel to the film planes, relative to the response for orthogonal incidence. For the smaller air gaps observed in the film stack dosimeter, the response of the dosimeter varies less than ± 1.25 % as a function

of the angle of incidence. Measurements with the film stack dosimeter of the PDD profile within a cylindrical Virtual Water™ phantom agreed with simulated PDD profiles within a cylindrical water phantom within a root-mean-square difference of 1.5 %.

Film stack dosimeter measurements were verified by comparison with TLD-100 microcube measurements. Measurements with the two dosimeters agreed within 5 % inside the field and within 0.5 mm in the field penumbra. Film stack dosimeter and TLD measurements had overall uncertainties of 6.0 % ($k = 2$) and 5.8 % ($k = 2$), respectively.

Finally, the film stack dosimeter was used to measure the dose distribution delivered by a seven-field, step-and-shoot IMRT treatment plan. Using dose-difference and DTA criteria of 3 % and 3 mm, respectively, the dose distributions measured with the film stack dosimeter had 99 % agreement with the calculated dose distribution.

The radiochromic film stack dosimeter was shown to be nearly water equivalent with minimal orientation dependence and energy dependence. Additionally, the film stack dosimeter has limited measurement uncertainty, providing a useful tool for 3D megavoltage photon beam dosimetry.

7.1.2 Monte Carlo linear accelerator model

A Monte Carlo model of the Clinac® 21EX linear accelerator was developed using EGSnrc. The physical components were modeled according to manufacturer specifications. The mean energy and the radial intensity distribution of the electron beam incident on the bremsstrahlung target were adjusted to achieve agreement between simulated and measured dose distributions within a water volume. An optimal beam energy of 6.05 MeV was determined by comparison of PDD profiles, while an optimal radial intensity distribution of 1.5 mm FWHM was determined by comparison of penumbra of inline and crossline profiles. These beam parameters are consistent with published models of similar linear accelerators [Sheikh-Bagheri and Rogers, 2002a; Ding, 2002; Keall et al., 2003]. Simulated PDD, inline,

and crossline profiles with these beam parameters agreed with measured profiles for a range of field sizes within 2 % and 1 mm.

With the completed optimization of electron beam parameters, the model of the Millennium 120 MLC was verified. The simulated leakage through a field fully blocked by the MLC was compared with leakage measurements to verify the density of the MLC. Through the comparison of the simulated and measured output of sweeping MLC fields with different MLC openings, it was determined that there is an offset of approximately 0.08 mm between the planned and actual MLC positions in the MLC midplane. This offset had the greatest impact on fields with smaller MLC openings, which could impact the accuracy of IMRT simulations. Agreement between measured and simulated inline and crossline profiles of fields defined by the MLC was within 2 % and 1 mm.

7.1.3 Interplay errors in step-and-shoot IMRT

Two seven-field, step-and-shoot IMRT treatment plans, one conventionally fractionated and one hypofractionated, were prepared using CT datasets of lung cancer patients for the investigation of interplay errors. The delivery of these treatment plans was measured using the film stack dosimeter within the cylindrical phantom housing and compared with simulations of the treatment deliveries to verify the simulation of IMRT procedures with the Monte Carlo accelerator model. It was demonstrated that the treatment couch does not significantly impact the dose at depth within the phantom. Furthermore, the observed offset between planned and actual MLC positions did not significantly affect simulations of the conventionally fractionated treatment plan. However, differences in simulations of the hypofractionated plan with and without an offset of -0.08 mm applied to the MLC positions exceeded the simulation uncertainty ($k = 1$). The hypofractionated treatment plan had more MLC segments with smaller apertures, so it is reasonable that the MLC offset would have a greater impact for this treatment plan. Using gamma criteria of 3 % and 3 mm,

measurements and simulations of both treatment plans had greater than 99 % agreement, verifying the simulation of IMRT procedures with the Monte Carlo linear accelerator model.

To verify the Monte Carlo modeling of the LUNGMAN™ phantom in which measurements of interplay errors were completed, the delivery of each treatment plan was measured using the film stack dosimeter positioned within the LUNGMAN™ phantom and compared with simulations of the treatment deliveries. The measured and simulated distributions had 98 % to 99 % agreement, verifying the modeling of the experimental geometry for the investigation of interplay errors. Finally, to verify the methodology for the simulation of interplay errors, the delivery of each treatment plan was measured with the film stack dosimeter moving according to one-dimensional and three-dimensional respiratory motion waveforms. These measurements had 97 % to 99 % agreement with corresponding simulations, thereby verifying the interplay simulation methodology. The comparison of measured and simulated distributions was able to detect phase differences between the measured and simulated motion waveforms of $\frac{3\pi}{20}$ and $\frac{\pi}{10}$ for the conventionally fractionated and hypofractionated treatment plans, respectively.

Following the verification of the interplay simulation methodology, interplay errors were investigated for the two treatment plans. The delivery of each treatment plan was simulated for one-dimensional target motion with periods ranging from 1 s to 180 s to identify characteristic modulation timescales and quantify delivery errors due to interference between target motion and intensity modulation. For target motion amplitudes of 10 mm to 15 mm, interplay errors reduced the CTV D_{98} by up to 5 % to 6 %. For both treatment plans, the greatest interference was with the intrafield and interfield modulations, corresponding to longer motion periods characteristic of drifts in the motion waveform. Interference over the timescale of typical respiratory motion periods was negligible. Using an elevated dose rate representative of a flattening-filter-free treatment, interplay errors for the hypofractionated plan increased and shifted toward shorter motion periods. Despite the greater

interplay errors seen for larger motion amplitudes, the volume of the CTV receiving the prescription dose did not change more than 1 % for motion amplitudes of 5 mm. Therefore, the amplitude-based motion-management criteria recommended by AAPM Task Group 76 appear to be sufficient for the management of interplay errors in step-and-shoot IMRT.

The greatest interplay errors were observed for longer target motion periods, which are representative of drifts in the target position due to irregularities in the target motion. To investigate the impact of motion irregularity on interplay errors, simulations were also completed for three-dimensional target motion with incremented variations in the motion period, amplitude, and baseline offset. Even for motion variations much greater than measured for lung cancer patients [Seppenwoolde et al., 2002], no changes in the CTV D_{98} greater than 1 % were observed. These results suggest that the low-frequency drifts in target position created by irregular target motion have insufficient power to produce substantial interplay errors.

AAPM Task Group 76 disregarded interplay errors in its recommendations for the use of respiratory motion management based on the observation that these errors become negligible over thirty fractions [Keall et al., 2006]. However, the referenced studies modeled respiratory motion as an invariant, one-dimensional sinusoid [Bortfeld et al., 2002; Jiang et al., 2003]. In this work, the cumulative interplay errors over a fractionated treatment course were simulated for irregular, three-dimensional respiratory motion. Even with motion amplitudes representative of unmanaged respiratory motion and a treatment course of just four fractions, there was no change in the CTV V_{100} due to interplay over a complete treatment course. Therefore, no additional recommendations beyond those made by AAPM Task Group 76 [Keall et al., 2006] are necessary for the management of interplay errors in step-and-shoot IMRT of the lung.

7.2 Recommendations for future work

7.2.1 Characterization of multichannel film analysis methods

For films analyzed using a flatbed scanner operated in red-green-blue mode, analysis methods have been proposed utilizing the signal from all three color channels to correct for the nonuniformity of the film response and for certain scanner artifacts [Micke et al., 2011]. However, as demonstrated in Sec. 3.1.4.1, the signal in the blue-color channel of a single film scanned repeatedly follows a continuously increasing trend. Depending on the cause of this trending response, the signal in the blue-color channel of several films scanned a single time in succession could also be impacted. Consequently, any measurement requiring the scanning of multiple films, including the calibration of the film response, would incur added uncertainty.

The dependence of the trending response on both the scanner and the film should be separately investigated. Other types of film can be tested to determine if this observation is unique to EBT2 film, or if this behavior is characteristic of the scanner. In this thesis work, it was hypothesized that the trend in the blue-channel signal is temperature-dependent based on the observation that the temperature of the scanbed increased with repeated scans. To test this hypothesis, a film should be heated to multiple known temperatures independently of the scanner and scanned. In a separate test, the scanbed could be independently heated to known temperatures by repeated scanning of a blank surface. At each temperature, a piece of film could be scanned once, without allowing for the film temperature to equilibrate with that of the scanbed. The added uncertainty due to the blue-channel trend could be estimated by repeatedly scanning a set of films one-at-a-time in a randomized order. Such an experiment would quantify the repeatability of the measured transmission through a film when scanned with several other films, such as for the generation of a calibration curve.

Following an investigation of the blue-channel trend, a comprehensive uncertainty analysis of the multichannel film analysis method should be completed. This uncertainty analysis could follow the methodology of Devic et al. [2005]. For comparison, an uncertainty analysis of the same films should be completed using the net OD analysis method employed in this thesis work. In particular, differences in the film uniformity between the two analysis methods are of interest. To test the uniformity of the film response, small regions should be analyzed over many calibration films exposed to the same dose.

7.2.2 Improvements to the film stack dosimeter

Multiple changes can be made to the film stack dosimeter to improve measurement versatility and uncertainty. In this thesis work, the film stack dosimeter was designed to represent a lung tumor volume. Consequently, a relatively small film stack dosimeter was developed. A larger detector volume would increase the potential applications of the film stack dosimeter. For any change in detector size, the energy dependence, orientation dependence, and water equivalence should be recharacterized. EBT2 film was chosen in this thesis work due to the observation of substantial edge artifacts when cutting EBT3 film. However, the use of laser cutting may reduce edge artifacts relative to mechanical cutting, which would make an EBT3 film stack dosimeter feasible. The response of EBT3 film has been shown to be much less dependent on the energy of the incident radiation than that of EBT2 film [Brown et al., 2012]. Moreover, a recent study has investigated different formulations for the active layer of EBT3 to minimize the energy dependence of the film response below photon energies of 100 keV [Bekerat et al., 2014]. Therefore, the use of EBT3 film could reduce the energy dependence, and consequently the measurement uncertainty, of the film stack dosimeter.

7.2.3 Dependence of interplay errors on treatment plan complexity

In this thesis work, it was determined that interference over the timescale of typical respiratory motion periods (i.e., 3 s to 5 s) is negligible. This range of times corresponds to the characteristic timescale for the delivery of MLC segments. Consequently, these results suggest that interplay errors are minimally dependent on the complexity of the MLC arrangements for each field. However, Court et al. [2010b] demonstrated that SW-IMRT and VMAT plans with intentionally increased complexity (i.e., smaller MLC apertures and more MLC segments per field) were subject to greater interplay errors than their less complex counterparts. If interplay errors are indeed dependent on plan complexity, then the limitation of plan complexity would be a straightforward method for the mitigation of interplay errors. To determine the dependence of interplay errors on plan complexity, a metric is needed to quantify the complexity of a treatment plan. Multiple metrics have been proposed for the quantification of plan complexity [Webb, 2003; McNiven et al., 2010]. The metric should consider the complexity of MLC segments, including number of segments per field, aperture size, and leaf separation, as well as the number of beams in the treatment plan and the MU per beam, given that the greatest interplay errors were attributed to interference with the intrafield and interfield modulation. With a means to quantify the complexity of treatment plans, the methodology from Sec. 6.2.1 could be used to quantify interference errors for several treatments plans of differing complexity. With the results of such an investigation, the correlation between plan complexity and interplay errors could be determined.

7.2.4 Interplay errors in sliding-window IMRT and VMAT

As asserted by Kissick and Mackie [2009], characteristic modulation frequencies differ between treatment modalities, requiring separate characterization of interference errors for each. This thesis work investigated step-and-shoot IMRT treatments, but additional in-

vestigations are required for sliding-window IMRT and VMAT. While interplay errors have been investigated in a limited capacity for these treatment techniques [Court et al., 2008, 2010a; Stambaugh et al., 2013], a more comprehensive investigation such as that completed in this thesis work is required to identify characteristic modulation frequencies and to quantify the resulting interference errors. A methodology similar to that from Sec. 6.2.1 could be used for such an investigation. However, due to the continuous fluence modulation of the sliding-window IMRT and VMAT techniques, the generation of phase-space files for each MLC arrangement is not feasible. Instead of using phase-space sources, a separate BEAMnrc simulation could be run for each simulation of a given target position. For the range of times that the target occupies a given position, the range of MLC positions could be determined. These position limits would then be used for a BEAMnrc simulation with dynamic MLC positioning. The primary limitation to running a separate BEAMnrc simulation for each target position is the increased time requirement. However, efficiency-enhancing techniques have been demonstrated for BEAMnrc simulations in which the simulation of bremsstrahlung generation is comparable in efficiency to the use of phase-space sources [Kawrakow and Walters, 2006].

7.3 Closing remarks

Delivery errors due to interplay in step-and-shoot IMRT are primarily the result of interference between the target motion and the intrafield and interfield modulation of the treatment delivery. While these errors are dependent on the frequency of the target motion, they are sufficiently mitigated with the use of the amplitude-based respiratory-motion-management criteria recommended by AAPM Task Group 76 [Keall et al., 2006]. Investigation of the correlation between treatment plan complexity and interplay errors would provide justification for broader generalization of the results of this thesis work. Additional investigations are required to quantify interference errors in sliding-window IMRT and VMAT treatments

and to determine if frequency-based motion-management criteria are necessary for these treatments.

Bibliography

A. Ahnesjö. Collapsed cone convolution of radiant energy for photon dose calculation in heterogeneous media. *Med Phys*, 16(4):577–592, 1989.

S. S. Almberg, J. Frengen, A. Kylling, and T. Lindmo. Monte Carlo linear accelerator simulation of megavoltage photon beams: independent determination of initial beam parameters. *Med Phys*, 39(1):40–7, 2012.

P. R. Almond, P. J. Biggs, B. M. Coursey, W. F. Hanson, M. S. Huq, R. Nath, and D. W. O. Rogers. AAPM's TG-51 protocol for clinical reference dosimetry of high-energy photon and electron beams. *Med Phys*, 26(9):1847–1870, 1999.

C. Andrés, A. del Castillo, R. Tortosa, D. Alonso, and R. Barquero. A comprehensive study of the Gafchromic EBT2 radiochromic film. A comparison with EBT. *Med Phys*, 37(12): 6271–6278, 2010.

A. Appleby, E. A. Christman, and A. Leghrouz. Imaging of spatial radiation dose distribution in agarose gels using magnetic resonance. *Med Phys*, 14(3):382–384, 1987.

B. Arjomandy, R. Tailor, A. Anand, N. Sahoo, M. Gillin, K. Prado, and M. Vicic. Energy dependence and dose response of Gafchromic EBT2 film over a wide range of photon, electron, and proton beam energies. *Med Phys*, 37(5):1942–1947, 2010.

M. R. Arnfield, J. V. Siebers, J. O. Kim, Q. Wu, P. J. Keall, and R. Mohan. A method for determining multileaf collimator transmission and scatter for dynamic intensity modulated radiotherapy. *Med Phys*, 27(10):2231–2241, 2000.

F. H. Attix. *Introduction to Radiological Physics and Radiation Dosimetry*. John Wiley and Sons, Inc., New York, 1986.

C. Baldock, Y. De Deene, S. Doran, G. Ibbott, A. Jirasek, M. Lepage, K. B. McAuley, M. Oldham, and L. J. Schreiner. Polymer gel dosimetry. *Phys Med Biol*, 55(5):R1–R63, 2010.

W. A. Beckham, P. J. Keall, and J. V. Siebers. A fluence-convolution method to calculate radiation therapy dose distributions that incorporate random set-up error. *Phys Med Biol*, 47(19):3465–3473, 2002.

H. Bekerat, S. Devic, F. DeBlois, K. Singh, A. Sarfehnia, J. Seuntjens, S. Shih, X. Yu, and D. Lewis. Improving the energy response of external beam therapy (EBT) GafChromicTM dosimetry films at low energies (100 keV). *Med Phys*, 41(2):022101, 2014.

R. I. Berbeco, S. Nishioka, H. Shirato, G. T. Chen, and S. B. Jiang. Residual motion of lung tumours in gated radiotherapy with external respiratory surrogates. *Phys Med Biol*, 50(16):3655–3667, 2005.

R. I. Berbeco, C. J. Pope, and S. B. Jiang. Measurement of the interplay effect in lung IMRT treatment using EDR2 films. *J Appl Clin Med Phys*, 7(4):33–42, 2006.

M. J. Berger. *Monte Carlo calculation of the penetration and diffusion of fast charged particles*, volume 1, page 135. Academic Press, New York, 1963.

A. F. Bielajew and D. W. O. Rogers. *Electron step-size artefacts and PRESTA*, pages 115–137. Plenum, New York, 1988.

J. M. Blackall, S. Ahmad, M. E. Miquel, J. R. McClelland, D. B. Landau, and D. J. Hawkes. MRI-based measurements of respiratory motion variability and assessment of imaging strategies for radiotherapy planning. *Phys Med Biol*, 51(17):4147–4169, 2006.

T. Bortfeld, K. Jokivarsi, M. Goitein, J. Kung, and S. B. Jiang. Effects of intra-fraction motion on IMRT dose delivery: statistical analysis and simulation. *Phys Med Biol*, 47 (13):2203–2220, 2002.

T. Bortfeld and H. Paganetti. The biologic relevance of daily dose variations in adaptive treatment planning. *Int J Radiat Oncol Biol Phys*, 65(3):899–906, 2006.

A. Brahme. Optimization of stationary and moving beam radiation therapy techniques. *Radiother Oncol*, 12(2):129–140, 1988.

T. A. Brown, K. R. Hogstrom, D. Alvarez, K. L. Matthews II, K. Ham, and J. P. Dugas. Dose-response curve of EBT, EBT2, and EBT3 radiochromic films to synchrotron-produced monochromatic x-ray beams. *Med Phys*, 39(12):7412–7417, 2012.

E. N. Bruce. Temporal variations in the pattern of breathing. *J Appl Physiol*, 80(4): 1079–1087, 1996.

M. J. Butson, T. Cheung, and P. K. Yu. Spatial resolution of a stacked radiochromic film dosimeter. *Radiother Oncol*, 61(2):211–213, 2001.

J. Cameron, D. Zimmerman, G. Kenney, R. Buch, R. Bland, and R. Grant. Thermoluminescent radiation dosimetry utilizing LiF. *Health Phys*, 10:25–29, 1964.

S. R. Chaudhari, S. M. Goddu, D. Rangaraj, O. L. Pechenaya, W. Lu, E. Kintzel, K. Malinowski, P. J. Parikh, J. D. Bradley, and D. A. Low. Dosimetric variances anticipated from breathing- induced tumor motion during tomotherapy treatment delivery. *Phys Med Biol*, 54(8):2541–2555, 2009.

T. Cheung, M. J. Butson, and P. K. Yu. Use of multiple layers of Gafchromic film to increase sensitivity. *Phys Med Biol*, 46(10):N235–N240, 2001.

T. Cheung, M. J. Butson, and P. K. Yu. Multilayer Gafchromic film detectors for breast skin dose determination *in vivo*. *Phys Med Biol*, 47(2):N31–N37, 2002.

O. Chibani, B. Moftah, and C. M. Ma. On Monte Carlo modeling of megavoltage photon beams: a revisited study on the sensitivity of beam parameters. *Med Phys*, 38(1):188–201, 2011.

A. B. Chilton. A note on the fluence concept. *Health Phys*, 34(6):715–716, 1978.

S. T. Chiu-Tsao and M. F. Chan. Photon beam dosimetry in the superficial buildup region using radiochromic EBT film stack. *Med Phys*, 36(6):2074–2083, 2009.

S. T. Chiu-Tsao, T. L. Duckworth, N. S. Patel, J. Pisch, and L. B. Harrison. Verification of Ir-192 near source dosimetry using GAFCHROMIC® film. *Med Phys*, 31(2):201–207, 2004.

B. Cho, P. R. Poulsen, A. Sloutsky, A. Sawant, and P. J. Keall. First demonstration of combined kV/MV image-guided real-time dynamic multileaf-collimator target tracking. *Int J Radiat Oncol Biol Phys*, 74(3):859–867, 2009.

L. Court, M. Wagar, R. Berbeco, A. Reisner, B. Winey, D. Schofield, D. Ionascu, A. M. Allen, R. Popple, and T. Lingos. Evaluation of the interplay effect when using RapidArc to treat targets moving in the craniocaudal or right-left direction. *Med Phys*, 37(1):4–11, 2010a.

L. E. Court, J. Seco, X. Q. Lu, K. Ebe, C. Mayo, D. Ionascu, B. Winey, N. Giakoumakis, M. Aristophanous, R. Berbeco, J. Rottman, M. Bogdanov, D. Schofield, and T. Lingos. Use of a realistic breathing lung phantom to evaluate dose delivery errors. *Med Phys*, 37 (11):5850–5857, 2010b.

L. E. Court, M. Wagar, D. Ionascu, R. Berbeco, and L. Chin. Management of the interplay effect when using dynamic MLC sequences to treat moving targets. *Med Phys*, 35(5): 1926–1931, 2008.

T. Craig, J. Battista, and J. Van Dyk. Limitations of a convolution method for modeling geometric uncertainties in radiation therapy. I. The effect of shift invariance. *Med Phys*, 30(8):2001–2011, 2003.

L. A. R. da Rosa, D. F. Regulla, and U. A. Fill. Reproducibility study of TLD-100 microcubes at radiotherapy dose level. *Appl Radiat Isotopes*, 50(3):573–577, 1999.

Y. De Deene, C. De Wagter, B. Van Duyse, S. Derycke, W. De Neve, and E. Achten. Three-dimensional dosimetry using polymer gel and magnetic resonance imaging applied to the verification of conformal radiation therapy in head-and-neck cancer. *Radiother Oncol*, 48 (3):283–291, 1998.

Y. De Deene, P. Hanselaer, C. De Wagter, E. Achten, and W. De Neve. An investigation of the chemical stability of a monomer/polymer gel dosimeter. *Phys Med Biol*, 45(4): 859–878, 2000.

Y. De Deene, G. Pittomvils, and S. Visalatchi. The influence of cooling rate on the accuracy of normoxic polymer gel dosimeters. *Phys Med Biol*, 52(10):2719–2728, 2007.

S. Devic, S. Aldelaijan, H. Mohammed, N. Tomic, L. H. Liang, F. DeBlois, and J. Seuntjens. Absorption spectra time evolution of EBT-2 model GAFCHROMIC™ film. *Med Phys*, 37 (5):2207–2214, 2010.

S. Devic, J. Seuntjens, G. Hegyi, E. B. Podgorsak, C. G. Soares, A. S. Kirov, I. Ali, J. F. Williamson, and A. Elizondo. Dosimetric properties of improved GafChromic films for seven different digitizers. *Med Phys*, 31(9):2392–2401, 2004.

S. Devic, J. Seuntjens, E. Sham, E. B. Podgorsak, C. R. Schmidtlein, A. S. Kirov, and C. G. Soares. Precise radiochromic film dosimetry using a flat-bed document scanner. *Med Phys*, 32(7):2245–2253, 2005.

S. Devic, Y. Z. Wang, N. Tomic, and E. B. Podgorsak. Sensitivity of linear CCD array based film scanners used for film dosimetry. *Med Phys*, 33(11):3993–3996, 2006.

R. O. Dillman, J. Herndon, S. L. Seagren, Jr. Eaton, W. L., and M. R. Green. Improved survival in stage III non-small-cell lung cancer: Seven-year follow-up of cancer and leukemia group B (CALGB) 8433 trial. *J Natl Cancer Inst*, 88(17):1210–1215, 1996.

G. X. Ding. Energy spectra, angular spread, fluence profiles and dose distributions of 6 and 18 MV photon beams: results of Monte Carlo simulations for a Varian 2100EX accelerator. *Phys Med Biol*, 47(7):1025–1046, 2002.

S. J. Doran, T. Brochard, J. Adamovics, N. Krstajic, and E. Bräuer-Krisch. An investigation of the potential of optical computed tomography for imaging of synchrotron-generated x-rays at high spatial resolution. *Phys Med Biol*, 55(5):1531–1547, 2010.

S. J. Doran, K. K. Koerkamp, M. A. Bero, P. Jenneson, E. J. Morton, and W. B. Gilboy. A CCD-based optical CT scanner for high-resolution 3D imaging of radiation dose distributions: equipment specifications, optical simulations and preliminary results. *Phys Med Biol*, 46(12):3191–3213, 2001.

S. Egan and W. Laub. Development of an accurate Monte Carlo model of the standard Clinac 6MV beam. *Med Phys*, 40:396, 2013.

E. D. Ehler and W. A. Tomé. Step and shoot IMRT to mobile targets and techniques to mitigate the interplay effect. *Phys Med Biol*, 54(13):4311–4324, 2009.

B. Emami, J. Lyman, A. Brown, L. Coia, M. Goitein, J. E. Munzenrider, B. Shank, L. J. Solin, and M. Wesson. Tolerance of normal tissue to therapeutic irradiation. *Int J Radiat Oncol Biol Phys*, 21(1):109–122, 1991.

M. Engelsman, G. C. Sharp, T. Bortfeld, R. Onimaru, and H. Shirato. How much margin reduction is possible through gating or breath hold? *Phys Med Biol*, 50(3):477–490, 2005.

G. A. Ezzell, J. W. Burmeister, N. Dogan, T. J. LoSasso, J. G. Mechalakos, D. Mihailidis, A. Molineu, J. R. Palta, C. R. Ramsey, B. J. Salter, J. Shi, P. Xia, N. J. Yue, and Y. Xiao. IMRT commissioning: Multiple institution planning and dosimetry comparisons, a report from AAPM Task Group 119. *Med Phys*, 36(11):5359–5373, 2009.

A. J. Fakiris, R. C. McGarry, C. T. Yiannoutsos, L. Papiez, M. Williams, M. A. Henderson, and R. Timmerman. Stereotactic body radiation therapy for early-stage non-small-cell lung carcinoma: Four-year results of a prospective phase II study. *Int J Radiat Oncol Biol Phys*, 75(3):677–682, 2009.

B. C. Ferreira, M. C. Lopes, and M. Capela. Evaluation of an Epson flatbed scanner to read Gafchromic EBT films for radiation dosimetry. *Phys Med Biol*, 54(4):1073–1085, 2009.

E. C. Ford, G. S. Mageras, E. Yorke, and C. C. Ling. Respiration-correlated spiral CT: a method of measuring respiratory-induced anatomic motion for radiation treatment planning. *Med Phys*, 30(1):88–97, 2003.

M. Fragoso, I. Kawrakow, B. A. Faddegon, T. D. Solberg, and I. J. Chetty. Fast, accurate photon beam accelerator modeling using BEAMnrc: a systematic investigation of efficiency enhancing methods and cross-section data. *Med Phys*, 36(12):5451–5466, 2009.

R. George, S. S. Vedam, T. D. Chung, V. Ramakrishnan, and P. J. Keall. The application of the sinusoidal model to lung cancer patient respiratory motion. *Med Phys*, 32(9): 2850–2861, 2005.

P. Goldstraw, J. Crowley, K. Chansky, D. J. Giroux, P. A. Groome, R. Rami-Porta, P. E. Postmus, V. Rusch, and L. Sobin. The IASLC Lung Cancer Staging Project: Proposals for the revision of the TNM stage groupings in the forthcoming (seventh) edition of the TNM Classification of malignant tumours. *J Thorac Oncol*, 2(8):706–714, 2007.

J. C. Gore, Y. S. Kang, and R. J. Schulz. Measurement of radiation dose distributions by nuclear magnetic resonance (NMR) imaging. *Phys Med Biol*, 29(10):1189–1197, 1984.

J. C. Gore, M. Ranade, M. J. Maryanski, and R. J. Schulz. Radiation dose distributions in three dimensions from tomographic optical density scanning of polymer gels: I. development of an optical scanner. *Phys Med Biol*, 41(12):2695–2704, 1996.

I. S. Grills, V. S. Mangona, R. Welsh, G. Chmielewski, E. McInerney, S. Martin, J. Wloch, H. Ye, and L. L. Kestin. Outcomes after stereotactic lung radiotherapy or wedge resection for stage I non-small-cell lung cancer. *J Clin Oncol*, 28(6):928–935, 2010.

P. Guo, J. Adamovics, and M. Oldham. A practical three-dimensional dosimetry system for radiation therapy. *Med Phys*, 33(10):3962–3972, 2006a.

P. Y. Guo, J. A. Adamovics, and M. Oldham. Characterization of a new radiochromic three-dimensional dosimeter. *Med Phys*, 33(5):1338–1345, 2006b.

J. Hanley, M. M. Debois, D. Mah, G. S. Mageras, A. Raben, K. Rosenzweig, B. Mychalczak, L. H. Schwartz, P. J. Gloeggler, W. Lutz, C. C. Ling, S. A. Leibel, Z. Fuks, and G. J. Kutcher. Deep inspiration breath-hold technique for lung tumors: The potential value of target immobilization and reduced lung density in dose escalation. *Int J Radiat Oncol Biol Phys*, 45(3):603–611, 1999.

J. D. Hazle, L. Hefner, C. E. Nyerick, L. Wilson, and A. L. Boyer. Dose-response characteristics of a ferrous-sulphate-doped gelatin system for determining radiation absorbed dose

distributions by magnetic resonance imaging (Fe MRI). *Phys Med Biol*, 36(8):1117–1125, 1991.

E. Heath and J. Seuntjens. Development and validation of a BEAMnrc component module for accurate Monte Carlo modelling of the Varian dynamic Millennium multileaf collimator. *Phys Med Biol*, 48(24):4045–4063, 2003.

M. L. Hernando, L. B. Marks, G. C. Bentel, S. M. Zhou, D. Hollis, S. K. Das, M. Fan, M. T. Munley, T. D. Shafman, M. S. Anscher, and P. A. Lind. Radiation-induced pulmonary toxicity: A dose-volume histogram analysis in 201 patients with lung cancer. *Int J Radiat Oncol Biol Phys*, 51(3):650–659, 2001.

H. G. Hughes. Improved logic for sampling Landau straggling in MCNP5, September 12-15 2005.

ICRU37. Stopping powers for electrons and positrons. Technical Report 37, International Commission on Radiation Units and Measurements, 1984.

ICRU50. Prescribing, recording, and reporting photon beam therapy. Technical Report 50, International Commission on Radiation Units and Measurements, 1993.

ICRU62. Prescribing, recording, and reporting photon beam therapy (Supplement to ICRU Report 50). Technical Report 62, International Commission on Radiation Units and Measurements, 1999.

ICRU83. Prescribing, recording, and reporting intensity-modulated photon-beam therapy (IMRT). Technical Report 83, International Commission on Radiation Units and Measurements, 2010.

D. A. Jaffray, J. J. Battista, A. Fenster, and P. Munro. X-ray sources of medical linear accelerators: focal and extra-focal radiation. *Med Phys*, 20(5):1417–1427, 1993.

M. D. Jensen, A. Abdellatif, J. Chen, and E. Wong. Study of the IMRT interplay effect using a 4DCT Monte Carlo dose calculation. *Phys Med Biol*, 57(8):N89–N99, 2012.

R. Jeraj, P. J. Keall, and P. M. Ostwald. Comparisons between MCNP, EGS4 and experiment for clinical electron beams. *Phys Med Biol*, 44(3):705–717, 1999.

S. B. Jiang, C. Pope, K. M. Al Jarrah, J. H. Kung, T. Bortfeld, and G. T. Chen. An experimental investigation on intra-fractional organ motion effects in lung IMRT treatments. *Phys Med Biol*, 48(12):1773–1784, 2003.

S. Junell and L. DeWerd. Determination of the energy correction factor for TLD-100 in 6 and 10 MV photon beams relative to ^{60}Co (abstract). *Med Phys*, 36:2594, 2009.

S. L. Junell. *Dosimetry for Small and Nonstandard Fields*. Ph.D. dissertation, 2013.

T. Kairn, T. Aland, and J. Kenny. Local heterogeneities in early batches of EBT2 film: a suggested solution. *Phys Med Biol*, 55(15):L37–L42, 2010.

I. Kawrakow, D. W. Rogers, and B. R. Walters. Large efficiency improvements in BEAMnrc using directional bremsstrahlung splitting. *Med Phys*, 31(10):2883–2898, 2004.

I. Kawrakow and B. R. Walters. Efficient photon beam dose calculations using DOSXYZnrc with BEAMnrc. *Med Phys*, 33(8):3046–3056, 2006.

P. J. Keall, E. Colvill, R. O'Brien, J. A. Ng, P. R. Poulsen, T. Eade, A. Kneebone, and J. T. Booth. The first clinical implementation of electromagnetic transponder-guided MLC tracking. *Med Phys*, 41(2):020702, 2014.

P. J. Keall, G. S. Mageras, J. M. Balter, R. S. Emery, K. M. Forster, S. B. Jiang, J. M. Kapatoes, D. A. Low, M. J. Murphy, B. R. Murray, C. R. Ramsey, M. B. Van Herk, S. S. Vedam, J. W. Wong, and E. Yorke. The management of respiratory motion in radiation oncology report of AAPM Task Group 76. *Med Phys*, 33(10):3874–3900, 2006.

P. J. Keall, J. V. Siebers, B. Libby, and R. Mohan. Determining the incident electron fluence for Monte Carlo-based photon treatment planning using a standard measured data set. *Med Phys*, 30(4):574–582, 2003.

R. G. Kelly, K. J. Jordan, and J. J. Battista. Optical CT reconstruction of 3D dose distributions using the ferrous-benzoic-xylenol (FBX) gel dosimeter. *Med Phys*, 25(9):1741–1750, 1998.

J. Kim, M. Yoon, S. Kim, D. Shin, S. B. Lee, Y. K. Lim, D. W. Kim, and S. Y. Park. Three-dimensional radiochromic film dosimetry of proton clinical beams using a Gafchromic EBT2 film array. *Radiat Prot Dosimetry*, 151(2):272–277, 2012.

J. O. Kim, J. V. Siebers, P. J. Keall, M. R. Arnfield, and R. Mohan. A Monte Carlo study of radiation transport through multileaf collimators. *Med Phys*, 28(12):2497–2506, 2001.

M. W. Kissick, S. A. Boswell, R. Jeraj, and T. R. Mackie. Confirmation, refinement, and extension of a study in intrafraction motion interplay with sliding jaw motion. *Med Phys*, 32(7):2346–2350, 2005.

M. W. Kissick, R. T. Flynn, D. C. Westerly, P. W. Hoban, X. Mo, E. T. Soisson, K. C. McCall, T. R. Mackie, and R. Jeraj. On the impact of longitudinal breathing motion randomness for tomotherapy delivery. *Phys Med Biol*, 53(18):4855–4873, 2008.

M. W. Kissick and T. R. Mackie. Task Group 76 Report on 'The management of respiratory motion in radiation oncology' [Med. Phys. 33, 3874-3900 (2006)]. *Med Phys*, 36(12):5721–5722, 2009.

M. W. Kissick, T. R. Mackie, R. T. Flynn, X. Mo, D. D. Campos, Y. Yan, and D. Zhao. Investigation of probabilistic optimization for tomotherapy. *J Appl Clin Med Phys*, 13 (5):155–169, 2012.

N. V. Klassen, L. van der Zwan, and J. Cygler. GafChromic MD-55: Investigated as a precision dosimeter. *Med Phys*, 24(12):1924–1934, 1997.

H. W. Koch and J. W. Motz. Bremsstrahlung cross-section formulas and related data. *Rev Mod Phys*, 31:920–955, 1959.

H. Koivunoro, T. Siiskonen, P. Kotiluoto, I. Auterinen, E. Hippelainen, and S. Savolainen. Accuracy of the electron transport in MCNP5 and its suitability for ionization chamber response simulations: A comparison with the EGSnrc and PENELOPE codes. *Med Phys*, 39(3):1335–1344, 2012.

H. W. Korin, R. L. Ehman, S. J. Riederer, J. P. Felmlee, and R. C. Grimm. Respiratory kinematics of the upper abdominal organs: A quantitative study. *Magn Reson Med*, 23 (1):172–178, 1992.

S. L. S. Kwa, J. V. Lebesque, J. C. M. Theuws, L. B. Marks, M. T. Munley, G. Bentel, D. Oetzel, U. Spahn, M. V. Graham, R. E. Drzymala, J. A. Purdy, A. S. Lichter, M. K. Martel, and R. K. Ten Haken. Radiation pneumonitis as a function of mean lung dose: An analysis of pooled data of 540 patients. *Int J Radiat Oncol Biol Phys*, 42(1):1–9, 1998.

L. Landau. On the energy loss of fast particles by ionization. *J Phys USSR*, 8:201, 1944.

I. Lax, H. Blomgren, I. Naslund, and R. Svanstrom. Stereotactic radiotherapy of malignancies in the abdomen. Methodological aspects. *Acta Oncol*, 33(6):677–683, 1994.

H. Li, A. K. Lee, J. L. Johnson, R. X. Zhu, and R. J. Kudchadker. Characterization of dose impact on IMRT and VMAT from couch attenuation for two Varian couches. *J Appl Clin Med Phys*, 12(3):23–31, 2011.

H. Li, Y. Li, X. Zhang, X. Li, W. Liu, M. T. Gillin, and X. R. Zhu. Dynamically accumulated dose and 4D accumulated dose for moving tumors. *Med Phys*, 39(12):7359–7367, 2012.

H. Li, P. Park, W. Liu, J. Matney, Z. Liao, P. Balter, Y. Li, X. Zhang, X. Li, and X. R. Zhu. Patient-specific quantification of respiratory motion-induced dose uncertainty for step-and-shoot IMRT of lung cancer. *Med Phys*, 40(12):121712, 2013.

D. W. Litzenberg, S. W. Hadley, N. Tyagi, J. M. Balter, R. K. Ten Haken, and I. J. Chetty. Synchronized dynamic dose reconstruction. *Med Phys*, 34(1):91–102, 2007.

D. A. Low and J. F. Dempsey. Evaluation of the gamma dose distribution comparison method. *Med Phys*, 30(9):2455–2464, 2003.

D. A. Low, W. B. Harms, S. Mutic, and J. A. Purdy. A technique for the quantitative evaluation of dose distributions. *Med Phys*, 25(5):656–661, 1998.

A. E. Lujan, E. W. Larsen, J. M. Balter, and R. K. Ten Haken. A method for incorporating organ motion due to breathing into 3d dose calculations. *Med Phys*, 26(5):715–20, 1999.

B. D. Lynch, J. Kozelka, M. K. Ranade, J. G. Li, W. E. Simon, and J. F. Dempsey. Important considerations for radiochromic film dosimetry with flatbed CCD scanners and EBT GAFCHROMIC® film. *Med Phys*, 33(12):4551–4556, 2006.

T. R. Mackie, J. W. Scrimger, and J. J. Battista. A convolution method of calculating dose for 15MV x rays. *Med Phys*, 12(2):188–196, 1985.

K. Malinowski, C. Noel, W. Lu, K. Lechleiter, J. Hubenschmidt, D. Low, and P. Parikh. Development of the 4D Phantom for patient-specific, end-to-end radiation therapy QA. *Proc SPIE Med Imag Conf*, 6510:U148–U156, 2007.

L. B. Marks, S. M. Bentzen, J. O. Deasy, F. M. Kong, J. D. Bradley, I. S. Vogelius, I. El Naqa, J. L. Hubbs, J. V. Lebesque, R. D. Timmerman, M. K. Martel, and A. Jackson. Radiation dose-volume effects in the lung. *Int J Radiat Oncol Biol Phys*, 76(3 Suppl): S70–S76, 2010a.

L. B. Marks, E. D. Yorke, A. Jackson, R. K. Ten Haken, L. S. Constine, A. Eisbruch, S. M. Bentzen, J. Nam, and J. O. Deasy. Use of normal tissue complication probability models in the clinic. *Int J Radiat Oncol Biol Phys*, 76(3):S10–S19, 2010b.

M. Martišíková, B. Ackermann, and O. Jäkel. Analysis of uncertainties in Gafchromic® EBT film dosimetry of photon beams. *Phys Med Biol*, 53(24):7013–7027, 2008.

M. J. Maryanski, J. C. Gore, R. P. Kennan, and R. J. Schulz. NMR relaxation enhancement in gels polymerized and cross-linked by ionizing-radiation: A new approach to 3D dosimetry by MRI. *Magn Reson Imag*, 11(2):253–258, 1993.

M. J. Maryanski, R. J. Schulz, G. S. Ibbott, J. C. Gatenby, J. Xie, D. Horton, and J. C. Gore. Magnetic resonance imaging of radiation dose distributions using a polymer-gel dosimeter. *Phys Med Biol*, 39(9):1437–1455, 1994.

B. P. McCabe, M. A. Speidel, T. L. Pike, and M. S. Van Lysel. Calibration of GafChromic XR-RV3 radiochromic film for skin dose measurement using standardized x-ray spectra and a commercial flatbed scanner. *Med Phys*, 38(4):1919–1930, 2011.

M. McEwen, L. DeWerd, G. Ibbott, D. Followill, D. W. Rogers, S. Seltzer, and J. Seuntjens. Addendum to the AAPM's TG-51 protocol for clinical reference dosimetry of high-energy photon beams. *Med Phys*, 41(4):041501, 2014.

R. C. McGarry, L. Papiez, M. Williams, T. Whitford, and R. D. Timmerman. Stereotactic body radiation therapy of early-stage non-small-cell lung carcinoma: Phase I study. *Int J Radiat Oncol Biol Phys*, 63(4):1010–1015, 2005.

A. L. McNiven, M. B. Sharpe, and T. G. Purdie. A new metric for assessing IMRT modulation complexity and plan deliverability. *Med Phys*, 37(2):505–515, 2010.

M. Mehta, R. Scrimger, R. Mackie, B. Paliwal, R. Chappell, and J. Fowler. A new approach to dose escalation in non-small-cell lung cancer. *Int J Radiat Oncol Biol Phys*, 49(1):23–33, 2001.

L. Menegotti, A. Delana, and A. Martignano. Radiochromic film dosimetry with flatbed scanners: A fast and accurate method for dose calibration and uniformity correction with single film exposure. *Med Phys*, 35(7):3078–3085, 2008.

B. Mersseman and C. De Wagter. Characteristics of a commercially available film digitizer and their significance for film dosimetry. *Phys Med Biol*, 43(6):1803–1812, 1998.

A. Micke, D. F. Lewis, and X. Yu. Multichannel film dosimetry with nonuniformity correction. *Med Phys*, 38(5):2523–2534, 2011.

J. R. Molina, P. Yang, S. D. Cassivi, S. E. Schild, and A. A. Adjei. Non-small cell lung cancer: Epidemiology, risk factors, treatment, and survivorship. *Mayo Clin Proc*, 83(5): 584–594, 2008.

F. Mourtada, C. G. Soares, S. M. Seltzer, P. M. Bergstrom, J. M. Fernandez-Verea, J. Asenjo, and S. H. Lott. Dosimetry characterization of a ^{32}P source wire used for intravascular brachytherapy with automated stepping. *Med Phys*, 30(5):959–971, 2003.

M. K. Murphy, R. K. Piper, L. R. Greenwood, M. G. Mitch, P. J. Lamperti, S. M. Seltzer, M. J. Bales, and M. H. Phillips. Evaluation of the new cesium-131 seed for use in low-energy x-ray brachytherapy. *Med Phys*, 31(6):1529–1538, 2004.

A. Niroomand-Rad, C. R. Blackwell, B. M. Coursey, K. P. Gall, J. M. Galvin, W. L. McLaughlin, A. S. Meigooni, R. Nath, J. E. Rodgers, and C. G. Soares. Radiochromic film dosimetry: Recommendations of AAPM Radiation Therapy Committee Task Group 55. *Med Phys*, 25(11):2093–2115, 1998.

A. A. Nunn, S. D. Davis, J. A. Micka, and L. A. DeWerd. LiF:Mg,Ti TLD response as a function of photon energy for moderately filtered x-ray spectra in the range of 20-250 kVp relative to 60Co. *Med Phys*, 35(5):1859–1869, 2008.

J. Nyman, K. A. Johansson, and U. Hulten. Stereotactic hypofractionated radiotherapy for stage I non-small cell lung cancer-Mature results for medically inoperable patients. *Lung Cancer*, 51(1):97–103, 2006.

J. E. O'Connor. The density scaling theorem applied to lateral electronic equilibrium. *Med Phys*, 11(5):678–680, 1984.

M. Oldham and L. Kim. Optical-CT gel-dosimetry. II: Optical artifacts and geometrical distortion. *Med Phys*, 31(5):1093–1104, 2004.

M. Oldham, H. Sakhalkar, P. Guo, and J. Adamovics. An investigation of the accuracy of an IMRT dose distribution using two- and three-dimensional dosimetry techniques. *Med Phys*, 35(5):2072–2080, 2008.

M. Oldham, J. H. Siewerdsen, A. Shetty, and D. A. Jaffray. High resolution gel-dosimetry by optical-CT and MR scanning. *Med Phys*, 28(7):1436–1445, 2001.

L. E. Olsson, A. Fransson, A. Ericsson, and S. Mattsson. MR imaging of absorbed dose distributions for radiotherapy using ferrous sulphate gels. *Phys Med Biol*, 35(12):1623–1631, 1990.

L. E. Olsson, S. Petersson, L. Ahlgren, and S. Mattsson. Ferrous sulphate gels for determination of absorbed dose distributions using MRI technique: basic studies. *Phys Med Biol*, 34(1):43–52, 1989.

L. Paelinck, W. De Neve, and C. De Wagter. Precautions and strategies in using a commercial flatbed scanner for radiochromic film dosimetry. *Phys Med Biol*, 52(1):231–242, 2007.

A. L. Palmer, P. Di Pietro, S. Alobaidli, F. Issa, S. Doran, D. Bradley, and A. Nisbet. Comparison of methods for the measurement of radiation dose distributions in high dose rate (HDR) brachytherapy: Ge-doped optical fiber, EBT3 Gafchromic film, and PRESAGE® radiochromic plastic. *Med Phys*, 40(6):061707, 2013.

N. Papanikolaou, T. R. Mackie, C. Meger-Wells, M. Gehring, and P. Reckwerdt. Investigation of the convolution method for polyenergetic spectra. *Med Phys*, 20(5):1327–1336, 1993.

A. B. Paxton. *Improved Dosimetry for ^{90}Y Microsphere Treatments of Liver Malignancies*. Ph.D. dissertation, 2012.

T. V. Pedersen, D. R. Olsen, and A. Skretting. Measurement of the ferric diffusion coefficient in agarose and gelatine gels by utilization of the evolution of a radiation induced edge as reflected in relaxation rate images. *Phys Med Biol*, 42(8):1575–1585, 1997.

W. I. Rae, C. A. Willemse, M. G. Lötter, J. S. Engelbrecht, and J. C. Swarts. Chelator effect on ion diffusion in ferrous-sulfate-doped gelatin gel dosimeters as analyzed by MRI. *Med Phys*, 23(1):15–23, 1996.

J. Raffi. *Limitations of current dosimetry for intracavitary accelerated partial breast irradiation with high dose rate ^{192}Ir and electronic brachytherapy sources*. Ph.D. dissertation, 2010.

N. Reynaert, H. Palmans, H. Thierens, and R. Jeraj. Parameter dependence of the MCNP electron transport in determining dose distributions. *Med Phys*, 29(10):2446–2454, 2002.

L. Richley, A. C. John, H. Coomber, and S. Fletcher. Evaluation and optimization of the new EBT2 radiochromic film dosimetry system for patient dose verification in radiotherapy. *Phys Med Biol*, 55(9):2601–2617, 2010.

A. Richter, J. Wilbert, and M. Flentje. Dosimetric evaluation of intrafractional tumor motion by means of a robot driven phantom. *Med Phys*, 38(10):5280–5289, 2011.

C. Richter, J. Pawelke, L. Karsch, and J. Woithe. Energy dependence of EBT-1 radiochromic film response for photon (10 kVp-15 MVp) and electron beams (6-18 MeV) readout by a flatbed scanner. *Med Phys*, 36(12):5506–5514, 2009.

D. W. Rogers, B. A. Faddegon, G. X. Ding, C. M. Ma, J. We, and T. R. Mackie. BEAM: a Monte Carlo code to simulate radiotherapy treatment units. *Med Phys*, 22(5):503–524, 1995.

H. Sakhalkar, D. Sterling, J. Adamovics, G. Ibbott, and M. Oldham. Investigation of the feasibility of relative 3D dosimetry in the Radiologic Physics Center Head and Neck IMRT phantom using Presage/optical-CT. *Med Phys*, 36(7):3371–3377, 2009a.

H. S. Sakhalkar, J. Adamovics, G. Ibbott, and M. Oldham. A comprehensive evaluation of the PRESAGE/optical-CT 3D dosimetry system. *Med Phys*, 36(1):71–82, 2009b.

S. Saur and J. Frengen. GafChromic EBT film dosimetry with flatbed CCD scanner: A novel background correction method and full dose uncertainty analysis. *Med Phys*, 35(7): 3094–3101, 2008.

W. T. Sause, C. Scott, S. Taylor, D. Johnson, R. Livingston, R. Komaki, B. Emami, W. J. Curran, R. W. Byhardt, A. T. Turrisi, and et al. Radiation Therapy Oncology Group (RTOG) 88-08 and Eastern Cooperative Oncology Group (ECOG) 4588: preliminary results of a phase III trial in regionally advanced, unresectable non-small-cell lung cancer. *J Natl Cancer Inst*, 87(3):198–205, 1995.

D. R. Schaart, J. T. Jansen, J. Zoetelief, and P. F. de Leege. A comparison of MCNP4C electron transport with ITS 3.0 and experiment at incident energies between 100 keV and

20 MeV: influence of voxel size, substeps and energy indexing algorithm. *Phys Med Biol*, 47(9):1459–1484, 2002.

R. J. Schulz, A. F. deGuzman, D. B. Nguyen, and J. C. Gore. Dose-response curves for Fricke-infused agarose gels as obtained by nuclear magnetic resonance. *Phys Med Biol*, 35(12):1611–1622, 1990.

J. Seco, G. C. Sharp, J. Turcotte, D. Gierga, T. Bortfeld, and H. Paganetti. Effects of organ motion on IMRT treatments with segments of few monitor units. *Med Phys*, 34(3): 923–934, 2007.

S. M. Seltzer and M. J. Berger. Bremsstrahlung spectra from electron interactions with screened atomic-nuclei and orbital electrons. *Nucl Inst Meth Phys Res B*, 12(1):95–134, 1985.

J. K. Seppälä and J. A. Kulmala. Increased beam attenuation and surface dose by different couch inserts of treatment tables used in megavoltage radiotherapy. *J Appl Clin Med Phys*, 12(4):15–23, 2011.

Y. Seppenwoolde, H. Shirato, K. Kitamura, S. Shimizu, M. van Herk, J. V. Lebesque, and K. Miyasaka. Precise and real-time measurement of 3D tumor motion in lung due to breathing and heartbeat, measured during radiotherapy. *Int J Radiat Oncol Biol Phys*, 53(4):822–834, 2002.

D. Sheikh-Bagheri and D. W. Rogers. Monte Carlo calculation of nine megavoltage photon beam spectra using the BEAM code. *Med Phys*, 29(3):391–402, 2002a.

D. Sheikh-Bagheri and D. W. Rogers. Sensitivity of megavoltage photon beam Monte Carlo simulations to electron beam and other parameters. *Med Phys*, 29(3):379–390, 2002b.

D. Sheikh-Bagheri, D. W. Rogers, C. K. Ross, and J. P. Seuntjens. Comparison of measured and Monte Carlo calculated dose distributions from the NRC linac. *Med Phys*, 27(10): 2256–2266, 2000.

H. Shirato, S. Shimizu, T. Kunieda, K. Kitamura, M. van Herk, K. Kagei, T. Nishioka, S. Hashimoto, K. Fujita, H. Aoyama, K. Tsuchiya, K. Kudo, and K. Miyasaka. Physical aspects of a real-time tumor-tracking system for gated radiotherapy. *Int J Radiat Oncol Biol Phys*, 48(4):1187–1195, 2000.

H. Shirato, K. Suzuki, G. C. Sharp, K. Fujita, R. Onimaru, M. Fujino, N. Kato, Y. Osaka, R. Kinoshita, H. Taguchi, S. Onodera, and K. Miyasaka. Speed and amplitude of lung tumor motion precisely detected in four-dimensional setup and in real-time tumor-tracking radiotherapy. *Int J Radiat Oncol Biol Phys*, 64(4):1229–1236, 2006.

J. V. Siebers, P. J. Keall, J. O. Kim, and R. Mohan. A method for photon beam Monte Carlo multileaf collimator particle transport. *Phys Med Biol*, 47(17):3225–3249, 2002.

R. Siegel, C. DeSantis, K. Virgo, K. Stein, A. Mariotto, T. Smith, D. Cooper, T. Gansler, C. Lerro, S. Fedewa, C. Lin, C. Leach, R. S. Cannady, H. Cho, S. Scoppa, M. Hachey, R. Kirch, A. Jemal, and E. Ward. Cancer treatment and survivorship statistics, 2012. *CA Cancer J Clin*, 62(4):220–241, 2012.

R. Siegel, J. Ma, Z. Zou, and A. Jemal. Cancer statistics, 2014. *CA Cancer J Clin*, 64(1): 9–29, 2014.

P. S. Skyt, P. Balling, J. B. Petersen, E. S. Yates, and L. P. Muren. Temperature dependence of the dose response for a solid-state radiochromic dosimeter during irradiation and storage. *Med Phys*, 38(5):2806–2811, 2011.

A. C. Spalding, K. W. Jee, K. Vineberg, M. Jablonowski, B. A. Fraass, C. C. Pan, T. S. Lawrence, R. K. Haken, and E. Ben-Josef. Potential for dose-escalation and reduction

of risk in pancreatic cancer using IMRT optimization with lexicographic ordering and gEUD-based cost functions. *Med Phys*, 34(2):521–529, 2007.

C. Stambaugh, B. E. Nelms, T. Dilling, C. Stevens, K. Latifi, G. Zhang, E. Moros, and V. Feygelman. Experimentally studied dynamic dose interplay does not meaningfully affect target dose in VMAT SBRT lung treatments. *Med Phys*, 40(9):091710, 2013.

N. Suchowerska, P. Hoban, M. Butson, A. Davison, and P. Metcalfe. Directional dependence in film dosimetry: radiographic and radiochromic film. *Phys Med Biol*, 46(5):1391–1397, 2001.

J. G. Sutherland and D. W. Rogers. Monte Carlo calculated absorbed-dose energy dependence of EBT and EBT2 film. *Med Phys*, 37(3):1110–1116, 2010.

T. Teke, B. Gill, C. Duzenli, and I. A. Popescu. A Monte Carlo model of the Varian IGRT couch top for RapidArc QA. *Phys Med Biol*, 56(24):N295–N305, 2011.

A. Thomas, J. Newton, J. Adamovics, and M. Oldham. Commissioning and benchmarking a 3D dosimetry system for clinical use. *Med Phys*, 38(8):4846–4857, 2011.

A. Thomas, M. Niebanck, T. Juang, Z. Wang, and M. Oldham. A comprehensive investigation of the accuracy and reproducibility of a multitarget single isocenter VMAT radiosurgery technique. *Med Phys*, 40(12):121725, 2013.

R. Timmerman, L. Papiez, R. McGarry, L. Likes, C. DesRosiers, S. Frost, and M. Williams. Extracranial stereotactic radioablation: Results of a phase I study in medically inoperable stage I non-small cell lung cancer. *Chest*, 124(5):1946–1955, 2003.

R. Timmerman, R. Paulus, J. Galvin, J. Michalski, W. Straube, J. Bradley, A. Fakiris, A. Bezjak, G. Videtic, D. Johnstone, J. Fowler, E. Gore, and H. Choy. Stereotactic body radiation therapy for inoperable early stage lung cancer. *JAMA*, 303(11):1070–1076, 2010.

M. J. Tobin, T. S. Chadha, G. Jenouri, S. J. Birch, H. B. Gazeroglu, and M. A. Sackner. Breathing patterns. 1. Normal subjects. *Chest*, 84(2):202–205, 1983a.

M. J. Tobin, T. S. Chadha, G. Jenouri, S. J. Birch, H. B. Gazeroglu, and M. A. Sackner. Breathing patterns. 2. Diseased subjects. *Chest*, 84(3):286–294, 1983b.

W. A. Tomé and J. F. Fowler. On cold spots in tumor subvolumes. *Med Phys*, 29(7): 1590–1598, 2002.

A. Trofimov, C. Vrancic, T. C. Chan, G. C. Sharp, and T. Bortfeld. Tumor trailing strategy for intensity-modulated radiation therapy of moving targets. *Med Phys*, 35(5):1718–1733, 2008.

G. S. Tudor, S. V. Harden, and S. J. Thomas. Three-dimensional analysis of the respiratory interplay effect in helical tomotherapy: Baseline variations cause the greater part of dose inhomogeneities seen. *Med Phys*, 41(3):031704, 2014.

W. Ulmer, J. Pyyry, and W. Kaissl. A 3D photon superposition/convolution algorithm and its foundation on results of Monte Carlo calculations. *Phys Med Biol*, 50(8):1767–1790, 2005.

M. van Herk, P. Remeijer, C. Rasch, and J. V. Lebesque. The probability of correct target dosage: Dose-population histograms for deriving treatment margins in radiotherapy. *Int J Radiat Oncol Biol Phys*, 47(4):1121–1135, 2000.

S. S. Vedam, P. J. Keall, V. R. Kini, and R. Mohan. Determining parameters for respiration-gated radiotherapy. *Med Phys*, 28(10):2139–2146, 2001.

S. S. Vedam, P. J. Keall, V. R. Kini, H. Mostafavi, H. P. Shukla, and R. Mohan. Acquiring a four-dimensional computed tomography dataset using an external respiratory signal. *Phys Med Biol*, 48(1):45–62, 2003.

B. R. Walters, I. Kawrakow, and D. W. Rogers. History by history statistical estimators in the BEAM code system. *Med Phys*, 29(12):2745–2752, 2002.

S. Webb. Optimization by simulated annealing of three-dimensional conformal treatment planning for radiation fields defined by a multileaf collimator. *Phys Med Biol*, 36(9): 1201–1226, 1991.

S. Webb. Optimization by simulated annealing of three-dimensional, conformal treatment planning for radiation fields defined by a multileaf collimator: II. Inclusion of two-dimensional modulation of the x-ray intensity. *Phys Med Biol*, 37(8):1689–1704, 1992.

S. Webb. Use of a quantitative index of beam modulation to characterize dose conformality: illustration by a comparison of full beamlet IMRT, few-segment IMRT (fsIMRT) and conformal unmodulated radiotherapy. *Phys Med Biol*, 48(14):2051–2062, 2003.

J. Wolf, M. E. Patno, B. Roswit, and N. D'Esopo. Controlled study of survival of patients with clinically inoperable lung cancer treated with radiation therapy. *Am J Med*, 40(3): 360–367, 1966.

J. W. Wong, M. B. Sharpe, D. A. Jaffray, V. R. Kini, J. M. Robertson, J. S. Stromberg, and A. A. Martinez. The use of active breathing control (ABC) to reduce margin for breathing motion. *Int J Radiat Oncol Biol Phys*, 44(4):911–919, 1999.

M. K. Woo and J. R. Cunningham. The validity of the density scaling method in primary electron transport for photon and electron beams. *Med Phys*, 17(2):187–194, 1990.

Y. Xu, C. S. Wuu, and M. J. Maryanski. Determining optimal gel sensitivity in optical CT scanning of gel dosimeters. *Med Phys*, 30(8):2257–2263, 2003.

Y. Xu, C. S. Wuu, and M. J. Maryanski. Performance of a commercial optical CT scanner and polymer gel dosimeters for 3-D dose verification. *Med Phys*, 31(11):3024–3033, 2004.

J. N. Yang, T. R. Mackie, P. Reckwerdt, J. O. Deasy, and B. R. Thomadsen. An investigation of tomotherapy beam delivery. *Med Phys*, 24(3):425–436, 1997.

E. D. Yorke, A. Jackson, K. E. Rosenzweig, S. A. Merrick, D. Gabrys, E. S. Venkatraman, C. M. Burman, S. A. Leibel, and C. C. Ling. Dose-volume factors contributing to the incidence of radiation pneumonitis in non-small-cell lung cancer patients treated with three-dimensional conformal radiation therapy. *Int J Radiat Oncol Biol Phys*, 54(2): 329–339, 2002.

C. X. Yu, D. A. Jaffray, and J. W. Wong. The effects of intra-fraction organ motion on the delivery of dynamic intensity modulation. *Phys Med Biol*, 43(1):91–104, 1998.

L. Zhan, R. Jiang, and E. K. Osei. Beam coordinate transformations from DICOM to DOSXYZnrc. *Phys Med Biol*, 57(24):N513–N523, 2012.

B. Zhao, Y. Yang, T. Li, X. Li, D. E. Heron, and M. S. Huq. Statistical analysis of target motion in gated lung stereotactic body radiation therapy. *Phys Med Biol*, 56(5):1385–1395, 2011.